

# **Polymer Electrolyte Membrane Degradation and Mobility in Fuel Cells: a Solid-state NMR Investigation**

Von der Fakultät für Chemie der Universität Stuttgart  
zur Erlangung der Würde eines  
Doktors der Naturwissenschaften (Dr. rer. nat.)  
genehmigte Abhandlung

Vorgelegt von  
**Lida Ghassemzadeh Khoshkroodi**  
aus Teheran, Iran

Hauptberichter:	Prof. Dr. K. Müller
Mitberichter:	Prof. Dr. J. Maier
Mitprüfer:	Prof. Dr. E. Roduner
Tag der Einreichung:	19.05.2010
Tag der mündlichen Prüfung:	15.07.2010

Max-Planck-Institut für Festkörperforschung Stuttgart  
und Institut für Physikalische Chemie der Universität Stuttgart

2010



# Contents

CONTENTS .....	3
ABBREVIATIONS AND SYMBOLS .....	7
1. INTRODUCTION .....	13
2. INTRODUCTION TO POLYMER ELECTROLYTE MEMBRANES .....	15
2.1. PEM FUEL CELLS.....	15
2.2. PEM FUEL CELL COMPONENTS.....	18
2.3. NAFION MEMBRANE .....	18
2.3.1. SYNTHESIS OF NAFION.....	19
2.3.2. NAFION MORPHOLOGY.....	20
2.3.3. WATER CONTENT AND CONDUCTIVITY.....	22
2.4. LIMITATIONS OF NAFION AS A FUEL CELL MEMBRANE.....	23
2.4.1. LOW TEMPERATURE OPERATION PROBLEMS.....	23
2.4.2. DURABILITY AND DEGRADATION ISSUE.....	24
2.5. NAFION ALTERNATIVES.....	27
2.5.1. SHORT SIDE CHAIN PERFLUOROSULFONIC ACID IONOMERS.....	28
2.5.2. NAFION/OXIDE COMPOSITE MEMBRANES.....	28
2.6. OPEN QUESTIONS AND MISSING INVESTIGATIONS.....	30
2.7. WHY TO CHOOSE SOLID-STATE NMR SPECTROSCOPY?.....	31
2.8. LITERATURE REVIEW ON NMR STUDIES OF NAFION .....	32
2.8.1. $^1\text{H}$ & $^2\text{H}$ NMR .....	32
2.8.2. $^{19}\text{F}$ NMR.....	33
2.8.3. OTHER NMR TECHNIQUES.....	34
2.8.4. NMR STUDIES ON DEGRADED NAFION .....	35
2.8.5. NMR STUDIES ON NAFION/OXIDE COMPOSITE MEMBRANES.....	36
3. BASICS OF NMR SPECTROSCOPY .....	37
3.1. INTERACTION WITH EXTERNAL MAGNETIC FIELDS .....	37
3.2. INTERNAL INTERACTIONS.....	40
3.2.1. CHEMICAL SHIELDING.....	42

3.2.2.	THE DIPOLAR INTERACTION .....	45
3.3.	SINGLE-PULSE EXCITATION .....	46
3.4.	METHODS FOR IMPROVING RESOLUTION .....	46
3.4.1.	MAGIC ANGLE SPINNING (MAS).....	47
3.4.2.	CROSS POLARIZATION (CP).....	49
3.4.3.	DECOUPLING .....	52
3.5.	NUCLEAR SPIN RELAXATION .....	54
3.5.1.	INVERSION RECOVERY: MEASUREMENT OF $T_1$ .....	57
3.5.2.	SPIN LOCKING: MEASUREMENT OF $T_{1\rho}$ .....	58
4.	FUEL CELL DEGRADATION TESTS .....	61
4.1.	INTRODUCTION.....	61
4.2.	EXPERIMENTAL .....	61
4.2.1.	MATERIALS .....	61
4.2.2.	MEMBRANE PRE-CONDITIONING.....	61
4.2.3.	FUEL CELL TESTS .....	62
4.2.4.	NMR SPECTROSCOPY .....	63
4.3.	RESULTS .....	63
4.4.	DISCUSSION.....	68
4.5.	CONCLUSIONS .....	69
5.	EX-SITU DEGRADATION UNDER MIMIC FUEL CELL CONDITIONS.....	71
5.1.	INTRODUCTION.....	71
5.2.	EXPERIMENTAL .....	71
5.2.1.	MATERIALS AND SAMPLE PREPARATION .....	71
5.2.2.	NMR SPECTROSCOPY .....	75
5.2.3.	EQUIVALENT WEIGHT (EW).....	76
5.3.	RESULTS .....	76
5.4.	DISCUSSION.....	85
5.5.	CONCLUSION .....	93
6.	FENTON DEGRADATION TESTS .....	95
6.1.	INTRODUCTION.....	95
6.2.	EXPERIMENTAL .....	96
6.2.1.	SAMPLE PREPARATION AND FENTON TEST .....	96
6.2.2.	NMR SPECTROSCOPY .....	98
6.2.3.	ATR-FTIR SPECTROSCOPY .....	99
6.3.	RESULTS.....	99

6.4.	DISCUSSION .....	107
6.5.	CONCLUSIONS .....	109
7.	DYNAMICS IN COMPOSITE MEMBRANES.....	111
7.1.	INTRODUCTION.....	111
7.2.	EXPERIMENTAL .....	111
7.2.1.	SAMPLE PREPARATION.....	111
7.2.2.	NMR SPECTROSCOPY .....	113
7.2.3.	EQUIVALENT WEIGHT (EW).....	113
7.3.	RESULTS .....	114
7.4.	DISCUSSION .....	124
7.5.	CONCLUSION .....	127
	SUMMARY .....	129
	DEUTSCHE ZUSAMMENFASSUNG .....	135
	APPENDIX .....	141
	REFERENCES .....	143
	ACKNOWLEDGEMENTS .....	151



## **Abbreviations and Symbols**

### **List of Abbreviations**

AFC	alkaline fuel cell
ATR-FTIR	attenuated total reflection Fourier transformation infra red
BPP	Bloembergen, Purcell and Pound
CP	cross polarization
2D	two dimensional
DAS	dynamic angle spinning
DMA	dynamic mechanical analysis
DMF	dimethylformamide
DMFC	direct methanol fuel cell
DOR	double angle rotation
EPR	electron spin resonance
EW	equivalent weight
FID	free induction decay
FTIR	Fourier transformation infra red
GDL	gas diffusion layer
Hz	hertz
IEC	ion exchange capacity
LF	laboratory frame
LSC	long side chain ionomer
MAS	magic angle spinning
MCFC	molton carbonate fuel cell
MEA	membrane electrode assembly
NMR	nuclear magnetic resonance

OCV	open circuit voltage
PAFC	phosphonic acid fuel cell
PAS	principal axis system
PEM	polymer electrolyte membrane
PEMFC	polymer electrolyte membrane fuel cell
PFG	pulsed-field-gradient
PFSA	perfluorosulfonic acid
PFSI	perfluorosulfonated ionomer
ppm	parts per million
PTFE	polytetrafluorethylene
<i>rf</i>	radio frequency
RH	relative humidity
RT	room temperature
SAXS	small-angle X-ray scattering
SEM	scanning electron microscope
SOFC	solid oxide fuel cell
SSB	spinning sideband
SSC	short side chain ionomer
TPPM	two-pulse phase-modulated
TEM	transmission electron microscopy
TEOS	tetraethoxysilane
TFE	tetrafluoroethylene
TGA	thermogravimetry analysis
TMS	tetramethylsilane
UV	ultra violet
VAS	variable angle spinning
XiX	X inverse-X
XPS	X-ray photoelectron spectroscopy
XRD	X-ray diffraction

**List of Symbols**

$\delta$	chemical shift anisotropy
$\gamma$	gyromagnetic ratio
$\eta$	asymmetry
$\varphi$	in chapter 3: <i>rf</i> field phase, in other chapters: water volume fraction
$\bar{\mu}$	magnetic moment
$\mu_0$	permeability
$\nu_{1/2}$	spectra linewidth
$\sigma$	chemical shielding
$\Delta\sigma$	shielding anisotropy
$\tau$	time delay
$\tau_{acq}$	acquisition period
$\tau_c$	correlation time
$\tau_{wait}$	waiting time
$\omega_0$	Larmor frequency
$\omega_{iso}$	isotropic part of the frequency
$\omega_{aniso}$	anisotropic part of the frequency
$\omega_r$	spinning frequency
$\omega_{rf}$	frequency of <i>rf</i> field
$B_0$	external magnetic field strength
$B_1$	radio frequency field strength
$D$	diffusion coefficient
$E$	energy
$\phi$	polar angle
$\hbar$	Planck's constant

---

$\hat{H}_{CS}$	chemical shielding Hamiltonian
$\hat{H}_D$	magnetic dipolar Hamiltonian
$\hat{H}_D^{II}$	homonuclear magnetic dipolar moment interactions Hamiltonian
$\hat{H}_D^{IS}$	heteronuclear magnetic dipolar moment interactions Hamiltonian
$\hat{H}_{ext}$	external nuclear spin interactions Hamiltonian
$\hat{H}_{int}$	internal nuclear spin interactions Hamiltonian
$\hat{H}_J$	J-coupling Hamiltonian
$\hat{H}_K$	Knight shielding Hamiltonian
$\hat{H}_P$	paramagnetic Hamiltonian
$\hat{H}_Q$	quadrupolar Hamiltonian
$\hat{H}_{rf}$	<i>rf</i> field Hamiltonian
$\hat{H}_z$	Zeeman Hamiltonian
$I$	spin quantum number
$\vec{I}$	spin angular momentum
$k$	Boltzmann constant
$K$	electroosmotic drag coefficient
$\lambda$	number of water molecules per sulfonic acid group
$m$	magnetic quantum number
$M_0$	equilibrium magnetization
$N_+$	number of spins in the lower energy level
$N_-$	number of spins in the upper energy level
$N$	total number of spins
$n$	difference in spin population between energy levels
$\theta$	polar angle

$\beta$	magic angle, 54.7°
$r$	distance
$t$	time
$T$	temperature
$T_1$	spin-lattice relaxation time in the laboratory frame
$T_{1\rho}$	spin-lattice relaxation time in the rotation frame
$T_2$	Spin-spin relaxation time
$T_g$	glass transition temperature



## 1. Introduction

Fuel cells can convert energy from chemical reactions into electrical energy in an efficient, clean and quiet manner. Therefore the development of fuel cells as electric power sources for transportation and other purposes is of great interest. In a fuel cell, the cathode and anode compartments are separated by an electrolyte so that the electrochemical reactions can occur at the electrodes and generate electricity. The choice of the electrolytic separator depends on the chemical reaction and on the intended use for the electric power. For transportation applications, such as electric powered automobiles, the cells must have high energy efficiency in terms of the power generated per unit mass and per unit volume and must be stable over a certain lifetime (about 40000 hours at an operating temperature of about 90°C). To satisfy these requirements specially designed ionomers are used as membrane electrolytes in these fuel cells.

The introduction of Nafion, a perfluorosulfonic acid ionomer (PFSA), provided an important advance in this area, and permitted operation of H<sub>2</sub>/O<sub>2</sub> fuel cells at about 1 A/cm<sup>2</sup> and 0.7 V. Despite advantages of Nafion over most ionomers, durability and degradation as well as problems with low temperature operation are still important issues which limit the reliable and long term application of this polymer.

The main motivation of this work was to understand the chemical degradation mechanism in Nafion and Nafion-like membranes as well as finding the reasons for the better performance of short side chain PFSA ionomers and Nafion composite membranes. The

investigations are primarily based on solid-state NMR spectroscopy, since it gives access to both the chemical structure and mobility of perfluorinated polymers.

The present dissertation consists of seven chapters. After a short introduction in chapter 1, the second chapter reviews the current state of research on PFSA ionomers, with particular focus on the durability. Chapter 3 gives an introduction to solid-state NMR spectroscopy. In chapter 4, the structures of polymer membranes before and after the fuel cell test are examined by their  $^{19}\text{F}$  and  $^{13}\text{C}$  solid-state NMR spectra. For a better understanding of the observed structural changes and the effect of different external parameters, in chapter 5 an ex-situ degradation test is introduced to expose membranes to flows of different gases with a controlled temperature and humidity. On the basis of the acquired results, possible mechanisms for the radical formation and radical attacks to Nafion are discussed. In chapter 6, by applying the traditional Fenton ex-situ test, the degradation of different fluorinated polymer is compared and the reasons for the better performance of the short side chain polymers are discussed. In chapter 7, the polymer mobility of Nafion with and without  $\text{SiO}_2$  particles is studied, and the effect of oxide particles on the performance of the membrane is discussed.

## **2. Introduction to Polymer Electrolyte Membranes**

### **2.1. PEM fuel cells**

Fuel cells are considered to be one of the solutions for the future problem of energy conversion. A fuel cell is a device in which the chemical energy of a fuel and an oxidant is directly converted into low voltage D.C. electricity. Fuel cells have high efficiencies, high energy densities and low or zero emission. They are quiet, clean, and modular and can be made in a variety of sizes [1].

The discovery of the operational principle of the fuel cells is ascribed to Schönbein and Grove [2]. But the first practical fuel cell applications were in the U.S. space program in the early 1960s. Even after that, the limited performance and lifetime which were the result of the membrane electrolyte degradation did not let the fuel cells to be commercialized until the performance and lifetime of the cells were significantly improved by developing perfluorosulfonated ionomer (PFSA) membranes.

Historically, fuel cells are classified by the nature of the electrolyte and/or by the temperature of operation. Thus, one distinguishes between alkaline or acidic, or low temperature (up to approx. 100°C), medium (up to approx. 200°C) and high temperature (up to approx. 1000°C) fuel cells [3]. Table 2.1 compares the components and properties of different fuel cells.

Generally, in a fuel cell, the anodic and cathodic reactants are fed into their respective chambers and an electrolyte layer is placed between the two electrodes. The half cell reaction at the anode yields electrons, which are transported through the external circuit and reach the cathode. These electrons are then transferred to the cathodic reactants. The circuit is completed by the transport of ions from one electrode to the other through the electrolyte.

In PEMFCs, a multilayer assembly of the membrane is placed between two porous, electrically conductive electrodes. This complete unit is called membrane electrode assembly (MEA). The MEA is located between two flow plates which distribute the reactant gases across the surface of the MEA and collect the electrical current from the MEA.

**Table 2.1.** Types of fuel cells.

Fuel Cell System	Electrolyte	Fuel	Oxidant	Operating Temperature	Electrical efficiency
<b>AFC</b> (alkaline fuel cell)	30% KOH	H <sub>2</sub>	O <sub>2</sub>	60-90°C	60 - 70%
<b>PEMFC</b> (polymer electrolyte membrane fuel cell)	H <sup>+</sup> conducting membrane	H <sub>2</sub>	O <sub>2</sub> , Air	50-100°C	50 - 68%
<b>DMFC</b> (direct methanol fuel cell)	H <sup>+</sup> conducting membrane	CH <sub>3</sub> OH	O <sub>2</sub> , Air	80-130°C	20 - 30%
<b>PAFC</b> (phosphonic acid fuel cell)	concentrated H <sub>3</sub> PO <sub>4</sub>	natural gas, bio gas, H <sub>2</sub>	O <sub>2</sub> , Air	160-220°C	55%
<b>MCFC</b> (molten carbonate fuel cell)	molten Li <sub>2</sub> CO <sub>3</sub> , K <sub>2</sub> CO <sub>3</sub>	natural gas, bio gas, H <sub>2</sub>	O <sub>2</sub> , Air	620-660°C	65%
<b>SOFC</b> (solid oxide fuel cell)	ZrO <sub>2</sub> /Y <sub>2</sub> O <sub>3</sub>	natural gas, bio gas, H <sub>2</sub>	O <sub>2</sub> , Air	800-1000°C	60 - 65%

Since the voltage of a fuel cell is quite small, many cells have to be connected in series to produce a useful voltage. Such a collection of fuel cells in series is called a “stack”, and it is achieved by connecting the edge of each anode to the cathode of the next cell or by

connecting the whole surface of one cathode to the whole surface of the next cell anode. The latter case is called a “bipolar plate”.

For the case of a reversible fuel cell running on hydrogen and oxygen, the following electrochemical reactions occur at the two electrodes:

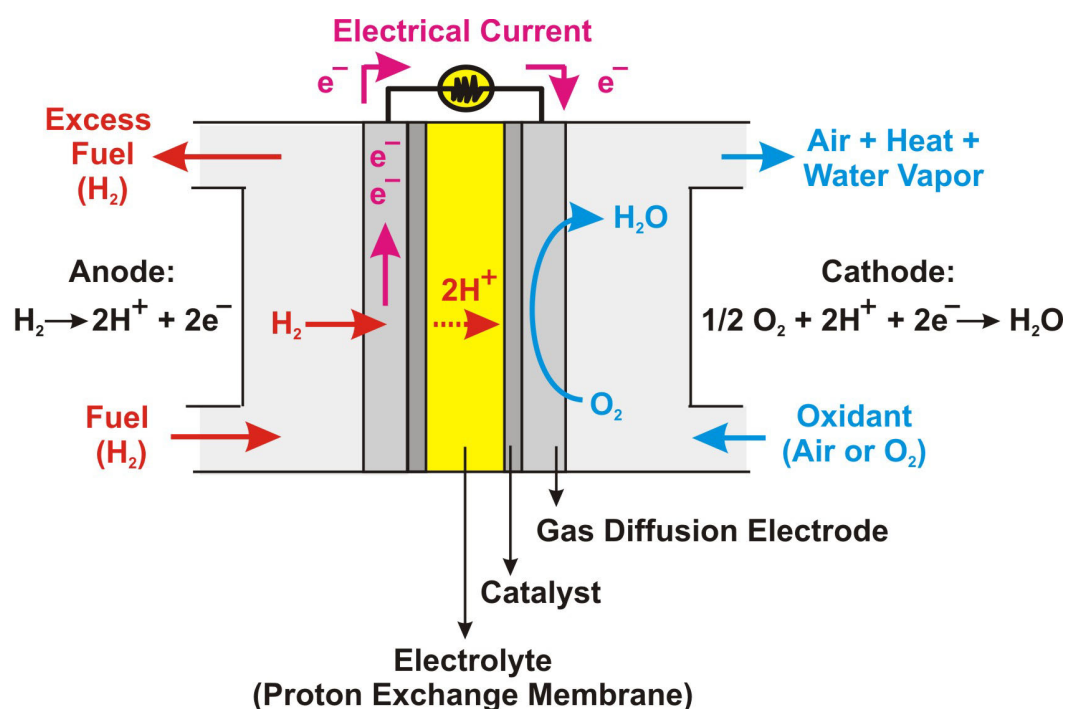
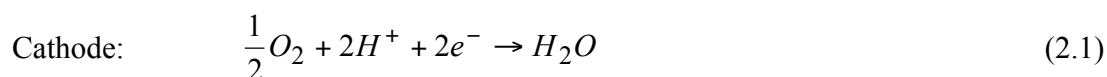


**Figure 2.1.** PEMFC components and its reactions

On the anode side, hydrogen diffuses to the anode catalyst where it dissociates into protons and electrons. The protons are conducted through the membrane to the cathode, and the electrons travel in an external circuit, because the membrane is electrically insulating. On the cathode catalyst, oxygen molecules react with the electrons and protons to form water.

## 2.2. PEM fuel cell components

The main components of a PEM fuel cell are gas diffusion layer (GDL), electrodes and polymer electrolyte membrane.

A gas diffusion layer is a porous layer between the catalyst layer and bipolar plates which provides a pathway for reactant gases from the flow field channels to the catalyst layer as well as the product water from the catalyst layer to the flow field channel. It provides mechanical support to the MEA, and its chemical and thermal conductivity helps completing the electrical circuit as well as removing the produced heat from the system.

A fuel cell electrode is a thin, porous catalyst layer with a hydrophobic surface where the electrochemical reactions take place. These properties are necessary to minimize the cell potential losses due to the rate of proton transport, and effectively remove the product water. The most common catalyst in PEM fuel cells for both oxygen reduction and hydrogen oxidation reactions is platinum. Generally, it is important to have small platinum particles with large surface area which are finely dispersed on the surface of the catalyst support, typically carbon powders with high mesoporous area. In order to assemble the membrane and catalyst layer and to prepare a MEA, the catalyst layer firstly is deposited to the gas diffusion layer (typically carbon fiber paper or carbon cloth) and then hot pressed to the membrane.

The fuel cell membrane of the PEM fuel cell is an electronic insulating but proton conducting polymer. High proton conductivity, high chemical and thermal stability, good mechanical properties, low water drag, fast kinetics for electrode reactions, low gas permeability, low cost and availability are the requirements that have to be fulfilled for a polymer electrolyte membrane to be used in a fuel cell.

## 2.3. Nafion membrane

Typically, the membranes for PEM fuel cells are made of perfluorocarbon-sulfonic acid ionomers. This is essentially a copolymer of tetrafluoroethylene (TFE) and various types of perfluorosulfonate monomers. The best known membrane material is Nafion [4]. This

polymer is the first of a class of synthetic polymers with ionic properties which are called ionomers. It was discovered in the late 1960s by Walther Grot at DuPont [5]. The membrane consists of a perfluorinated backbone (for chemical stability) and pendant chains terminated by sulfonic groups,  $\text{SO}_3\text{H}$  (for ionic conductivity) [4]. Therefore, it combines two extremes: the perfluorinated sulfonic acid side chains are strongly hydrophilic, while the perfluorinated backbones are strongly hydrophobic.

The conductivity of Nafion comes from the protons of the sulfonic acid groups. The hydrated  $-\text{SO}_3^-$  side chain end groups and the absorbed water provide the media for the transport of protons. The excellent chemical resistance of Nafion comes from the PTFE like backbone: the CF bond energy is one of the highest known values, 480 kJ/mol. The combination of the proton conductivity and the chemical resistance makes Nafion widely useful for electrochemical processes.

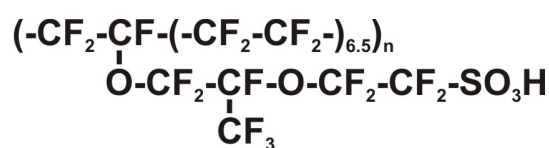


**Figure 2.2.** Chemical structure of Nafion in the sulfonic acid form

Nafion membranes are usually characterized by their equivalent weight and thickness, e.g. the designation “117” means that the film has an equivalent weight of 1100 g/mol and a normal thickness of 0.007 inch. The equivalent weight (EW) is the weight, in grams, of dry Nafion per mol of sulfonic acid groups. The number of  $\text{CF}_2-\text{CF}_2$  (tetrafluoroethylene, TFE) repeat units is an average value due to the usually unknown comonomer sequence distribution along the polymer chains. For example, on average for each  $\text{SO}_3\text{H}$  group there are 6.5 TFE repeating units in Nafion 117. In other words, the side chains are separated by 14  $\text{CF}_2$  units along the backbone of Nafion 117.

### 2.3.1. Synthesis of Nafion

Nafion films are produced by both extrusion and solution casting processes. Extruded Nafion is synthesized by the copolymerization of tetrafluoroethylene (the monomer of Teflon) and a derivative of a perfluoro (alkyl vinyl ether) with sulfonyl acid fluoride. The



universally accepted morphological model for the solid-state structure of Nafion has not been given due to the low crystallinity and complexity of co-organized crystalline and ionic domains.

The generally accepted picture is an aggregation of the polar perfluoroether side chains containing sulfonic acid groups due to Coulombic interactions which leads to a nanophase separated morphology. These ionic domains are distributed over the nonpolar PTFE matrix. In addition, randomly distributed crystalline domains which have a crystal structure similar to PTFE are detected (for PTFE crystallinity is 100%, for Nafion 117 is ~3-12%) [4]. This complex phase-separated morphology has been the target of several investigations which led to different models.

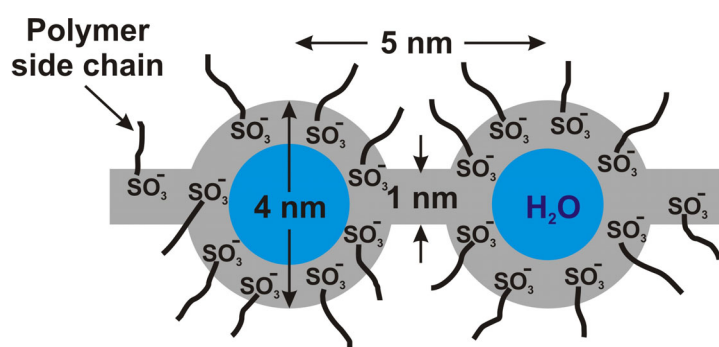


**Figure 2.4.** Cluster-network model of Gierke for the morphology of hydrated Nafion [6].

The cluster-network model of Gierke et al. can be considered as the most widely referenced model [7]. Based on small-angle X-ray scattering (SAXS) studies and several further assumptions, the model proposes that there are clusters of sulfonate terminated side chains that are organized as inverted micelles. These micelles are interconnected by a network of short and narrow channels which allow water and ion transport. Another model proposed by Yeager and Steck depicts a three-phase model based on a fluorocarbon phase, an interfacial region and ionic clusters [8]. Yeo and Eisenberg proposed one of the first theories which explained the formation of ionic clusters in organic polymers [9]. The other models that have been proposed to date include a core-shell model by Fujimura et al. [10,11], a rod-like model by Rubatat et al. [12,13], a sandwich-like model by Haubold et al. [14] and an inverted-micelle cylinder model by Schmidt-Rohr et al. [15]. Common in all

these models is the presence of an ionic cluster network; the models differ in the cluster geometry and distribution.

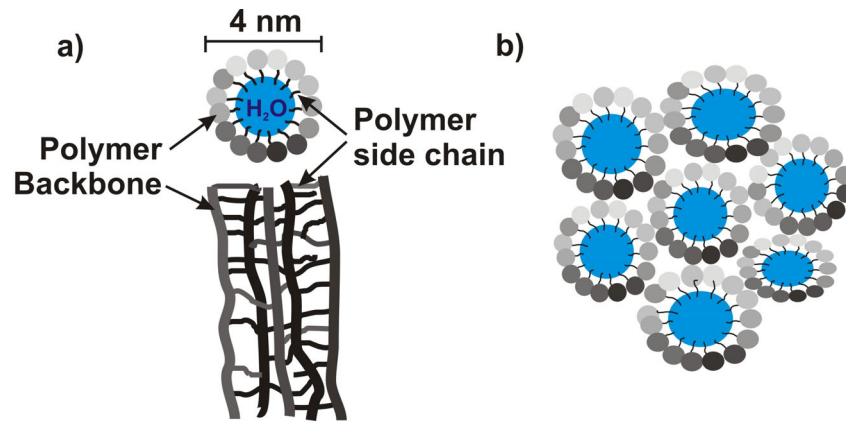


**Figure 2.5.** Parallel water-channel (inverted-micelle cylinder) model of Nafion [15].

a) Two views of an inverted-micelle cylinder, with the polymer backbones on the outside and the ionic side groups lining the water channel. Shading is used to distinguish chains in front and in the back. b) Schematic picture of the approximately hexagonal packing of several inverted-micelle cylinders.

### 2.3.3. Water content and conductivity

The water content in the Nafion membrane is normally a function of temperature and relative humidity. But since different pre-treatments cause changes in the morphology of membrane, the absolute water content value depends strongly on the membrane pre-treatment.

Membranes in PEM fuel cells are generally water saturated to keep the conductivity high. As the PEMFC operates at about 80°C, the water is produced as a liquid and is transported out of the fuel cell by excess oxidant flow. In the cell, water transport processes are a function of the current and the characteristics of both the membrane and electrodes. Water transfer through the membrane is dependent on the difference between the relative humidity at the cathode and anode side.

The proton conductivity depends on the water content, diffusion coefficient and concentration of the excess protons. High concentration of water molecules in the system

together with the relatively large diameter of the interconnecting channels between ionic clusters promotes water diffusion. For Nafion, a decay in proton conductivity with decreasing humidity as well as the water content has been reported [16-18]. At a higher degree of hydration, the large water content in the system shields the changes associated with the sulfonic acid anions and preserves the hydrogen bond network, leading to quicker reorientation of water molecules and formation of a continuous pathway for the protons across the medium. Therefore, in a well-hydrated membrane, the major proton conduction mechanism is structure diffusion. At low humidity levels, there are fewer water molecules per sulfonic acid group, resulting in concentration increase and poor shielding of the protonic charge carriers. In this case, hydrogen bonds get tighter which leads to a reduced rate of bond breaking and forming processes. Therefore, intermolecular proton transfer is suppressed and protons preferentially diffuse as a part of bigger species (vehicle mechanism) [19,20].

## **2.4. Limitations of Nafion as a fuel cell membrane**

### **2.4.1. Low temperature operation problems**

Tests in PEMFCs indicate that more than about 10 ppm of CO in the gas stream have an impact on cell performance [21]. The reason is the poisoning of platinum by carbon monoxide. At relatively low operating temperatures, the affinity of CO molecules to the platinum surface is very high. Therefore the dual site replacement of one H<sub>2</sub> molecule by two CO molecules on the Pt surface can happen. Owing to the fact that the absolute free energy of adsorption of CO on Pt has a larger positive temperature dependence than that of H<sub>2</sub>, lower CO coverage can be achieved by raising the cell temperature above 100 °C. The CO tolerance will be drastically enhanced, from 10-20 ppm at 80 °C to 1000 ppm at 130 °C. This high CO tolerance makes it possible for a fuel cell to use hydrogen directly from a reformer and also leads to a reduction in electro-catalyst loadings.

On the other hand, the proton conductivity strongly increases with increasing the concentration of absorbed water and falls with decreasing water content. Therefore membranes in PEM fuel cells are generally water saturated to keep the conductivity high.

This is normally done by humidification of the feed gases and also by production of water at the cathode by electrochemical reduction of oxygen. If the PEMFC operates, the protonic current through the membrane produces an electroosmotic water current which causes a decrease of water at the anode, and an increase of the membrane resistance. Both the electroosmotic drag and the water generation build up a large concentration gradient across the membrane which causes back diffusion of water from the cathode to the anode. Some water is transported out of the fuel cell by excess oxidant flow. Thinner membranes are required in order to assure sufficient back diffusion.

Operation of a PEMFC at a temperature close to the boiling point of water involves the problem of a double phase water system. When the humidification is too high, water condenses and the gas diffusion electrodes are flooded. This problem can be solved by operating the fuel cell above the boiling point of water.

The equilibrium partial vapor pressure of water can't be compensated above 100 °C at normal atmospheric pressure. In order to keep the membrane hydrated, the total cell pressure has to be raised above 1 atm. Pressurized operation results in a large loss in the system efficiency because of the energy needed to compress the oxidant air. Membranes that are capable of operating at reduced humidity would not require pressurization at elevated temperatures.

#### **2.4.2. Durability and degradation issue**

The most significant problem for commercialization of polymer electrolyte membrane fuel cells (PEMFC) is their relatively short lifetime. Extension of the lifetime for all fuel cell components is therefore absolutely mandatory for the use of fuel cells as economical alternative energy conversion systems, with high reliability and low maintenance costs.

It has been demonstrated that the failure of fuel cells results from the interplay of different degradation routes within the various fuel cell components. Hence, dissolution of the platinum catalyst particles [22-24], corrosion of the carbon catalyst support [25-28], delamination of the electrode and membrane layers [29,30], decrease of the electrochemically active surface areas of the catalyst, and the increase of the Pt particle size

[31] are frequently discussed.

The major reason for a reduced fuel cell performance, however, is the degradation of the polymer electrolyte membrane. The chemical composition and structure play an essential role for the performance of fuel cell systems, and the materials have to meet several requirements in order to become applicable as fuel cell membranes [32-34]. Sulfonated fluoropolymers or aromatic polymers were found to be suitable candidates, out of which Nafion is still a kind of bench-mark material [4].

When it comes to membrane breakdown, three contributions, namely mechanical, thermal and chemical degradation, are distinguished. Hence, various mechanical degradation modes were proposed to explain experimental observations, such as released fluoride detected in the waste water [35-42], membrane thinning [43], and pinhole/crack formations [41,44]. They include (i) tiring behavior after the membranes were subjected to rapid dehydration-rehydration cycles due to, for instance, rapid current density changes [42,45], (ii) concentrated stress areas, and (iii) localized heat spots caused by penetration of catalyst particles into the membrane [46].

From thermogravimetric studies the chemical structure of Nafion membrane is reported to be thermally stable up to temperatures of about 280 °C, above which the sulfonic groups are split off [47,48]. However, extended durability studies on hydrated membranes, kept in water over a period of up to 10 years, revealed structural and chemical changes even at ambient temperature.

Chemical degradation of membranes is generally thought to play the most important role for fuel cell failures [30,35,36,43,49]. Experimental observations such as decrease of the ion exchange capacity [48], changes in pH [36], conductivity [36,50] and membrane thickness [43] as well as the presence of fluoride in the released water [35-43] are typically considered as a strong indication for chemical degradation of the polymer electrolyte membrane. In the meantime, a variety of experimental techniques, such as broadband dielectric spectroscopy [51], EPR [29,30,49,52-59], FTIR [35,40,44,47,52,60-63], Raman [52], UV-visible [52], liquid [44,64,65], solid-state [40,44,61] NMR and mass spectroscopy [64,65], XPS [31,46,60,66,67], wide angle and small angle X-ray diffraction [31,46], TGA

[47,48,68], TEM [69] and SEM [44], has been used for identification and characterization of the degradation products, including the remaining membrane and/or the released components.

Degradation studies of membranes are either done under in-situ or ex-situ conditions. In the first scenario, the membrane operates in a fuel cell as a part of the membrane electrode assembly (MEA), and degradation is studied a) directly during the fuel cell operation or b) externally at the end of the test after removal of the membrane from the MEA. Ex-situ tests do not require the use of fuel cell set-ups. Rather, the polymer electrolyte membrane is subjected to suitable test conditions which are assumed to mimic the situation (and chemical reactions) during fuel cell operation. In ex-situ tests, it is principally possible to accelerate the reactions, by which the testing time may be reduced considerably. However, due to the complexity of the reaction scheme, partial reactions may be accelerated to different extents, and one has to be careful to generalize conclusions. On the other hand, ex-situ tests allow for easier variation of experimental parameters, and this freedom makes it frequently possible to obtain details of degradation mechanisms. Therefore, the combined use of both in-situ and ex-situ protocols may lead to a more detailed and reliable understanding of the degradation reactions taking place in PEM fuel cells. Finding suitable ex-situ tests in which the system parameters are well controlled appears therefore an interesting option for obtaining complementary information. In the ideal case, the influence of each experimental parameter can be examined separately or in combination with other parameters. To do this in a meaningful way, some knowledge about the mechanisms responsible for membrane degradation in a fuel cell under operating conditions is needed.

In a running fuel cell, the membrane is subjected to a chemically oxidizing environment on the cathode side, and chemically reducing environment on the anode side. Any cross-over of gases between anode and cathode may lead to radical formation. In fact, it is the attack by radicals which is considered as the main source for chemical degradation of PEMFC membranes. This assumption is directly supported by a recent study which proved the formation of HO• and HOO• radicals during in-situ fuel cell experiments [49]. They originate from both electrochemical and chemical reactions, and they occur on the anode as well as on the cathode side. Also, the observation of a polymeric radical has been reported

for Nafion where the unpaired electron is located at the tertiary backbone carbon atom that is linked to the pendant side chain [30,56]. Chain end radicals with structures like  $-O-CF_2-CF_2\cdot$  have been also identified by EPR, when Nafion membranes, saturated with metal counter ions, were exposed to UV radiation in the presence of  $H_2O_2$  [56].

During other EPR studies on X-ray irradiated Nafion the formation of peroxy radicals was detected [52]. XPS investigations on Nafion confirmed that the polymer backbone as well as the sulfonic acid groups in the side chains are susceptible to X-ray damage, although the decomposition of the side chain is faster than that of the PTFE backbone [66-68]. For the samples treated with Fenton's reagent, it has been shown that the decrease of the peak intensities for the fluorine and sulfur signals in the XPS spectrum is consistent with the detection of fluoride and sulfate ions during fuel-cell tests [60]. Likewise, FTIR spectra proved the formation of C=O and S-O-S units in the degraded membranes [60]. An IR band, characteristic for S-O-S units, was observed after soaking a Nafion membrane in a  $H_2O_2$  solution for 30 days [62]. The formation of such structural components are thought to be a result of cross-linking of sulfonic acid groups in the side chains [61,62]. Band intensity changes associated with C-O, C-S and  $SO_3^-$  stretching modes after the X-ray irradiation test indicated breaking of C-S and C-O bonds.  $^{19}F$  NMR and mass spectrometric analyses of the degradation solution exhibited fluorinated fragments largely resembling the Nafion side chain structure [64].

## 2.5. Nafion alternatives

Low proton conductivity at low relative humidity, high methanol permeability and poor mechanical properties above  $90^\circ C$  as well as degradation and durability has been mentioned as the main obstacles for commercializing the polymer electrolyte fuel cells with the known ionomeric membranes like Nafion. Therefore, new types of proton-conducting membranes, which can work in the temperature range of 90 to  $140^\circ C$  and which have a higher durability, have to be developed. The proposed solutions to overcome the mentioned problems can be the developments of membranes made of new ionomers or improvement of the known ionomeric membranes. Based on the second case, two possibilities for improving the performance of Nafion will be mentioned in the following.

### 2.5.1. Short side chain perfluorosulfonic acid ionomers

In the mid 1980s Ballard Power Systems showed significant improvements in fuel cell performance using ionomer membranes obtained from Dow Chemical. This ionomer is perfluorinated and structurally similar to Nafion, but has a shorter pendant side chain which carries the functional ion transporting group. It is known as the short side chain (SSC) ionomer corresponding to Nafion as the long side chain (LSC) ionomer.

Recently, Solvay Solexis has restarted the development of polymer electrolyte membranes based on SSC perfluorinated ionomers. The commercial name for the product of this company is Hyflon Ion. The Nafion and Hyflon Ion membranes differ in the lengths of the side chains. The side chain of Hyflon Ion does not contain the  $-O-CF_2-CF(CF_3)-$  segment next to the polymer backbone. The shorter side chains of the Hyflon Ion structure results, compared to Nafion, in a higher concentration of  $SO_3H$  groups for the same degree of branching and higher ion exchange capacity.

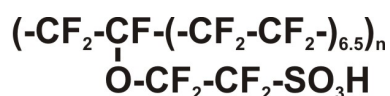


**Figure 2.6.** Chemical structure of Hyflon Ion

It has been shown that the short side chain membranes have a higher degree of crystallinity and higher glass transition temperature ( $T_g$ ) as compared to Nafion [70,71]. These properties have been suggested to be the reason for less swelling, higher conductivity, lower electroosmotic drag and better mechanical stability especially at high temperature and, as a consequence, better performance in the temperature range between 80 and 120 °C [72].

### 2.5.2. Nafion/Oxide composite membranes

Here, composite membranes are considered which consist of a polymeric ionomer (like Nafion) in which inorganic solid particles (such as  $SiO_2$ ) are dispersed. The properties of these composite membranes not only depend on the nature of the ionomer and the solid used, but also on the amount [73-76], homogeneous dispersion [76-79], size [77,78],

surface properties [76,77,80,81], and orientation of the solid particles dispersed in the polymeric matrix. In ionomers, such as Nafion, where well-separated hydrophilic and hydrophobic domains are present, the distribution of the dispersed particles in the different domains is also important.

Nano- and micro-composite membranes can be prepared following two different procedures: (a) dispersion of micro- or nano-sized filler particles in an ionomer solution followed by casting or (b) generation of the filler particles within a preformed membrane or in an ionomer solution (sol-gel process). In the casting procedure, the solids are first ground until a fine powder is obtained and then dispersed under strong stirring in an organic solution of the polymer. The membrane is obtained by film casting and solvent elimination. Using this procedure, one should avoid the formation of agglomerated particles inside the polymeric matrix which cause a non-homogeneous dispersion. In-situ formation of inorganic fillers in preformed membranes is done by incorporation of a filler precursor in the polymeric matrix by simple impregnation (if the filler is neutral) or by ion-exchange reaction (if the filler is a cationic or an ionic species) and subsequent treatment of the membrane with the necessary reactants to convert the precursor into the final inorganic filler. If this reaction is an acid-catalyzed hydrolysis, then the ionomer itself can act as a catalyst, and external reactants are not necessary. A typical example is the impregnation of ionomeric membranes with tetraethoxysilane (TEOS), which is then converted into the final filler  $\text{SiO}_2$  [82-84]. From a practical point of view, in-situ formation of the filler appears to be a suitable way to modify commercial membranes, which are prepared by extrusion.

The first nano-composite Nafion- $\text{SiO}_2$  membranes were obtained by TEOS [82]. Later, other sources for preparing composite polymers with  $\text{SiO}_2$  particles have been used [73-79,83-91]. Bifunctional silica with both  $-\text{SiOH}$  and  $-\text{SO}_3\text{H}$  functional groups, and mesoporous silica are some examples for this kind of work. Because of different dispersion and size of the silicon oxide particles, a range of silica content from 3 to 9 w/w% was reported in literature for the optimal performance of composite membrane [75,78,88,92].

Comprehensive investigations of the structure of these composites have been done. Studies of nano-composites by FTIR spectroscopy [82], dielectric relaxation [84], thermal analysis [83], and small angle X-ray scattering (SAXS) [80,89] suggested that the nano-phase-

separated morphology of Nafion acts as a template for the growth of the incorporated silica phase. More specifically, the SAXS peak characteristic of quasi-ordered clusters in pure Nafion persisted in the composites filled with silica. A significant increase of the average ion clusters dimension was observed for the composite SiO<sub>2</sub> membrane. The thermogravimetry analysis (TGA) results of Nafion-SiO<sub>2</sub> membranes [88] have indicated that the composite membranes are thermally stable up to 170°C. Different water domains presented in bulk membrane were assigned by ATR-FTIR and micro Raman measurements [88,90]. X-ray diffraction (XRD) results showed incorporation of particles into the Nafion membrane could increase the crystallinity of the Nafion recast membrane [79,91]. These results were also obtained from the FTIR absorption spectra where narrower peaks were observed for the composite membrane (9 w/w% SiO<sub>2</sub>) with the best performance as compared to recast Nafion. Increase of the SiO<sub>2</sub> mass fraction to more than 9 % led to peak broadening and therefore a decrease in crystallinity [88]. It has been reported that composite membranes with SiO<sub>2</sub> are characterized by an improved water-uptake [75,79,85-87,91,93-96] and reduced methanol permeability [76,80,97,98]. Some researches claimed that the conductivity of composite Nafion was in general higher than for Nafion [75-77,90], but it is mostly reported that for the typical condition the composite membrane conductivity is very close to that of the Nafion [78,79,91,99] but higher at elevated temperatures [93,95] and at low relative humidity [78,79,87,91].

## 2.6. Open questions and missing investigations

In order to develop a fuel cell with a high performance and high durability, one has to understand the reason for the failures of Nafion as an available bench mark material. This should include the understanding of possible chemical and morphological changes in Nafion when the membrane is operating in normal and critical situations (such as low relative humidity and high temperatures). In general, the main reason for the reduction in fuel cell performance is the chemical degradation of the polymer electrolyte membrane. Despite the detailed observations which are mentioned in literature, the various reactions and structural changes during chemical degradation are far from being completely understood. Till now all the expectations about the chemical changes in the polymer membrane are based on the observation of released fragments from the polymer or the

direct measurement of fluoride ion emission. However, a complete picture of the Nafion structure after chemical degradation is still missing. Based on the whole knowledge about degradation and the role of radicals in membrane degradation one should find out the different possibilities for the radical formation inside the fuel cell. Ionization radiation [35], Fenton reaction [29,36,40,51,54,55,60,100], X-ray radiation [52,66,67], cleavage of hydrogen peroxide by UV light [54-56] or heat [54] are different methods for radical formation in ex-situ degradation experiments. But what are the sources for the radical formation in a running fuel cell? The oxygen reduction reaction [36,49,101] or the direct reaction of H<sub>2</sub> and O<sub>2</sub> gases [39,43,59,102] appear as possible sources. Only if the conditions for the occurrence of these reactions and the parameters that can control them are clarified, one is able to control a fuel cell system and to reduce the radical formation to a minimum. Further, one has to understand which are the potential positions for the radical attacks in the polymer structure. In order to get this information not only a correct degradation test is needed but also a suitable tool for the characterization of small changes in the chemical structure of the polymer is required. It also gives an idea about the weak points in the chemical structure of Nafion that may be improved in order to design new materials.

As outlined, there is evidence for the better performance of short side chain perfluorinated polymers or of Nafion/oxide composite membranes. The former works showed the limits and advantages of these polymers. Explanations of the reasons for the better performance are missing or sometimes contradictory to other works. Probably the effect is not only related to the chemical structure of polymers but also to the morphology which leads to a higher conductivity and better water management. Studying the polymer chain motions for any of these membranes in different operating situation, such as high or low temperatures and different water contents, and the effect of these parameters on the proton conductivity is therefore necessary and may led some further light on the open questions.

## **2.7. Why to choose solid-state NMR spectroscopy?**

As demonstrated by numerous applications on quite different types of materials, solid-state NMR spectroscopy is a powerful tool for elucidation of the structural and dynamical

features of solids, and it can be applied to almost any type of inorganic, organic, polymeric and biological materials [103-107].

For synthetic polymers with long chain molecules composed of large number of repeated units, the properties strongly depend on both the molecular structure and the organization of the macromolecules in the solid-state. Macroscopic as well as microscopic properties of polymers, which are determined by the phase structure, morphology, molecular order and molecular dynamic features of the polymers, are the result of the physical and/or chemical processing following the chemical synthesis. Scattering techniques and microscopy are suitable methods for probing structural features, while relaxation techniques are usually applied to provide dynamic information on the materials. Although spectroscopic techniques, such as IR, UV, Raman, etc., are also widely used for such materials, solid-state NMR is a suitable technique for both structure and dynamic investigation of polymeric solids. It is also applicable for situations in which other techniques do not work. For example, polymers are usually not perfectly crystalline, and this is crucial for some scattering techniques. The responses of the nuclear spins to the internal and external magnetic fields provide a versatile molecular level probe for studying even such materials.

The low resolution of solid-state NMR due to the absence of fast isotropic molecular motions as in solutions limited early solid-state NMR studies. But cross-polarization (CP) [108], magic angle spinning (MAS) [109,110], and the ingenious application of multiple pulses techniques make the orientation-dependent interactions in solids valuable for probing the structural and dynamical information of solids, and makes NMR a valuable tool for the study of solid materials.

## **2.8. Literature review on NMR studies of Nafion**

### **2.8.1. $^1\text{H}$ & $^2\text{H}$ NMR**

Several reports have been published on  $^1\text{H}$  NMR [111-119] and  $^2\text{H}$  NMR [113-115,120] investigations of Nafion. It has been shown that the chemical shift and the linewidth of proton and deuteron peaks depend on the water content of Nafion [111-115,120], therefore any of these parameters may be used as an indirect measure of the water content. For

instance, by increasing the temperature, the linewidth of the proton and deuteron peaks decrease which shows that the mobility of water molecules becomes higher and the chemical environments become more homogeneous [116,117,120]. Proton exchange between water and sulfonic acid groups has been confirmed by high-resolution  $^1\text{H}$  solid-state NMR [119]. The proton mobility was found to depend not only on the water content but also on the temperature.

$^1\text{H}$  NMR relaxation time measurements on Nafion with different water contents over a wide range of temperature [121-124] indicated that there is a distribution of heterogeneous water sites in the membranes and the relaxation data is similar to the behavior predicted by the BPP theory for motions in isotropic liquids, although the detailed behavior of the system is not consistent with that theory [125]. In general it is found that by increasing the water content, the  $T_1$  (spin-lattice relaxation time) values increase [126]. The general trends for the deuteron relaxation data is similar to those in  $^1\text{H}$  NMR, but the deuteron relaxation times in the membrane is 5-6 times shorter than in aqueous solution [114]. The dependence of the relaxation data on the degree of hydration is reported also for deuteron relaxation times [120].

### 2.8.2. $^{19}\text{F}$ NMR

$^{19}\text{F}$  NMR studies of Nafion in different solvents [127] showed that separate signals from nuclei in the backbone and in the pendant chain can be detected [127]. The first  $^{19}\text{F}$  magic angle NMR spectra with different spinning speed from 5-35 kHz was reported by Dec et al. [128]. It was shown that in general going to the higher spinning speed as well as increasing the water content can decrease the linewidth of the spectra and increase the resolution [128]. The original assignment of  $^{19}\text{F}$  and  $^{13}\text{C}$  NMR resonances of Nafion, given by Dec et. al. [128], was corrected later by Chen and Schmidt-Rohr using two-dimensional (2D)  $^{13}\text{C}$ - $^{19}\text{F}$  heteronuclear correlation and  $^{19}\text{F}$  2D-exchange NMR experiments under 30 kHz magic-angle spinning [129]. This later assignment was then confirmed in a solution NMR study of Takasaki where the  $^{19}\text{F}$  and  $^{13}\text{C}$  assignments of Nafion was determined on the basis of the assignments of the model compounds in solution, and the analysis of spin couplings between  $^{19}\text{F}$  and  $^{13}\text{C}$  [130].

The molecular motions of the fluorocarbon backbone in Nafion membranes were studied through  $^{19}\text{F}$  NMR relaxation in different water content [123,131]. It was mentioned that because of the effect of water as a plasticizer as well as possible cross-relaxation effects between the  $^{19}\text{F}$  and  $^1\text{H}$  spin systems, interpretation of the  $^{19}\text{F}$  relaxation data for the hydrated acid is complicated. In contrast to  $^1\text{H}$  and  $^2\text{H}$  relaxation data, it is reported that the fluorine  $T_1$  and  $T_2$  values are almost independent of the level of hydration, and unaffected by the presence or absence of a hydrating medium [123,131]. Also, no distinction between  $\text{H}_2\text{O}$  and  $\text{D}_2\text{O}$  hydration was reported [131]. On the other hand, the observation of nonexponential  $T_1$  and  $T_{1\rho}$  decay is indicative of a heterogeneous system. Broad minima as well as very short relaxation times, and little changes with temperature were mentioned to be a characteristic of large solid polymers [131].

The motions of the perfluoroether side chains and the effect of the pendant chain on the ionomer mobility in Nafion were also evaluated by the sideband analysis in variable temperature solid-state  $^{19}\text{F}$  NMR [132]. A sideband analysis indicated that the side chain is more mobile than the main chain. This effect was also confirmed by comparing the linewidths for Teflon and Nafion [127]. Molecular level information from these analyses in combination with SAXS and DMA data support the assignment of the  $\beta$  relaxation process to the genuine  $T_g$  of Nafion, and the  $\alpha$  relaxation process to the onset of long range mobility of chains/side chains via a thermally activated destabilization of the electrostatic network [132]. A similarity in the relaxation behavior of the side and main chains was derived from  $^{19}\text{F}$  NMR relaxation data which can be explained with the dynamically coupled motions of the side chains and main chains [132]. The initial increase in  $T_{1\rho}$  as a function of increasing temperature has been attributed to backbone rotations that increase with increasing temperature [132]. The maxima observed in the  $T_{1\rho}$  plots was attributed a change in the dominant relaxation mechanism at that temperature [132].

### 2.8.3. Other NMR techniques

To study the water dynamics, pulsed-field-gradient (PFG) NMR has been frequently used on Nafion membranes [133-142] and Nafion containing solid oxide particles [143,144]. The PFG NMR data showed that the proton conductivity is consistent with the proton

diffusion rate and the proton mobility affects dominantly the proton conductivity. The self-diffusion constant of water and ethanol increases with increasing temperature as well as the volume fraction of water or ethanol [134]. In general, water molecules have a weak interaction with the polymer backbone [140], and Nafion seems to exhibit a very different behavior and can't be described as a porous material, but rather a swelling system where the diffusion takes place along cylinders in the early stages of hydration, and then becomes 3-dimensional at higher hydration states [137].

It has been found that the electroosmotic drag coefficient ( $K$ ), measured by electrophoretic NMR [145], increases with an increase of water content and temperature. The increase of  $K$  with increasing temperature is interpreted by a weakening of water-polymer interactions. The increase of  $K$  with water content was explained by an increase of hydrodynamic pumping for higher water contents. This effect appears to dominate that of proton transfer processes, which is more important at higher water contents and is expected to reduce  $K$ .

#### **2.8.4. NMR studies on degraded Nafion**

So far, there are only two reports on the application of solid-state  $^{19}\text{F}$  NMR spectroscopy for the study of Nafion degradation [40,44]. In both cases, the Fenton reaction has been used for preparing samples via ex-situ treatment. It is known that the ex-situ Fenton reaction generally gives rise to stronger degradation than in-situ tests. This was proven by ATR-FTIR results as well as direct measurement of fluoride ion emission. Surprisingly both former NMR investigations revealed no differences between the solid-state NMR spectrum of the membrane before and after ex-situ Fenton degradation [40,44]. However, the solution NMR on the Fenton's reagent after the degradation test, showed side chain fragments of the Nafion polymer [146]. Therefore, the degradation of the PEMs seems to initiate decomposition of the repeating units in the main chain or of the side chains.

Other information is available for the water self diffusion coefficient ( $D$ ) in the membranes as a function of the  $\text{H}_2\text{O}_2$  treatment time [62]. It has been reported that all the  $D$  values decreased with  $\text{H}_2\text{O}_2$  treatment time, and the trend resembles the findings for proton conductivity and water uptake [145].

### 2.8.5. NMR studies on Nafion/oxide composite membranes

Apart from  $^{29}\text{Si}$  NMR, there are only few reports about the NMR studies on composite membranes. Water and methanol transport behavior of filler-free Nafion membranes and Nafion-SiO<sub>2</sub> systems were investigated using nuclear magnetic resonance methods [81,143,144], including spin-lattice relaxation and pulsed-field-gradient spin-echo diffusion. A comparison between water and methanol self-diffusion coefficients revealed that the water mobility is higher than the methanol mobility in all membranes. Additionally, the inclusion of inorganic fillers improved both the solvent uptakes and the transport properties of the composite membranes relative to filler-free Nafion. It has been shown that by increasing the temperature, the  $T_1$  values of methanol and water increase.

Proton mobility in Nafion and Nafion/SiO<sub>2</sub> composites was studied using high-resolution solid-state  $^1\text{H}$  MAS NMR [147]. This study showed that low concentrations of filler or short permeation times are necessary to allow complete hydrolysis of filler in Nafion. The diffusion coefficients established by PFG NMR showed that Nafion/SiO<sub>2</sub> composite gave a higher diffusion coefficient than pure Nafion under dry conditions [119], although no differentiation in performance was observed when the membranes are hydrated [80,81,119].

### 3. Basics of NMR Spectroscopy

#### 3.1. Interaction with external magnetic fields

Any nuclei with an odd number of protons, neutrons or both have an intrinsic non-zero spin angular momentum,  $\vec{I}$ , and can be used in NMR spectroscopy. The state of the nucleus in terms of the nuclear spin wave function is described by the quantum numbers  $I$  and  $m$ , where  $m$  is the magnetic quantum number:

$$m = -I, -I+1, \dots, I-1, I \quad (3.1)$$

**Table 3.1.** NMR properties of the investigated nuclei in this work.

Nucleus	Spin	Natural abundance (%)	NMR frequency (MHz) at $B_0 = 9.39$ T	gyromagnetic ratio ( $10^{-7}$ rad T $^{-1}$ s $^{-1}$ )
$^1\text{H}$	1/2	99.98	399.952	26.752
$^{19}\text{F}$	1/2	100	376.331	25.18
$^{13}\text{C}$	1/2	1.108	100.568	6.728

The nuclei with spin possess a magnetic moment,  $\vec{\mu}$ , which interacts with its surroundings. The magnetic moment is related to the spin angular momentum via:

$$\vec{\mu} = \gamma\hbar\vec{I} \quad \text{and} \quad |\vec{\mu}| = \gamma\hbar\sqrt{I(I+1)} \quad (3.2)$$

where the gyromagnetic ratio,  $\gamma$ , is a constant specific for the nucleus under consideration.

A magnetic dipolar moment in a static magnetic field,  $B_0$ , has an energy of

$$E = -\vec{\mu} \cdot \vec{B}_0 = -\gamma\hbar I B_0 \quad (3.3)$$

which not only depends on  $\gamma$ ,  $\hbar$  and the magnitude of  $B_0$  but also on the relative orientation of  $\vec{\mu}$  and  $\vec{B}_0$ . In a Cartesian coordinate system, the static magnetic field direction is normally defined along the z-direction (homogenous magnetic field). The three spin operators associated with  $\vec{I}$  are  $\vec{I}_x$ ,  $\vec{I}_y$  and  $\vec{I}_z$ . The interaction between  $\vec{I}$  and  $B_0$  is called the Zeeman interaction with the following Hamiltonian:

$$\hat{H}_Z = -\gamma\hbar\vec{I}\vec{B}_0 = -\gamma\hbar \begin{pmatrix} I_x \\ I_y \\ I_z \end{pmatrix} \cdot \begin{pmatrix} 0 \\ 0 \\ B_0 \end{pmatrix} = -\gamma\hbar I_z B_0 = \hbar I_z \omega_0 \quad (3.4)$$

The precession frequency associated with the Zeeman interaction is called the Larmor frequency  $\omega_0 = -\gamma \cdot B_0$ .

A sample containing spin 1/2 nuclei has two states (energy levels) with the nuclear spin distributed between them. The distribution is given by the Boltzmann distribution which describes the probability of occupation of the different states:

$$\frac{N_-}{N_+} = e^{-\frac{\Delta E}{kT}} \quad (3.5)$$

where  $k$  is the Boltzmann constant and  $T$  is the temperature in Kelvin.  $N_+$  is the number of spins in the lower energy level and  $N_-$  is the number in the upper energy level. The total number of spins is given by  $N = N_{1/2} + N_{-1/2}$ , and the difference in population is:

$$n = N_{1/2} - N_{-1/2} \quad (3.6)$$

$$n = N \frac{1 - e^{-\frac{\Delta E}{kT}}}{1 + e^{-\frac{\Delta E}{kT}}} \quad (3.7)$$

In the high temperature limit (nearly always a good approximation in NMR),  $\frac{\Delta E}{kT} \ll 1$ , the population difference is  $n = N \frac{\Delta E}{2kT}$ . The separation of  $m = \pm 1/2$  levels is  $\Delta E = E_{-1/2} - E_{1/2} = \hbar\omega_0$  which is the energy of the  $+1/2 \leftrightarrow -1/2$  transition (Figure 3.1).

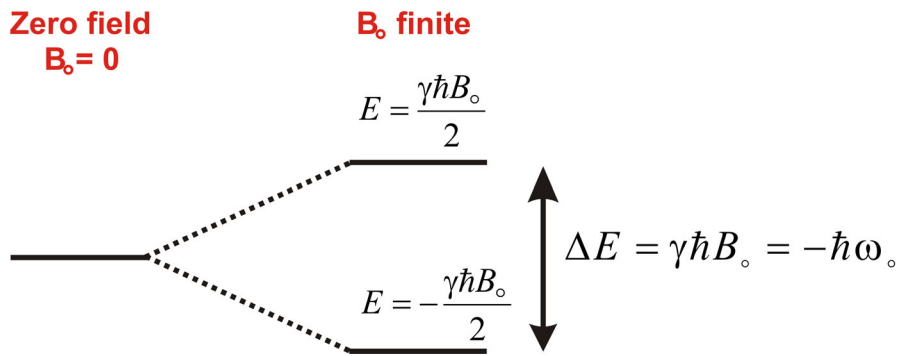


**Figure 3.1.** Energy level diagram of a spin 1/2 nucleus showing the Zeeman interaction.

The signal in NMR spectroscopy is proportional to the population difference between the states, as described by Equation (3.7). In order to change the population of the spin states a radio frequency field ( $rf$ ) is applied along the x-axis perpendicular to the static magnetic field in the laboratory frame (see Figure 3.2). The  $rf$  magnetic field is time dependent. The sample is irradiated with a linearly polarized  $rf$  field of strength  $B_1$ , frequency  $\omega_{rf}$  and phase  $\varphi$ .

$$B(t) = B_1 \cos(\omega_{rf}t + \varphi) \quad (3.8)$$

The Hamiltonian for a  $rf$  field applied along x-axis is:

$$\hat{H}_{rf} = -\gamma\hbar \begin{pmatrix} I_x \\ I_y \\ I_z \end{pmatrix} \cdot \begin{pmatrix} B(t) \\ 0 \\ 0 \end{pmatrix} = -\gamma\hbar B_1 I_x \cos(\omega_{rf}t + \varphi) \quad (3.9)$$

$$\hat{H}_{rf} = \hbar\omega_1 I_x \cos(\omega_{rf}t + \varphi) \quad (3.10)$$

When the radio frequency field oscillates close to the resonance frequency  $\omega_0$ , which corresponds to the Zeeman energy splitting, transitions between the spin states will occur.

In pulsed NMR experiments the spin system is excited with a short *rf* pulse near resonance and the system is measured afterwards. The total external Hamiltonian from the applied fields is then:

$$\hat{H}_{ext} = \hat{H}_Z + \hat{H}_{rf} \quad (3.11)$$

$$\hat{H}_{ext} = \hbar\omega_0 I_z + \hbar\omega_1 I_x \cos(\omega_{rf}t + \varphi) \quad (3.12)$$

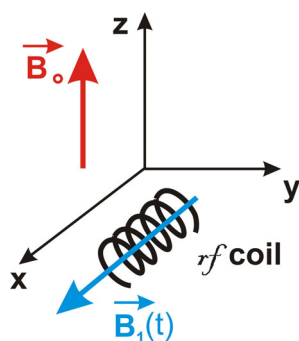


**Figure 3.2.** External magnetic fields in the laboratory frame ( $x, y, z$ ).  $B_0$  is the applied static magnetic field along the  $z$ -axis.  $B_1$  is a pulsed oscillating radio-frequency field perpendicular to  $B_0$  (in the present case it is along the  $x$ -axis).

### 3.2. Internal interactions

The total interaction energy (described by the spin Hamiltonian) of the nucleus is the sum of all the individual contributions it experiences. The external magnetic fields applied allow

one to manipulate the spin. The information about the atomic scale surroundings of a nucleus is given by the interactions between the nucleus and those surroundings. These interactions are summarized in the internal Hamiltonian.

$$\hat{H}_{\text{int}} = \hat{H}_{CS} + \hat{H}_D + \hat{H}_K + \hat{H}_J + \hat{H}_P + \hat{H}_Q \quad (3.13)$$

In diamagnetic insulating solids, spin 1/2 nuclei experience a range of interactions that include chemical shielding ( $\hat{H}_{CS}$ ), modification of the magnetic field at the nucleus due to the surrounding electrons, magnetic dipolar ( $\hat{H}_D$ ), interaction through space with nearby nuclear magnetic moments, and indirect spin-spin coupling ( $\hat{H}_J$ ), interaction of nuclear magnetic moments mediated by intermediate electron spins. In materials that contain paramagnetic centers the unpaired electrons can interact strongly with the nuclei ( $\hat{H}_P$ ) and possibly cause very large shifts and severe broadening of the NMR signal. In materials containing conduction electrons these can also interact strongly with the nuclear spin via a contact interaction ( $\hat{H}_K$ ) that produces both relaxation and a change in resonance position termed the Knight shift. Nuclei with spin  $I > 1/2$  are also affected by the electric quadrupole interaction ( $\hat{H}_Q$ ), an interaction between the nuclear electric quadrupole moment and the gradient in the electric field at the nucleus. The quadrupolar interaction can cause a significant splitting relative to the Zeeman effect.

All the interactions that affect the NMR spectra can be represented by a general expression involving tensors (spherical tensor representation)

$$\hat{H}_m = k_m I_i T_{ij}^m \cdot A_j^m \quad (3.14)$$

where  $\hat{H}_m$  is one of the component Hamiltonians in equation (3.13). For each interaction there is a constant  $k$ , a 3x3 second-rank tensor  $T$  and another vector quantity, either a field or a spin with which the spin interacts.

The internal and external interactions are summarized in Table 3.2.

**Table 3.2.** Overview of NMR interactions

$\hat{H}_m$	Interaction	$T$	$A$	Typical size (Hz)	Comments
$\hat{H}_Z$	Zeeman	Unitary	$B_0$	$10^7$ - $10^9$	interaction with main magnetic field
$\hat{H}_{rf}$	RF	Unitary	$B_1$	$10^3$ - $10^5$	interaction with <i>rf</i> field
$\hat{H}_{CS}$	Chemical Shielding	$\sigma$	$B_0$	$10^2$ - $10^5$	alteration of magnetic field by the electrons
$\hat{H}_D$	Dipolar	$D$	$I$	$10^3$ - $10^4$	through space spin-spin interaction
$\hat{H}_J$	J-coupling	$J$	$I$	$1$ - $10^3$	spin-spin interaction mediated via the bonding electrons through the contact interaction
$\hat{H}_P$	Paramagnetic	$P$	$S$	$10^2$ - $10^5$	Interaction with isolated unpaired electrons
$\hat{H}_K$	Knight Shielding	$K$	$S$	$10^2$ - $10^5$	Interaction with conduction electrons via the contact interaction
$\hat{H}_Q$	Quadrupolar	$eq$	$I$	$10^3$ - $10^7$	Interaction with the electric field gradient

All these interactions are quite similar in form, containing an anisotropic part so that in powders the lines are usually significantly broadened. The first-order perturbation shows an angular variation of the form  $\Delta((3\cos^2\beta - 1) + \eta\sin^2\beta\cos 2\alpha)$  which is similar for all interactions.

In the following, the internal interactions that are important for the system and nuclei in this work are explained in more detail.

### 3.2.1. Chemical shielding

The signal position in NMR depends on the chemical environment of the nucleus. This is termed the chemical shielding and means that the exact resonance frequency is an extremely sensitive discriminator of the chemical environment as it depends on the electron density and hence reflects the chemical bonding. The three-dimensional nature of the

electron density in a material means that the chemical shielding is represented by a second-rank tensor  $\sigma$  and the corresponding Hamiltonian is

$$\hat{H}_{CS} = \gamma_I \hbar \vec{I} \sigma \vec{B}_0 \quad (3.15)$$

The orientation dependence is present in the chemical shielding tensor which in its principal axis system (PAS) is diagonal with the principal components  $\sigma_{XX}$ ,  $\sigma_{YY}$  and  $\sigma_{ZZ}$ . Hence, the tensor representation is given in the PAS by

$$\sigma^{PAS} = \begin{pmatrix} \sigma_{XX} & 0 & 0 \\ 0 & \sigma_{YY} & 0 \\ 0 & 0 & \sigma_{ZZ} \end{pmatrix} \quad (3.16)$$

which when transformed into the laboratory frame (LF) becomes

$$\sigma = \begin{pmatrix} \sigma_{xx} & \sigma_{xy} & \sigma_{xz} \\ \sigma_{yx} & \sigma_{yy} & \sigma_{yz} \\ \sigma_{zx} & \sigma_{zy} & \sigma_{zz} \end{pmatrix} \quad (3.17)$$

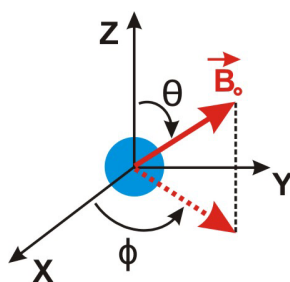


**Figure 3.3.**  $B_0$  orientation in the principal axes system (PAS) frame

The tensor components are distinguished by capital subscripts in the PAS and lower case subscripts in the laboratory frame. The two frames are related by rotation of the axes using matrices with the Euler angles defining the rotation to give:

$$\sigma^{LAB} = R(\alpha\beta\gamma) \sigma^{PAS} R^{-1}(\alpha\beta\gamma) \quad (3.18)$$

Then the field at the nucleus, including both the main field and the shielding, yields

$$\vec{B} = (1 - \sigma) \cdot \vec{B}_0 = \begin{pmatrix} 1 - \sigma_{xx} & -\sigma_{xy} & -\sigma_{xz} \\ -\sigma_{yx} & 1 - \sigma_{yy} & -\sigma_{yz} \\ -\sigma_{zx} & -\sigma_{zy} & 1 - \sigma_{zz} \end{pmatrix} \cdot \begin{pmatrix} 0 \\ 0 \\ B_0 \end{pmatrix} = \begin{pmatrix} -\sigma_{xz} B_0 \\ -\sigma_{yz} B_0 \\ (1 - \sigma_{zz}) B_0 \end{pmatrix} \quad (3.19)$$

It is only the  $zz$ -component that is of interest since after this transformation this is the component that is aligned with  $B_0$ ,  $\sigma_{xz}$  and  $\sigma_{yz}$  make only second-order contributions.

Hence the Hamiltonian representing the chemical shielding is now given by:

$$\hat{H}_{CS} = \gamma_I \hbar I_z \cdot \sigma_{zz} \cdot B_0 \quad (3.20)$$

$\sigma_{zz}$  is obtained by performing the appropriate set of rotations from the PAS to the LAB frame, and the tensor element becomes:

$$\sigma_{zz} = \sigma_{iso} + \frac{\Delta\sigma}{2} \left[ \left( 3 \cos^2 \theta - 1 \right) + \eta \left( \sin^2 \theta \cos 2\phi \right) \right] \quad (3.21)$$

where  $\sigma_{iso} = \frac{1}{3}(\sigma_{xx} + \sigma_{yy} + \sigma_{zz})$ .  $\Delta\sigma = \sigma_{zz} - \sigma_{iso}$  is denoted as the shielding anisotropy

and  $\eta = \frac{\sigma_{XX} - \sigma_{YY}}{\Delta\sigma}$  is the asymmetry parameter. The angles  $\theta$  and  $\phi$  are the polar angles

of the LAB frame in the PAS of the tensor (Figure 3.3).

Chemical shielding ( $\sigma$ ) can be expressed by the difference of the resonance frequency between the sample ( $\nu_{sample}$ ) and a reference Larmor frequency ( $\nu_{Larmor}$ ) for that nucleus. It is then normalized by ( $\nu_{Larmor}$ ) and quoted in parts per million (ppm)

$$\sigma_{sample} = \frac{\nu_{Larmor} - \nu_{sample}}{\nu_{Larmor}} \times 10^6 \quad (3.22)$$

Hence, measurements at different magnetic fields can be directly compared. Instead of the chemical shielding, the chemical shift ( $\delta$ ) is normally given which is calculated by

$$\delta = \frac{\sigma_{ref} - \sigma_{sample}}{1 - \sigma_{ref}} \quad (3.23)$$

### 3.2.2. The dipolar interaction

The dipolar interaction arises from the coupling between two magnetic dipoles. Classically the energy of two interacting dipoles  $\mu_1$  and  $\mu_2$ , separated by a distance  $r$ , is given by

$$E_D = \frac{\mu_o}{4\pi} \left[ \frac{\vec{\mu}_1 \cdot \vec{\mu}_2}{r^3} - \frac{3(\vec{\mu}_1 \cdot \vec{r})(\vec{\mu}_2 \cdot \vec{r})}{r^5} \right] \quad (3.24)$$

and the Hamiltonian:

$$\hat{H}_D = \frac{\mu_o}{4\pi} \frac{\gamma_1 \gamma_2 \hbar^2}{r^3} \left[ \vec{I}_1 \cdot \vec{I}_2 - \frac{3(\vec{I}_1 \cdot \vec{r})(\vec{I}_2 \cdot \vec{r})}{r^2} \right] \quad (3.25)$$

where  $\mu_o$  is permeability and  $\gamma$  is gyromagnetic ratio of the involved nuclei.

This can be usually rewritten in terms of polar coordinates as:  $x = r \sin \theta \cos \phi$ ,  $y = r \sin \theta \sin \phi$  and  $z = r \cos \theta$ .

The secular dipolar Hamiltonian for a set of like-spin  $I_i$  and  $I_j$  is then as following:

$$\hat{H}_D^{II} = \frac{\mu_o}{4\pi} \frac{1}{2} \frac{\gamma_I^2 \hbar^2}{r_{ij}^3} \left[ 3I_{iz}I_{jz} - I_i I_j \right] \left( 3 \cos^2 \theta_{ij} - 1 \right) \quad (3.26)$$

whereas the secular heteronuclear dipolar Hamiltonian for spin  $I$  and spin  $S$  is given by:

$$\hat{H}_D^{IS} = \frac{\mu_o}{4\pi} \frac{\gamma_I \gamma_S \hbar^2}{r_{IS}^3} I_Z S_Z \left( 3 \cos^2 \theta_{IS} - 1 \right) \quad (3.27)$$

Both the homonuclear and heteronuclear dipolar coupling depend on the orientation of the inter-nuclear vector and the inverse cube of the distance.

### 3.3. Single-pulse excitation



**Figure 3.4.** Single pulse NMR experiment

The most basic experiment in FT-NMR consists of a single  $90^\circ$  pulse. After applying a  $90^\circ$   $x$   $rf$  pulse the net magnetization is flipped from the  $z$  axis to the  $y$ -axis and precesses in the  $xy$ -plane with its resonance frequency. This induces a weak oscillating voltage in the  $rf$  -coil, which is amplified and later converted into a digital signal that can be handled by a computer. This oscillating electric current induced by the precessing nuclear transverse magnetization is called NMR signal or free-induction decay (FID).

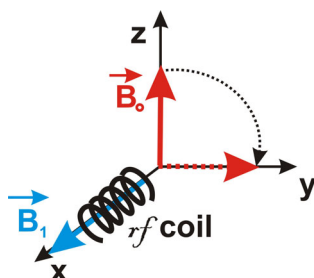


**Figure 3.5.** The vector model showing the effect of  $90^\circ$   $x$  pulse

### 3.4. Methods for improving resolution

The anisotropic part of the interactions cause broadening which can often be very significant. In liquids the interactions responsible for line broadening are averaged by the continuous, random tumbling and translational motions of the molecules. This isotropic averaging of the interactions produces high resolution spectra. However in solids it is often necessary to improve resolution by deliberately averaging the anisotropic parts of the interactions, thereby obtaining line narrowing. The Hamiltonians representing these interactions have all been seen to contain a spatially-dependent part and a spin-dependent

part. To average these interactions, either (or both) of these parts of the Hamiltonian must be manipulated which usually means making them time-dependent.

By far the most common approach is to make the spatial part time-dependent, for example by applying magic angle spinning (MAS) [109,110,148], variable angle spinning (VAS), double angle rotation (DOR) and dynamic angle spinning (DAS). The spatial part can also be varied by diluting the spins which reduces the dipolar coupling since the magnitude of the dipolar coupling is proportional to the inverse cube of the distance between the spins. Techniques for averaging the spin part include decoupling, both for heteronuclear and homonuclear dipolar coupling cases. The averaging techniques can be used in combination with each other, leading to even higher resolution enhancement.

In the following the techniques that have been used in this work are explained in detail.

### 3.4.1. Magic angle spinning (MAS)

Magic angle sample spinning, is probably the most widely used technique to enhance spectral resolution in solid-state NMR spectroscopy [109,110,148]. The solid sample is loaded into a container called a rotor which is inclined at a fixed angle to the magnetic field and rapidly spun about its symmetry axis.

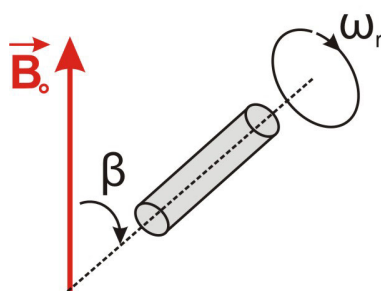


**Figure 3.6.** Rotation of the sample around an axis at an angle of  $\beta = 54.7^\circ$  to the external magnetic field  $B_0$ .

Under fast spinning the averaged chemical shift anisotropy and dipolar coupling can be described as:

$$\omega = \omega_{iso} + \omega_{aniso}(\theta, \varphi) \frac{1}{2} (3 \cos^2 \beta - 1) \quad (3.28)$$

where  $\beta$  specifies the orientation of the rotation axis relative to  $B_0$ . The anisotropic part of the frequency  $\omega_{aniso}(\theta, \varphi)$  vanishes when  $\beta$  equals the magic angle,  $54.7^\circ$  or more accurately  $\arccos(1/3)^{1/2}$ , and only the isotropic frequency is retained.

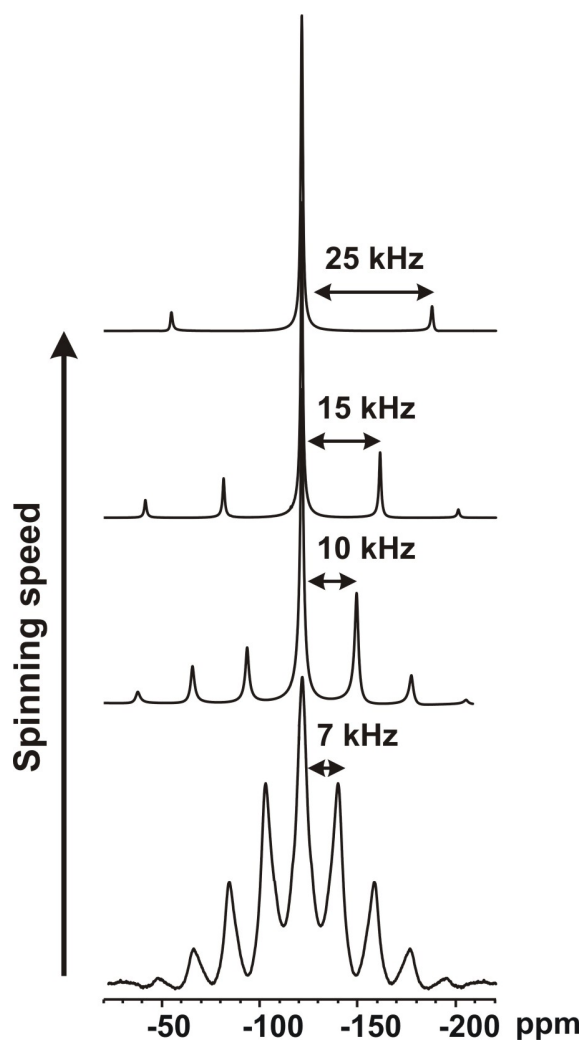


**Figure 3.7.** The influence of the spinning rate on the  $^{19}\text{F}$  NMR spectra of Teflon

When the spinning speed is comparable to the strength of the anisotropic interaction, there will be a set of frequencies separated at integer multiples of the spinning frequency,

spinning sidebands (SSB). They can be used to extract chemical shift anisotropy information.

The orientation and time dependent frequency is described by:

$$\begin{aligned} \omega(t) = & C_1 \cos(\gamma + \omega_r t) + S_1 \sin(\gamma + \omega_r t) \\ & + C_2 \cos(2\gamma + 2\omega_r t) + S_2 \sin(2\gamma + 2\omega_r t) \end{aligned} \quad (3.29)$$

where  $\omega_r$  is spinning speed in radian and the angles  $\alpha, \beta, \gamma$  specify the orientation of the PAS in the rotor frame. The coefficients  $C_n$  and  $S_n$  depend on the chemical shift parameters  $\delta$  and  $\eta$ , and the angles  $\alpha$  and  $\beta$ .

### 3.4.2. Cross Polarization (CP)

Even with the line narrowing techniques such as MAS, NMR experiments on solids with dilute spin 1/2 nuclei are still relatively unattractive for two reasons. One is the lack of sensitivity due to their low net polarization and the other is the relatively long spin-lattice relaxation time. In solids where both abundant (I) and dilute (S) nuclei coexist, polarization transfer techniques can usually be used to overcome both problems [108]. The most common technique is to create and spin-lock transverse I-magnetization. The experiment is best understood using ideas from spin thermodynamics. The magnetization is given by Curie's Law:

$$M_o = \frac{N\gamma^2 B_o \hbar^2 I(I+1)}{3kT} \quad (3.30)$$

where N is the total number of spins,  $M_o$  is the equilibrium magnetization and the temperature in this equation is the thermodynamic lattice temperature.

The transverse I-magnetization is created and then spin-locked. In the spin-locking frame the effective field is only  $B_1$ . In the spin-locking frame immediately after the  $90^\circ$  pulse, the I-magnetization is still  $M_1$  but the energy levels are now much closer ( $\gamma\hbar B_1$  as opposed

to  $\gamma\hbar B_0$ ). With the new field  $B_1$  the system can now be assigned with an effective spin temperature  $T_{P1}$  defined by

$$M_1 = \frac{N_1 \gamma_1^2 \hbar^2 I(I+1) B_0}{T_L} = \frac{N_1 \gamma_1^2 \hbar^2 I(I+1) B_{1I}}{T_{P1}} \quad (3.31)$$

As  $B_{1I} \ll B_0$  and the degree of order amongst the spins remains the same (i.e.  $M_1$  is constant), it follows that

$$T_{P1} = \frac{B_{1I}}{B_0} T_L \quad (3.32)$$

Hence the I-spins are effectively very cold. The S-spins, in contrast, start off with no transverse magnetization so, in terms of thermodynamics, they are very hot. There is a thermodynamic driving force for the transfer of magnetization. However, the spin systems have to be allowed to communicate efficiently and this is achieved by applying a second  $B_1$  field, this time to the S-spins. If the two spins to be brought in contact are spin 1/2, then the condition the two fields must meet the Hartmann-Hahn condition [149]:

$$\gamma_I B_{1I} = \gamma_S B_{1S} \quad (3.33)$$

When this condition is satisfied, the dipole flip-flop terms are energy conserving so that order can be transferred between the I and S spins. Thermodynamics means that transfer of order occurs, tending to give the two systems a common spin temperature ( $T_{P2}$ ).

$$T_{P2} = T_{P1} \left[ \frac{N_S}{N_I} - 1 \right] \quad (3.34)$$

The spin temperature for the I-spin system changes very little, so that I-magnetization essentially remains unchanged as a result of the contact, and S-magnetization created is

$$M_S = \frac{N_S \gamma_S^2 \hbar^2 S(S+1)}{3kT_{P2}} = \frac{\gamma_I}{\gamma_S} \frac{1}{1+A} \frac{N_S \gamma_S^2 \hbar^2 S(S+1) B_0}{3kT_L} \quad (3.35)$$

$$A = \frac{N_S S(S+1)}{N_I I(I+1)} \quad (3.36)$$

Hence in a single contact experiment the gain in signal intensity is approximately  $\frac{\gamma_I}{\gamma_S}$  in

comparison to a single  $90^\circ$  pulse on the S-spins.

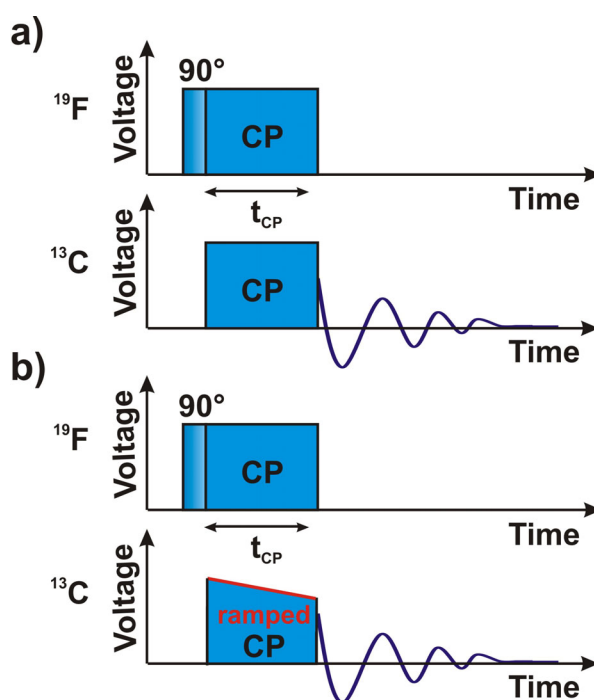


**Figure 3.8.** The pulse sequence of normal (a) and ramped amplitude (b) cross-polarization experiment.

Under MAS condition, this matching condition changes to

$$\gamma_I B_1(I) = \gamma_S B_1(S) \pm n\omega_r \quad (3.37)$$

( $\omega_r$  being the spinning frequency) with maximum signal for  $n = \pm 1$ ).

At slow MAS rates a broad matching condition is usually obtained around the central Hartmann-Hahn condition and any mismatch is relatively unimportant. As the spinning

speed increases, the matching profile breaks up into a series of narrowing matching bands separated by  $\omega_r$  (the spinning frequency). The CP rate at the central matching condition is slower than at some of the sidebands.

Ramping the amplitude across one of the matching sidebands with the ramp centered on one of the matching sidebands has been found to improve greatly the CP efficiency and broaden the matching condition [150].

### 3.4.3. Decoupling

In some cases the broadening arising from interactions between the dipole moments of two different nuclei (heteronuclear broadening) is too large to be removed completely by MAS. In a NMR experiment one can usually only observe one kind of nucleus at a time, such as  $^1\text{H}$ ,  $^{13}\text{C}$  or  $^{19}\text{F}$ . Historically,  $^1\text{H}$  NMR was the first to be exploited widely, and is still the most recorded nucleus. As a result, all nuclei which are not protons are grouped together and called heteronuclei.

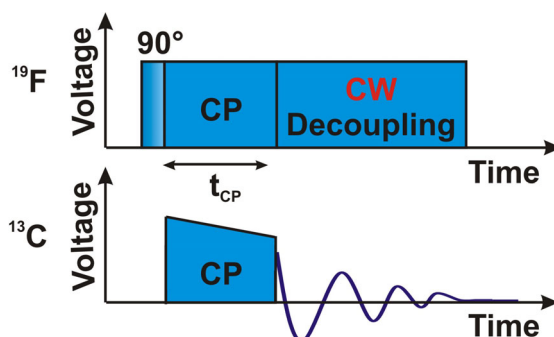


**Figure 3.9.** The pulse sequence of cross polarization experiment with continuous wave (CW) decoupling.

When dealing with heteronuclei, S, with low natural abundance, homonuclear coupling can safely be neglected. However, even at fast MAS up to 30 kHz the heteronuclear dipolar coupling between the S nuclei and high abundant nuclei, I (usually  $^1\text{H}$  or in our case  $^{19}\text{F}$ ), still causes significant line broadening. To overcome this problem various decoupling schemes have been devised and improved [151-153]. The simplest method for decoupling is continuous wave (CW) decoupling, where a continuous *rf* pulse of fixed phase is applied

for the duration of the acquisition of the free induction decay (FID). In order to obtain sufficient decoupling efficiency, high *rf* power is needed, which is technically demanding and sometimes not desirable. Therefore improved high-power multiple-pulse decoupling schemes are considered, and proved to be efficient methods for solids under fast MAS. Two-pulse phase-modulated (TPPM) [154-156] and X inverse-X (XiX) [157] are the most widely adopted decoupling sequence which provide significant improvement in both linewidth and intensity under a wide range of experimental conditions.

**XY-16 decoupling for  $^{13}\text{C}$  CP/MAS NMR in perfluorinated polymers:** The combination of significant  $^{13}\text{C}$ - $^{19}\text{F}$  and  $^{19}\text{F}$ - $^{19}\text{F}$  dipolar couplings [158] with large ( $>130$  ppm)  $^{19}\text{F}$  chemical shift anisotropies [159] cause a large line broadening for the  $^{13}\text{C}$  solid-state NMR spectra in perfluorinated polymers such as Teflon and Nafion. The  $^{13}\text{C}$  CP/MAS spectrum of Teflon at a Larmor frequency of 100 MHz and spinning speed of 5 kHz shows relatively broad lines resulting from insufficient  $^{19}\text{F}$  decoupling. The line broadening problem can be partially overcome by using high speed magic-angle spinning. At spinning rates higher than 25 kHz, the central lines of  $^{19}\text{F}$  NMR spectra are narrowed to less than 1 ppm [128,160,161]. This indicates that MAS is sufficient to average  $^{19}\text{F}$ - $^{19}\text{F}$  dipolar couplings to nearly zero. As a result,  $^{13}\text{C}$ - $^{19}\text{F}$  dipolar couplings are also greatly reduced [162]. Nevertheless, the spectrum is still undesirably broadened. The large spread of  $^{19}\text{F}$  frequencies makes it impossible to irradiate the  $^{19}\text{F}$  decoupling power on or near resonance for all  $^{19}\text{F}$  nuclei in an unoriented sample and causes off-resonance line-broadening in the  $^{13}\text{C}$  MAS NMR spectra of fluoropolymers.

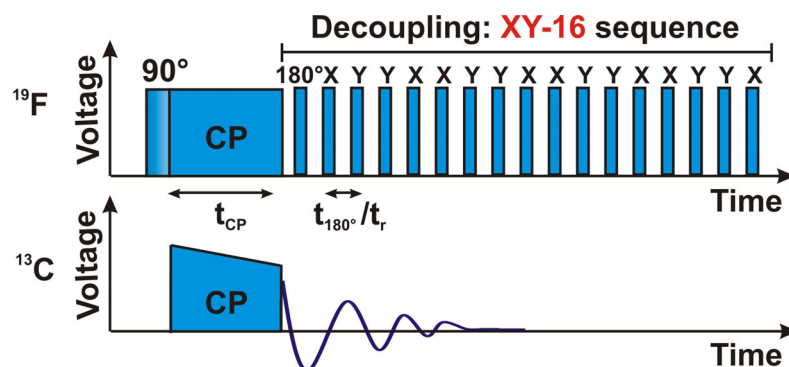


**Figure 3.10.**  $^{13}\text{C}\{^{19}\text{F}\}$  CP/MAS NMR experiment with XY-16 decoupling

The residual line broadening in  $^{13}\text{C}$  NMR can be removed effectively by using rotation synchronized  $^{19}\text{F}$   $180^\circ$  pulses [162]. The decoupling pulse sequence consists of one  $180^\circ$  pulse at the end of each rotor period. The train of  $180^\circ$  pulses, using the xy-16 phase sequence [163], keeps refocusing the  $^{19}\text{F}$ - $^{13}\text{C}$  J-couplings, while not recoupling the dipolar interactions. The approach of using one  $180^\circ$  pulse per cycle is reminiscent of pulsed heteronuclear decoupling during multiple-pulse homonuclear decoupling [162].

The pulsed decoupling at high speed MAS (i.e. 28 kHz spinning speed) works very well, yielding a CP/MAS  $^{13}\text{C}$  peak of PTFE, with only 18 Hz (0.18 ppm) linewidth. Compared to the standard CP/MAS spectrum, the signal has been narrowed by more than a factor of 100. The decoupling sequence has a small duty cycle of  $(t_{180^\circ} / t_r)$ , where  $t_{180^\circ}$  is the  $180^\circ$  pulse length and  $t_r$  is the rotation period.

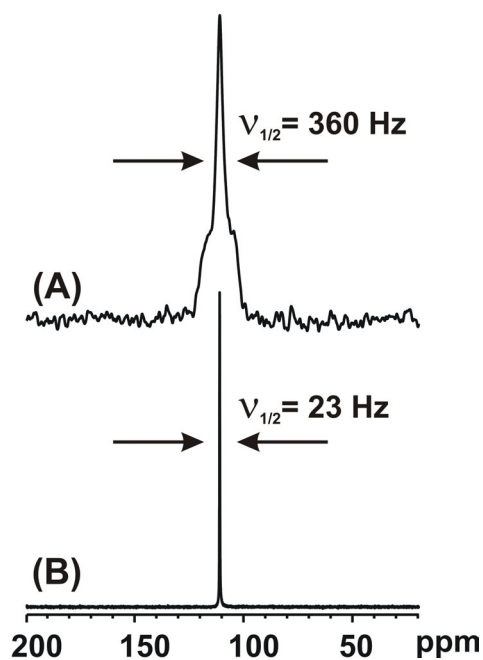


**Figure 3.11.** The  $^{13}\text{C}\{^{19}\text{F}\}$  CP/MAS NMR of Teflon with CW (A) and XY-16 (B) decoupling sequence at 25 kHz spinning speed.

### 3.5. Nuclear spin relaxation

One of the most important and useful features of NMR is its ability to probe molecular motions, over a wide range of time scales, ranging from picoseconds ( $10^{-12}$  s) to tens of

seconds. Any motion in this range (intermolecular or intramolecular) which changes the nuclear spin Hamiltonian is detectable by NMR. The effect of motion on the nuclear spin dynamics depend on their time scale and can be detected by NMR relaxation experiments (Figure 2.12).

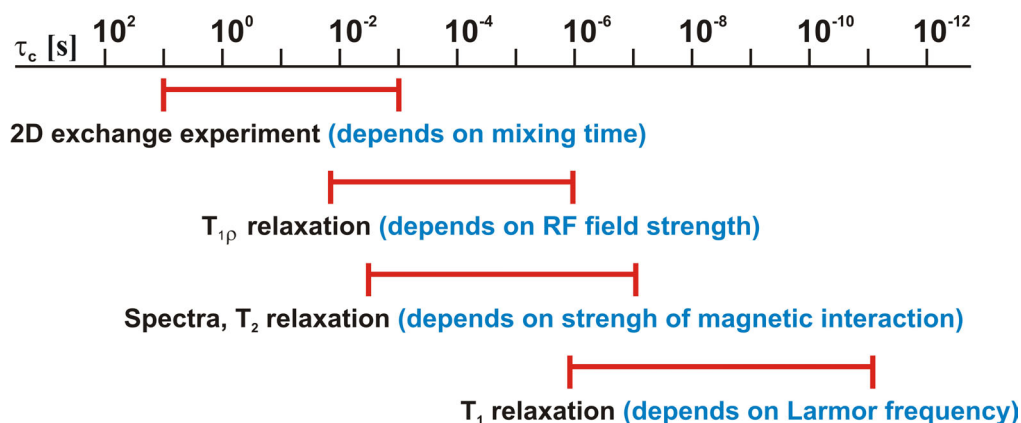


**Figure 3.12.** NMR time scale.

If the sample is allowed to be undisturbed for a long time in the magnetic field, it reaches a state of thermal equilibrium. At equilibrium, nuclei are distributed among the energy levels according to a Boltzmann distribution. *rf* pulses disturb the equilibrium of the spin system. The population after a pulse usually deviates from their thermal equilibrium values. Spin relaxation is the process by which equilibrium is regained, through interaction of the spin system with the thermal molecular environment.

Relaxation processes may be divided into two types. Spin-lattice relaxation ( $T_1$ ) is concerned with the movement of spin populations back to their Boltzmann distribution values. In this process, the population of the spin states is changed and energy is exchanged with the surrounding. The spin-spin relaxation ( $T_2$ ) is concerned with the decay of coherences (i.e. phase relationships).

Apart from  $T_1$  and  $T_2$ , also  $T_{1\rho}$ , spin-lattice relaxation in rotation frame can be studied. This quantity describes the decay time constant for transverse magnetization in the presence of an *rf* field.

Bloembergen, Purcell and Pound have shown that the dependence of  $T_1$  on the molecular correlation time  $\tau_c$  at different resonance frequencies can be given by (assuming isotropic motion) [125,164]

$$\frac{1}{T_1} = K \left[ \frac{\tau_c}{1 + \omega_o^2 \tau_c^2} + \frac{4\tau_c}{1 + 4\omega_o^2 \tau_c^2} \right] \quad (3.38)$$

where  $K$  is a function related to the correlation time for the molecular motions,  $\tau_c$ . If  $K$  decays to zero in a short time, the sample is characterized by a short correlation time and the molecular motions are very rapid. Quantitatively, the correlation time indicates how long it takes before the random field changes sign. In practice, the correlation time depends on the physical parameters of the system, such as the temperature. If  $E_a$  is the activation energy of molecular motion, the correlation time can be described with the Arrhenius equation:

$$\tau_c = \tau_o \exp(E_a/RT) \quad (3.39)$$

$\tau_o$  is the correlation time constant.

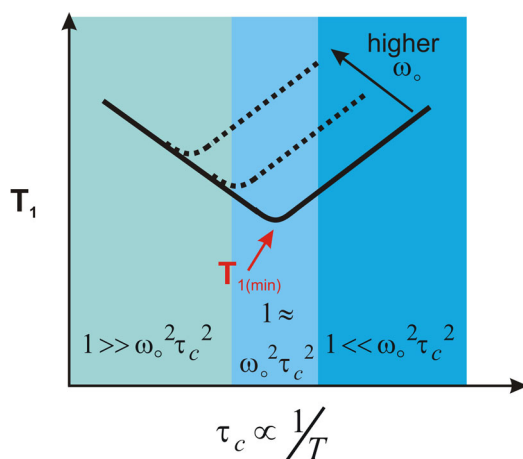


**Figure 3.13.** Plot of spin-lattice relaxation time  $T_1$  as a function of correlation time  $\tau_c$ .

As shown in Figure 3.13, in the higher temperature region, to the left of the  $T_1$  minimum,  $T_1$  is found to be frequency independent, and it decreases with decreasing temperature. This

behavior is typical of any molecule which is characterized by small  $\tau_c$  values where  $1 \gg \omega_o^2 \tau_c^2$  (small molecules in non-viscous liquids).

If  $1 \approx \omega_o^2 \tau_c^2$ ,  $T_1$  goes through a minimum and the value of the  $T_1$  at the minimum is proportional to  $\omega_o$ . In the low temperature region, to the right of the  $T_1$  minimum,  $T_1$  is frequency dependent and its value increases with decreasing temperature. This situation is found whenever  $1 \ll \omega_o^2 \tau_c^2$  (large molecules and viscous liquids).

The dependence of  $T_{1\rho}$  on the molecular correlation time  $\tau_c$  is [164]:

$$\frac{1}{T_{1\rho}} = K \left[ \frac{3}{2} \frac{\tau_c}{1 + \omega_1^2 \tau_c^2} + \frac{5}{2} \frac{\tau_c}{1 + \omega_o^2 \tau_c^2} + \frac{\tau_c}{1 + \omega_o^2 \tau_c^2} \right] \quad (3.40)$$

$T_{1\rho}$ , goes through a minimum when  $1 \approx \omega_1^2 \tau_c^2$ .

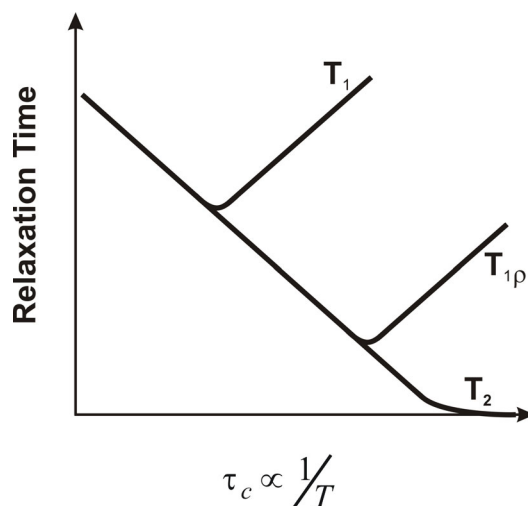


**Figure 3.14.** The dependence of  $T_1$ ,  $T_2$  and  $T_{1\rho}$  on the correlation time  $\tau_c$ .

### 3.5.1. Inversion recovery: measurement of $T_1$

The spin-lattice relaxation time in the laboratory frame,  $T_1$ , can be measured by using the inversion recovery sequence as shown in Figure 3.15.

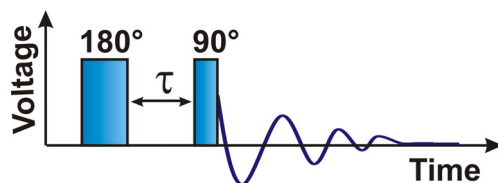


**Figure 3.15.** Inversion recovery sequence for measuring  $T_1$

The inversion recovery sequence consists of two  $rf$  pulses separated by an interval  $\tau$ . The pulse sequence is repeated with different values of the interval  $\tau$ . For each value of  $\tau$  the pulse sequence and data acquisition is normally repeated many times. Also each repetition of the pulse sequence is separated by a long interval  $\tau_{wait}$ , during which the spins return to a reproducible thermal equilibrium state. The waiting interval plus the signal acquisition period  $\tau_{acq}$  must be several times the relaxation time constant  $T_1$ .

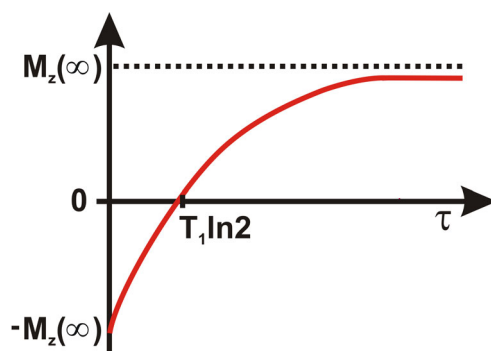


**Figure 3.16.** Peak amplitude as a function of  $\tau$  in inversion recovery experiment.

The observed signal amplitude is a function of the interval between the pulses:

$$M_Z(\tau) = M_o [1 - 2 \exp(-\tau/T_1)] \quad (3.41)$$

where  $M_o$  is the equilibrium magnetization.

### 3.5.2. Spin locking: measurement of $T_{1\rho}$

The spin locking method employs a resonant  $rf$  field to suppress the free evolution of transverse magnetization, locking it to a particular direction in the rotation frame. A typical spin locking pulse sequence is as follows:

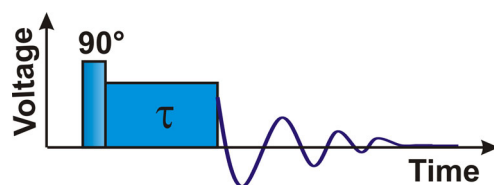


**Figure 3.17.** Pulse sequence for a spin locking experiment.

The initial  $90^\circ$   $y$  pulse converts the initial longitudinal magnetization into transverse magnetization along the rotation frame  $x$ -axis. The phase of the  $rf$  field is then suddenly changed to  $\varphi = 0$ , so that the rotation frame  $rf$  field is along the  $x$ -axis. Then the transverse magnetization is unable to precess away from the  $x$ -axis and it is said to be spin locked. After a time  $\tau$  the locking field is turned off, releasing the transverse magnetization and allowing it to generate an NMR signal.

The spin locked magnetization decays exponentially to zero. The decay process is followed by conducting a series of experiments with several values of the locking time  $\tau$ . The time constant of the exponential decay is denoted by  $T_{1\rho}$ .

$$M_z(\tau) = M_0 \exp(-\tau/T_{1\rho}) \quad (3.42)$$

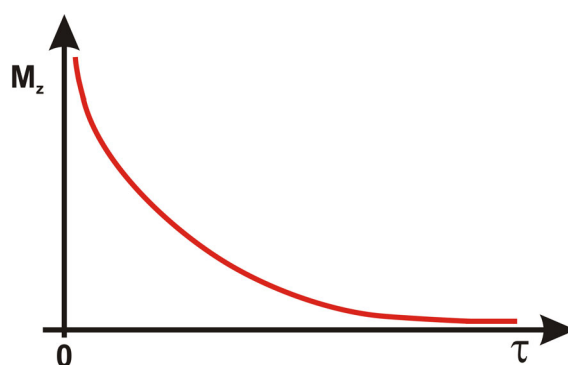


**Figure 3.18.** Peak amplitude as a function of  $\tau$  in spin lock experiment.



## 4. Fuel Cell Degradation Tests

### 4.1. Introduction

In this part of the work, the chemical changes on polymer electrolyte membranes, Nafion and Hyflon Ion, are detected before and after in-situ fuel cell tests by  $^{13}\text{C}$  CP/MAS and  $^{19}\text{F}$  solid-state NMR spectroscopy. The effects of membrane thickness and polymer architecture on degradation are examined and the most reactive molecular segments are determined.

### 4.2. Experimental

#### 4.2.1. Materials

Two types of perfluorosulfonic acid membranes, Nafion of different thickness (Nafion 112, 115 and Nafion 117) and Hyflon Ion type E87, were used. The relevant material parameters are summarized in Table 4.1.

#### 4.2.2. Membrane pre-conditioning

Pieces of membranes were washed in  $\text{H}_2\text{O}_2$  (3 v/v%) at 80 °C for 1 hour, and were rinsed in deionized water for another hour at  $T = 80$  °C. After this procedure, the membranes were completely transparent. For exchanging all ions by protons, the membrane was exposed to a solution of  $\text{HNO}_3$  (5 w/w%) at 80 °C for 4 hours. The membranes were then rinsed in

deionized water at  $T = 80\text{ }^{\circ}\text{C}$ . The water was renewed after each hour for at least 4 times. In the last step, the membranes were kept in deionized water at room temperature overnight.

**Table 4.1.** Properties of the perfluorinated membranes investigated for the in-situ degradation test

Membrane	Supplier	Thickness (inch)	Ion-exchange capacity (meqg <sup>-1</sup> )
<b>Nafion 112</b>	Hydro2Power SRL	0.002	0.9
<b>Nafion 115</b>	Hydro2Power SRL	0.005	0.9
<b>Nafion 117</b>	Hydro2Power SRL	0.007	0.9
<b>Hyflon Ion E87</b>	Solvay Solexis S.p.A.	0.00078	1.15

### 4.2.3. Fuel cell tests

Details of the test protocols are reported by Marrony et. al. [165]. E-TEK LT250EW electrodes (0.5 mg Pt/cm<sup>2</sup> and 0.7 mg Nafion/cm<sup>2</sup>) were used for the membrane-electrodes assembly (MEA) during the fuel cell tests. A mechanical pressure of 3 Nm is applied at ambient temperature using 5 cm<sup>2</sup> of active surface area. The gas pressures were kept at  $p = 1.5$  bar with flows corresponding to a stoichiometry of 1.5/2 for H<sub>2</sub> and O<sub>2</sub>.

At the beginning of each test the cells were activated by inlet gases of 100% relative humidity. The cell was then heated to 70 °C with a temperature ramp of 5 °C per hour, and a potential of  $E = 0.65$  to 0.7 V was applied to the cell by adjusting the current. A by-pass system also allowed for dry-gases mode. Some cycling electrical loading steps were then performed, simulating the hydration and dehydration behavior of the membrane likely to be encountered during long term operation. The experimental procedure provided one open circuit voltage (OCV) event per hour which lasted 30 s, after which the system returned to the initial value for the current density.

In the same way, long time tests at operating temperatures of 80-90 °C were performed by adjusting the current in order to maintain a potential of 0.65-0.7 V. The end of the test was

reached after 150 loading cycles or after mechanical rupture of the membrane, as indicated by a sudden potential drop.

Following the fuel cell tests, the membranes were dried in a vacuum oven at 110 °C for 12 hours before carefully removing the electrodes and packing into the NMR rotors.

#### 4.2.4. NMR Spectroscopy

Solid-state NMR spectra were acquired on a Varian InfinityPlus 400 MHz spectrometer (Varian, Palo Alto/CA) operating at a static magnetic field of 9.4 T. A 4 mm four-channel HFX MAS probe with a Vespel spinning module, and zirconia rotors with Vespel drive tips, caps and plug-ins were used in order to avoid fluorine background. The spectra were recorded at 379.09 MHz for  $^{19}\text{F}$  nuclei and at 100.53 MHz for  $^{13}\text{C}$  nuclei at a spinning rate of 15 kHz.  $^{19}\text{F}$  MAS NMR spectra were recorded with a  $90^\circ$  pulse length of 2.8  $\mu\text{s}$ , a recycle delay of 2 s and a dwell time of 5  $\mu\text{s}$ . 256 transients were recorded.

$^{13}\text{C}\{^{19}\text{F}\}$  CP/MAS NMR spectra were taken by means of the RAMP-CP sequence and xy-16 pulse decoupling, with an excitation pulse of 2.8  $\mu\text{s}$ , contact time of 1.6 ms and a recycle delay of 2 s. 1024 transients were recorded for each sample.

Each transient was acquired for 10.24 ms with a spectral width of 200 kHz. The spectra were processed with the Spinsight software (Varian), and the FID was Fourier transformed without any additional line broadening. Teflon was utilized for establishing the Hartmann–Hahn match. The  $^{19}\text{F}$  NMR signal of Teflon at -121 ppm (relative to  $\text{CFCl}_3$  with  $\delta = 0$  ppm) and the  $^{13}\text{C}$  NMR signal of adamantane at 38.56 ppm (relative to TMS with  $\delta = 0$  ppm) were used as secondary external references. All experiments were performed at 80 °C which provided a better spectral resolution.

### 4.3. Results

$^{19}\text{F}$  and  $^{13}\text{C}\{^{19}\text{F}\}$  CP/MAS spectra for Nafion 117 and Hyflon Ion prior to the in-situ test are shown in Figure 4.1. The  $^{13}\text{C}$  and  $^{19}\text{F}$  resonances of Nafion were assigned on the basis of a former investigation by Chen et al. [129], and are listed in Table 4.2.

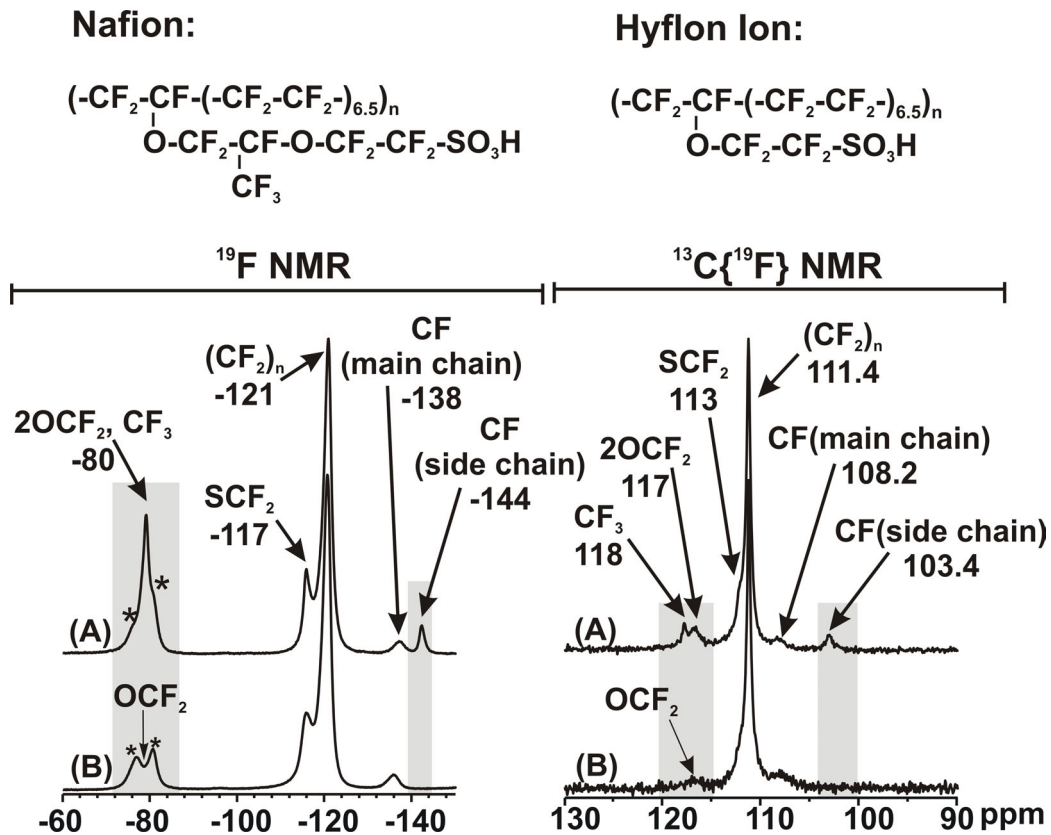


**Figure 4.1.** <sup>19</sup>F NMR and <sup>13</sup>C{<sup>19</sup>F} CP/MAS NMR spectra of Nafion (A) and Hyflon Ion (B). Asterisks indicate spinning sidebands.

**Table 4.2.** Chemical shift values (in ppm) and assignment of the <sup>13</sup>C and <sup>19</sup>F resonances in Nafion and Hyflon Ion membranes

		CF (side chain)	CF (main chain)	(CF <sub>2</sub> ) <sub>n</sub>	SCF <sub>2</sub>	OCF <sub>2</sub>	CF <sub>3</sub>
<sup>19</sup> F	Nafion	-144	-138	-121	-117	-80.1 79.9	-80
	Hyflon Ion	—	-138	-121	-117	-80	—
<sup>13</sup> C	Nafion	103.4	108.2	111.4	113	116.7 117	118
	Hyflon Ion	—	108.2	111.4	113	117	—

The NMR spectra were measured at an elevated temperature of 80 °C, which – as demonstrated by the spectra given in Figure 4.1 – provided a satisfactory resolution. It

should be mentioned that the  $^{19}\text{F}$  NMR spectrum of a completely dry membrane, recorded at room temperature, is much less resolved. For instance, the signal associated with the  $\text{SCF}_2$  segment only appears as a low-field shoulder next to the dominant  $\text{CF}_2$  signal. In principle, a better resolution could also be achieved by higher sample spinning rates which unfortunately were not available in the present study. However, it has been shown that even a spinning rate of 30 kHz was not sufficient to resolve these signals [129].

The backbones of the present fluoropolymers are identical and consist of  $\text{CF}_2$  and  $\text{CF}$  groups. The  $\text{CF}_2$  groups give rise to resonances at -121 and 111.4 ppm in the  $^{19}\text{F}$  and  $^{13}\text{C}$  NMR spectra, respectively. Likewise, the  $^{19}\text{F}$  resonance at -138 ppm and the  $^{13}\text{C}$  signal at 108.2 ppm are signatures of the backbone  $\text{CF}$  groups.

The common  $-\text{O}-\text{CF}_2-\text{CF}_2-\text{SO}_3\text{H}$  unit is clearly identified in the  $^{13}\text{C}$  and  $^{19}\text{F}$  NMR spectra of the Nafion and Hyflon Ion membranes. The  $^{19}\text{F}$  resonance at -117 ppm and the shoulder at 113 ppm in the  $^{13}\text{C}$  NMR spectrum reflect the  $\text{SCF}_2$  groups, while the  $\text{OCF}_2$  group of this common structural unit gives rise to a signal at -80 ppm in the  $^{19}\text{F}$  NMR spectra. For Nafion the  $\text{OCF}_2$  group appears as a broad peak which is dominated by the  $\text{CF}_3$  resonance at -80 ppm and the spinning sidebands from the  $\text{CF}_2$  and  $\text{SCF}_2$  signals. In the spectrum of Hyflon Ion the spinning sidebands are clearly separated while the signals from the  $\text{CF}_3$  group are missing. In the  $^{13}\text{C}$  NMR spectrum the  $\text{OCF}_2$  group appears as a broad resonance at 117 ppm.

The Nafion and Hyflon Ion membranes differ in the lengths of the side chains, and the side chain of Hyflon Ion does not contain the  $-\text{O}-\text{CF}_2-\text{CF}(\text{CF}_3)-$  segment next to the polymer backbone (see Figure 4.1). These structural differences are directly visible in the  $^{19}\text{F}$  and  $^{13}\text{C}$  NMR spectra. For Nafion additional  $^{19}\text{F}$  and  $^{13}\text{C}$  resonances at -144 and 103.4 ppm, respectively, stemming from side chain  $\text{CF}_2$  units appear. The  $\text{CF}_3$  group causes a sharp  $^{13}\text{C}$  signal at 118 ppm, while in the  $^{19}\text{F}$  NMR spectrum, the  $^{19}\text{F}$  resonance of this structural unit coincides with the  $\text{OCF}_2$  group and signals from spinning sidebands, as mentioned above.

Typical  $^{19}\text{F}$  and  $^{13}\text{C}$  NMR spectra for Nafion and Hyflon Ion samples before and after degradation are shown in Figures 4.2 and 4.3. The spectra are normalized to the dominant peak of the backbone  $\text{CF}_2$  groups. It is found that after the fuel cell tests the intensities of

the side chain signals (arising from  $\text{SCF}_2$ ,  $\text{CF}_3$ ,  $\text{OCF}_2$  and  $\text{CF}$  groups) have decreased in all polymer samples. In general, the changes after in-situ tests are better traceable in the  $^{19}\text{F}$  than in the  $^{13}\text{C}$  NMR spectra which is related to the higher sensitivity and the better resolution of the former ones.

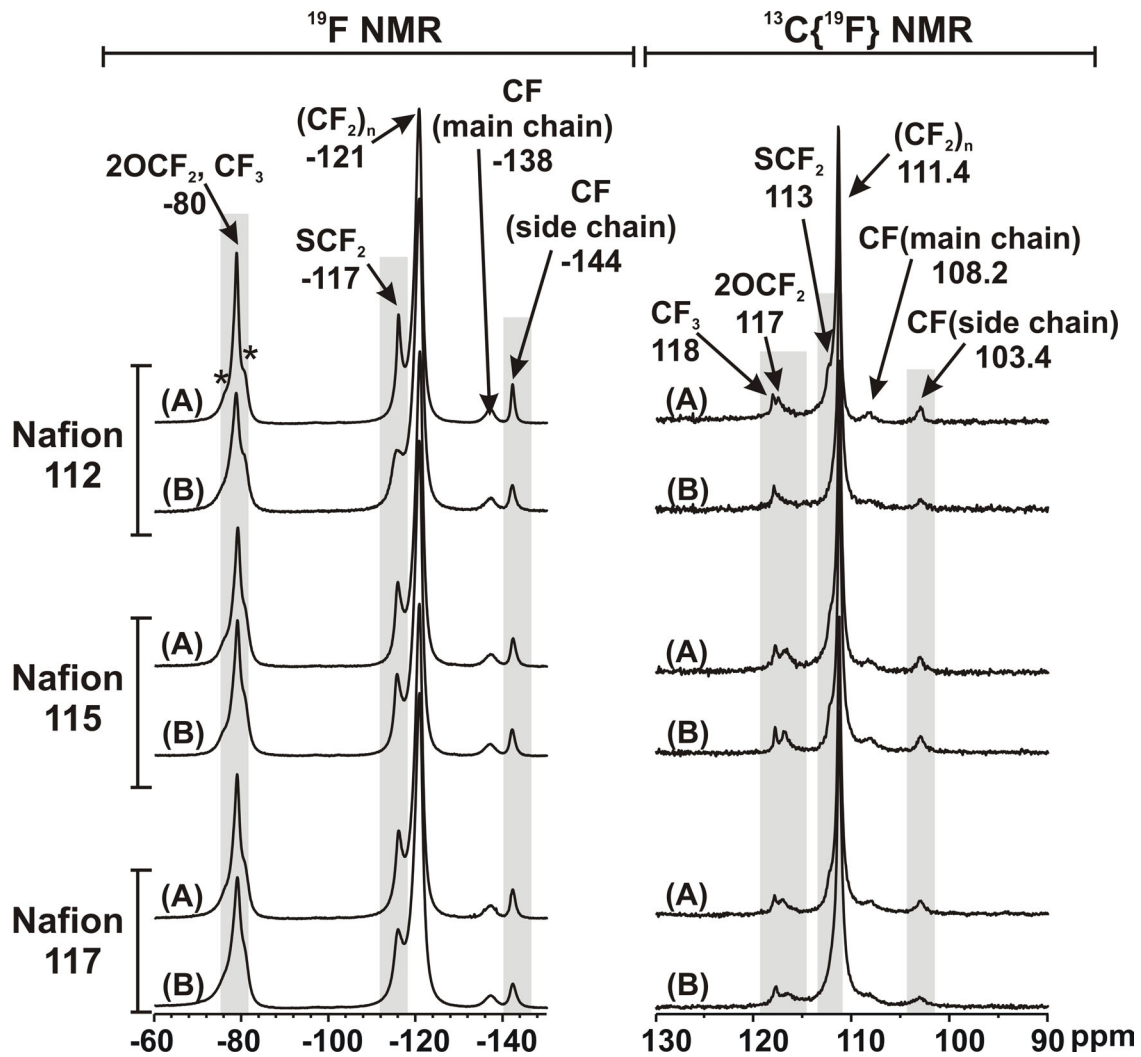


**Figure 4.2.**  $^{19}\text{F}$  NMR and  $^{13}\text{C}\{^{19}\text{F}\}$  CP/MAS NMR spectra of Nafion membranes of different thicknesses, before (A) and after (B) in-situ tests. Asterisks indicate spinning sidebands.

A better comparison of the structural changes due to membrane degradation after fuel cell in-situ tests is possible by inspection of the plots given in Figure 4.4. They show the ratios of the peak intensities before and after the fuel cell tests for all investigated polymer

membranes. As noted above, the spectra were normalized to the peak of the main chain  $(CF_2)_n$  units, and possible changes due to main chain degradation are therefore not detectable.

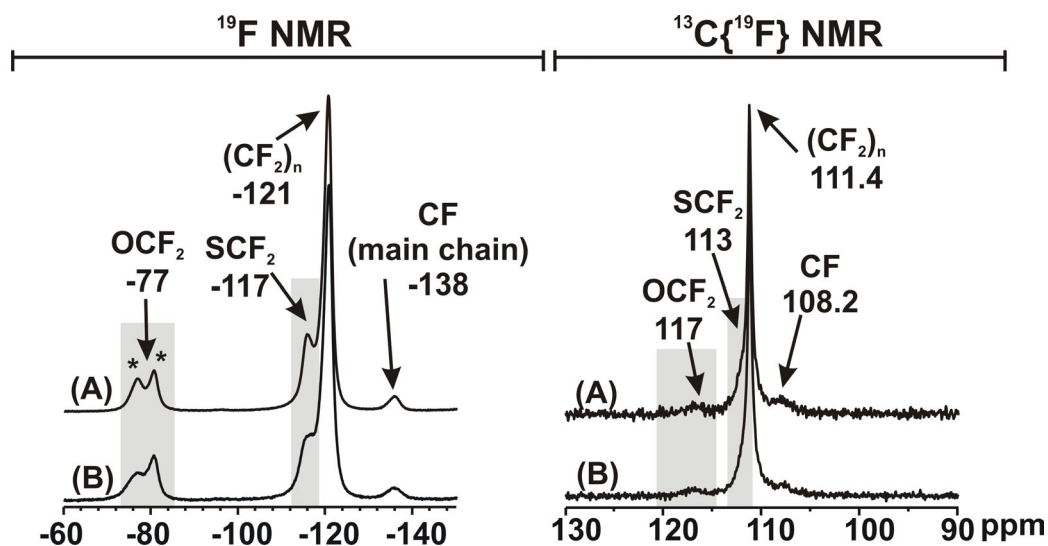


**Figure 4.3.**  $^{19}\text{F}$  NMR and  $^{13}\text{C}\{^{19}\text{F}\}$  CP/MAS NMR spectra of Hyflon Ion before (A) and after (B) the in-situ tests. Asterisks indicate spinning sidebands.

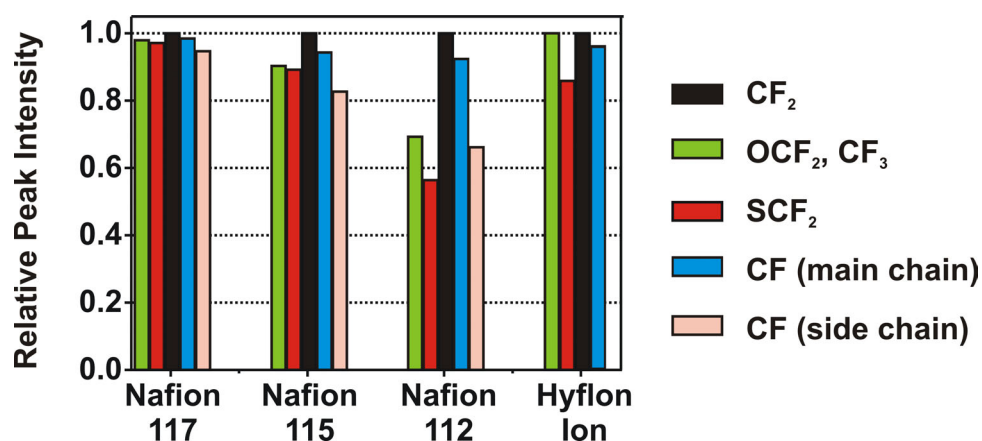


**Figure 4.4.** Relative peak heights of the various structural units after the in-situ tests. The given numbers are the ratios of the peak intensities after the in-situ tests relative to the original intensities before the tests in percentage, as taken from the  $^{19}\text{F}$  NMR spectra. For Hyflon Ion, the black column refers only to the  $\text{OCF}_2$  group (see text).

From these plots, it can be concluded that all membranes have been affected by the in-situ degradation test and the degradation of the side groups is verified for all membranes. Comparison of the Nafion membranes with different thicknesses shows that the degradation rate depends on the thickness, and for the thinner membrane, a higher degradation rate is observed (in the order of Nafion 117 < Nafion 115 < Nafion 112). Comparing the thinner Nafion membrane (Nafion 112) and Hyflon Ion, it is clear that the short side chain membrane degradation is much less than for Nafion 112. Although the Hyflon Ion sample is the thinnest of all membranes, it is almost as stable as Nafion 115 and Nafion 117.

#### 4.4. Discussion

The solid-state  $^{13}\text{C}$  and  $^{19}\text{F}$  NMR spectra recorded clear changes in the side chain signal intensities after degradation, and therefore supports the assumption that the pendant side chains of the ionomers are affected during degradation [36,56,64]. It could be also shown that after identical in-situ tests, the membranes with shorter side chains are less affected. Likewise, thinner membranes experience stronger degradation. At this point, there is no unambiguous explanation for the observed trends, because relevant data are still missing.

In general, the rate of formation of aggressive radicals and the reactivity of the ionomer itself have to be considered. A trivial explanation could be a degradation process proceeding from the membrane surface, which is expected to affect thin membranes more than thicker membranes. But the thickness dependence of the degradation may also be the result of a decreasing gas cross-over with thickness, if peroxy radical (e.g.  $\text{HOO}\cdot$ ) formation were rate limiting the degradation process, and if the formation of such radicals on the catalyst surface were controlled by either  $\text{H}_2$  cross-over to the cathode side or  $\text{O}_2$  cross-over to the anode side [166]. The latter explanation may also provide a rationale for understanding the higher durability of the Hyflon Ion membrane. Because of their higher crystallinity, short side chain ionomers such as Hyflon Ion usually swell less [72], which is anticipated to also reduce gas cross-over especially at elevated operation temperature [166].

Another possible explanation for the relative stability of the Hyflon Ion is its lower concentration of chemically sensitive ether linkages. Reaction with the only ether group close to the polymer backbone may even be hindered sterically.

In order to discriminate between these explanations, the degradation conditions may be varied, and the anode and cathode side of the membrane may be analysed separately. Work along these lines will be presented in the next chapter.

## 4.5. Conclusions

Solid-state NMR spectroscopy has been successfully introduced as a new method for the study of the structural changes within PFSA membranes after fuel cell in-situ tests. Unlike most other techniques, the present method provides the opportunity to directly study the structural alterations of the membranes. The results of  $^{19}\text{F}$  and  $^{13}\text{C}$  NMR measurements before and after in-situ tests demonstrate that degradation predominantly takes place in the side chains containing  $\text{SO}_3\text{H}$ ,  $\text{CF}_3$ ,  $\text{OCF}_2$  and  $\text{CF}$  groups. Degradation is decreasing with increasing membrane thickness and, for a given thickness, degradation for short side chain Hyflon Ion membranes is found to be less severe. Although, much more work is necessary to get a comprehensive understanding of the degradation mechanisms in such membrane systems, it can be stated that less gas cross-over through thicker membranes as well as short side chain membranes are important issues controlling the degradation rate of membranes in fuel cell systems.



## **5. Ex-situ Degradation under Mimic Fuel Cell Conditions**

### **5.1. Introduction**

After detecting the chemical changes on the polymer structure of Nafion and Hyflon Ion, in this chapter we describe a new type of ex-situ test, by which the degradation of the membrane is studied as a function of different variables including gas composition and absence or presence of catalyst. Changes in both the chemical structure of the polymer and the polymer mobility are examined by solid-state  $^{19}\text{F}$  NMR spectroscopy.

### **5.2. Experimental**

#### **5.2.1. Materials and sample preparation**

The tests were done on Nafion 117 membranes. The relevant material parameters and the procedure for the membrane pre-treating have been mentioned in chapter 4. For preparing membranes with catalyst layer, each piece of hydrated membrane was sandwiched between two glass plates and was fixed with some clips at the corners. The glass plates were then kept in the oven at  $T = 100\text{ }^{\circ}\text{C}$  overnight. After separating the glass plates, a completely flat dried membrane was obtained (Figure 5.1.a).

In a second step, a certain amount of Nafion dispersion in water and ethanol (5 w/w%) was added to a weighted beaker (6 ml). The beaker was kept in a water bath at  $T = 80\text{ }^{\circ}\text{C}$  until

the total amount of solvent was evaporated. After weighting the beaker again, a small amount of dimethylformamide (DMF) was added to the beaker (~ 3ml). When the Nafion was completely dissolved in DMF, 0.2 g of platinum (40% on carbon) was added to the beaker and was mixed well with the DMF solution containing the Nafion. This mixture was used as electrode ink.

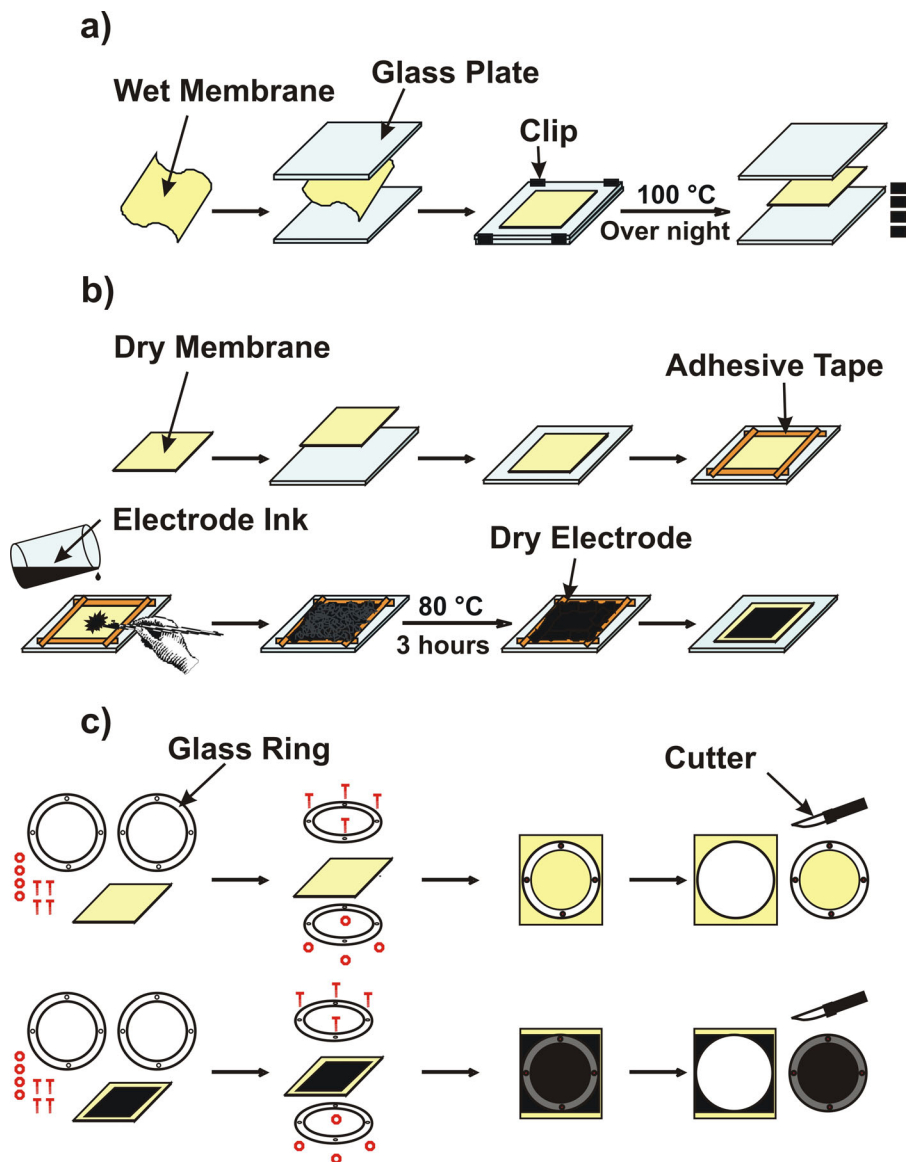


**Figure 5.1.** Membrane preparation. a) membrane flattening, b) pasting the electrode layer, c) Putting the membrane in the frame.

The flat dried membrane from the first step was then laid on a glass plate, and all edges of the membrane were fixed to the glass by self-adhesive tape. After putting the glass plate in the oven at  $T = 80^{\circ}\text{C}$ , the surface of the membrane was painted with the electrode ink by means of a small paint-brush. The reason for using only a small amount of DMF solvent in the electrode ink is that too high amount of DMF in the electrode ink prevents Pt from covering the surface of the membrane in a homogenous way; it rather flows over the membrane surface forming flowmarks. After painting, the oven door was closed and the glass plate was kept in the oven at  $T = 80^{\circ}\text{C}$  until the DMF over the membrane was evaporated completely, and the membrane coated with a Pt layer was obtained (Figure 5.1.b). During the painting process the membrane may deform, but as it is fixed to the glass, it will appear flat after drying. By weighting the dry membrane before and after the electrode painting, it was possible to calculate the amount of Pt which finally covered the surface of the membrane. The amount of Pt for the present membranes was between 1.9-2.0 w/w% of the total weight of Nafion membrane (1.25 mg Pt per  $\text{cm}^2$  of membrane).

The dried membrane was sandwiched between two glass rings. The glass rings with the membrane in between were tightened with four stainless steel screws. Extra membrane material around the rings was removed with a cutter and kept as reference sample without degradation. For each experiment, one membrane without Pt layer and one with Pt layer was prepared (Figure 5.1.c). The sample holder containing the membrane was then hooked inside the ex-situ set-up cell with a Nylon string.

The experimental set-up is shown in Figure 5.2. Temperature and humidity were chosen to be constant and close to typical fuel cell operating conditions ( $T = 80^{\circ}\text{C}$  and  $\text{RH} = 70\%$ ). The two compartments of the set-up are kept at different temperatures. The bottom of the cell (lower temperature compartment) was placed on a hot plate to keep the water inside the cell on a fixed temperature. In order to keep the level of the water constant during a long term experiment, a water refilling system was connected to the cell. The water temperature was controlled to be  $T = 70^{\circ}\text{C}$  which corresponds to a relative humidity of 65%. The upper compartment, containing the sample, was kept at  $T = 80 \pm 1^{\circ}\text{C}$  by a temperature controlled home-made oven.

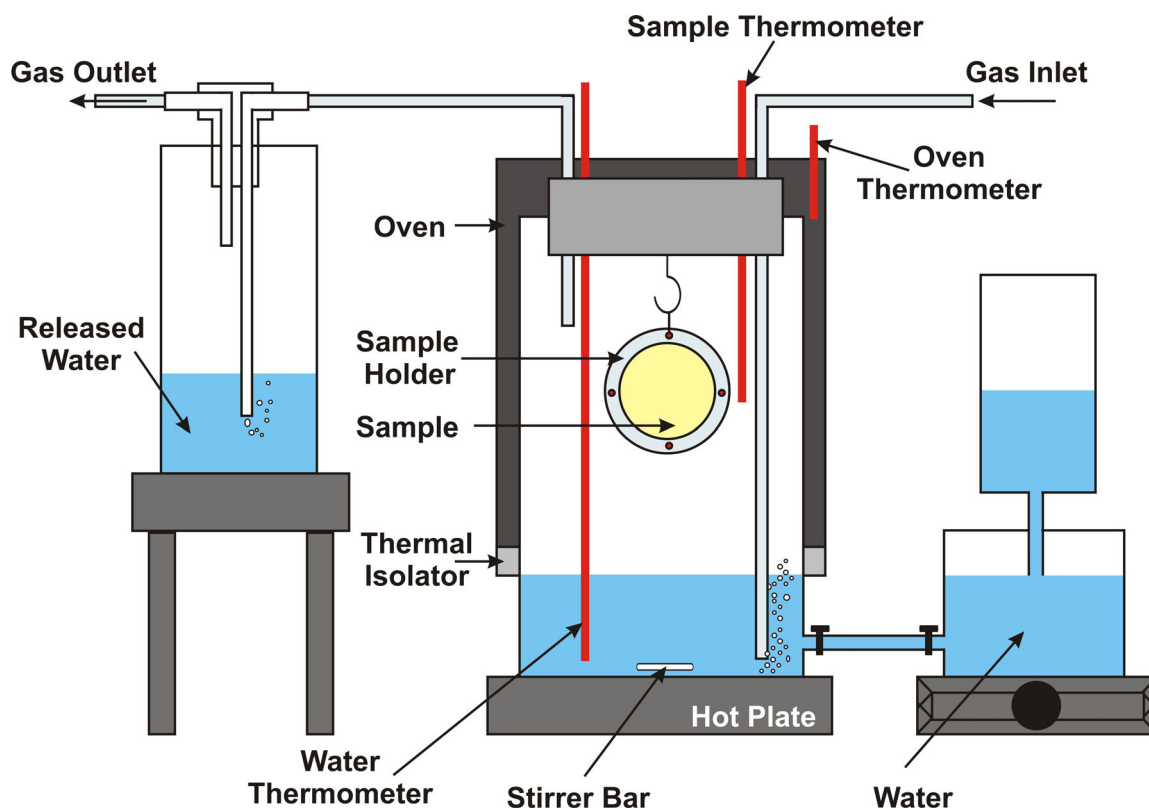


**Figure 5.2.** Set-up of ex-situ degradation test cell.

The set-up was equipped with a gas inlet and a gas outlet. The inlet gas was passed through the water to ensure fast humidification and the outlet gas was connected to a dish to condense and collect the release water from the test as well as any fragments of the sample which might be released during the experiment.

In order to simulate anodic and cathodic conditions including the possibility of gas cross-over, four different sets of experiments were chosen (Table 5.1). The total inlet gas flow was fixed to mimic a current density of  $1 \text{ A/cm}^2$  in a real fuel cell. Therefore, for each 10 mg of the sample the flow rate was chosen to around  $j = 10 \text{ ml/min}$ .

For each sample, NMR measurements were done before and after the degradation test which took 160 h. For solid-state NMR investigations two pieces of each sample were taken, one of which was dried at  $110 \text{ }^\circ\text{C}$  for 12 h, and kept inside a desiccator until the NMR measurements were started. The other piece was kept in water at  $70 \text{ }^\circ\text{C}$  overnight,

and then in the same water environment at room temperature before the NMR measurements. These two hydrated states were denoted as “dry” and “wet” samples.

**Table 5.1.** Experimental conditions for the ex-situ test

	T (°C)	RH (%)	Sample	Inlet gas		
				1	2	3
<b>Cathode (O<sub>2</sub>)</b>	80°C	65	Nafion 117	O <sub>2</sub>	-	-
	80°C	65	Nafion117 + Pt coating	O <sub>2</sub>	-	-
<b>Cathode (O<sub>2</sub>-rich)</b>	80°C	65	Nafion 117	O <sub>2</sub> (20%)	H <sub>2</sub> (2%)	Ar (78%)
	80°C	65	Nafion117 + Pt coating	O <sub>2</sub> (20%)	H <sub>2</sub> (2%)	Ar (78%)
<b>Anode (H<sub>2</sub>)</b>	80°C	65	Nafion 117	H <sub>2</sub>	-	-
	80°C	65	Nafion117 + Pt coating	H <sub>2</sub>	-	-
<b>Anode (H<sub>2</sub>-rich)</b>	80°C	65	Nafion 117	H <sub>2</sub> (90%)	O <sub>2</sub> (2%)	Ar (8%)
	80°C	65	Nafion117 + Pt coating	H <sub>2</sub> (90%)	O <sub>2</sub> (2%)	Ar (8%)

Changes in the chemical structure of the membranes, as derived from the solid-state NMR experiments, were also compared with the results from liquid-state NMR measurements which were done on the water released from the cell during the different test runs. For this purpose, the released water from each test was collected and kept at room temperature under a slow N<sub>2</sub> gas flow for about 2 days. During this time, water evaporated and the total amount of the solution decreased to about 10 ml which was then used for liquid-state <sup>19</sup>F NMR measurements.

### 5.2.2. NMR Spectroscopy

Solid-state NMR spectra were acquired for <sup>19</sup>F nuclei at a spinning rate of 10.5 and 15 kHz, with the same specifications as is mentioned in chapter 4. The lower spinning speed was used to study the changes in the spinning sideband intensities of the different peaks corresponding to different parts of the polymer and for the linewidth analysis. The higher

spinning speed was used for all other studies. Variable temperature  $^{19}\text{F}$  NMR spectra were also recorded using the aforementioned parameters and by using the Varian temperature control unit.

$^{19}\text{F}$  spin-lattice relaxation times in the laboratory frame,  $T_1$ , were measured by using the inversion recovery experiment. 16 transients were recorded for each measurement with a repetition delay of 5 s.  $^{19}\text{F}$  spin-lattice relaxation times in the rotating frame,  $T_{1\rho}$ , were obtained by observing the decay of the spin locked polarization generated by a  $\pi/2$  pulse. 16 transients were recorded for each experiment with a repetition delay of 5 s.  $^{19}\text{F}$  NMR spectra,  $T_1$  and  $T_{1\rho}$  relaxation experiments were recorded at six temperatures (25, 40, 60, 80, 95 and 120 °C). The processing steps for the  $T_1$  and  $T_{1\rho}$  experiments were the same as mentioned for the  $^{19}\text{F}$  MAS NMR spectra. The magnetization decays in both the  $T_1$  and  $T_{1\rho}$  measurements were plotted as the natural logarithm of the measured intensity versus time, and these data ( $r^2 > 99$ ) were then fitted with the appropriate one-component equation.

Liquid-state  $^{19}\text{F}$  NMR spectra were recorded with the 4 mm MAS probe, and with the same parameters as during the MAS NMR experiments, applying 1024 transients, but without spinning the sample. The processing parameters were the same as during the MAS experiments.

### 5.2.3. Equivalent weight (EW)

The amount of sulfonic acid groups available for ion exchange was determined by acid-base titration. The membranes were soaked in 1 M NaCl solution for 12 h before titrating with 0.01 M NaOH (Mettler Titrator DL21). The samples (in their  $\text{Na}^+$  form) were dried after titration in a vacuum oven at 140 °C for 4 h. Ion exchange capacities (IEC) are given in units of moles of titratable protons per g dry ionomer with the equivalent weight being the inverse of the IEC.

## 5.3. Results

**$^{19}\text{F}$  MAS NMR.** Figure 5.3 compares  $^{19}\text{F}$  NMR spectra of different samples before and after the ex-situ tests for different hydration states. The spectra were recorded at  $T = 80$  °C,

because at this elevated temperature the reduced linewidths allowed for an enhanced resolution. The given signal assignment (Table 5.2) is based on former solid-state [129] and liquid-state NMR investigations [130].

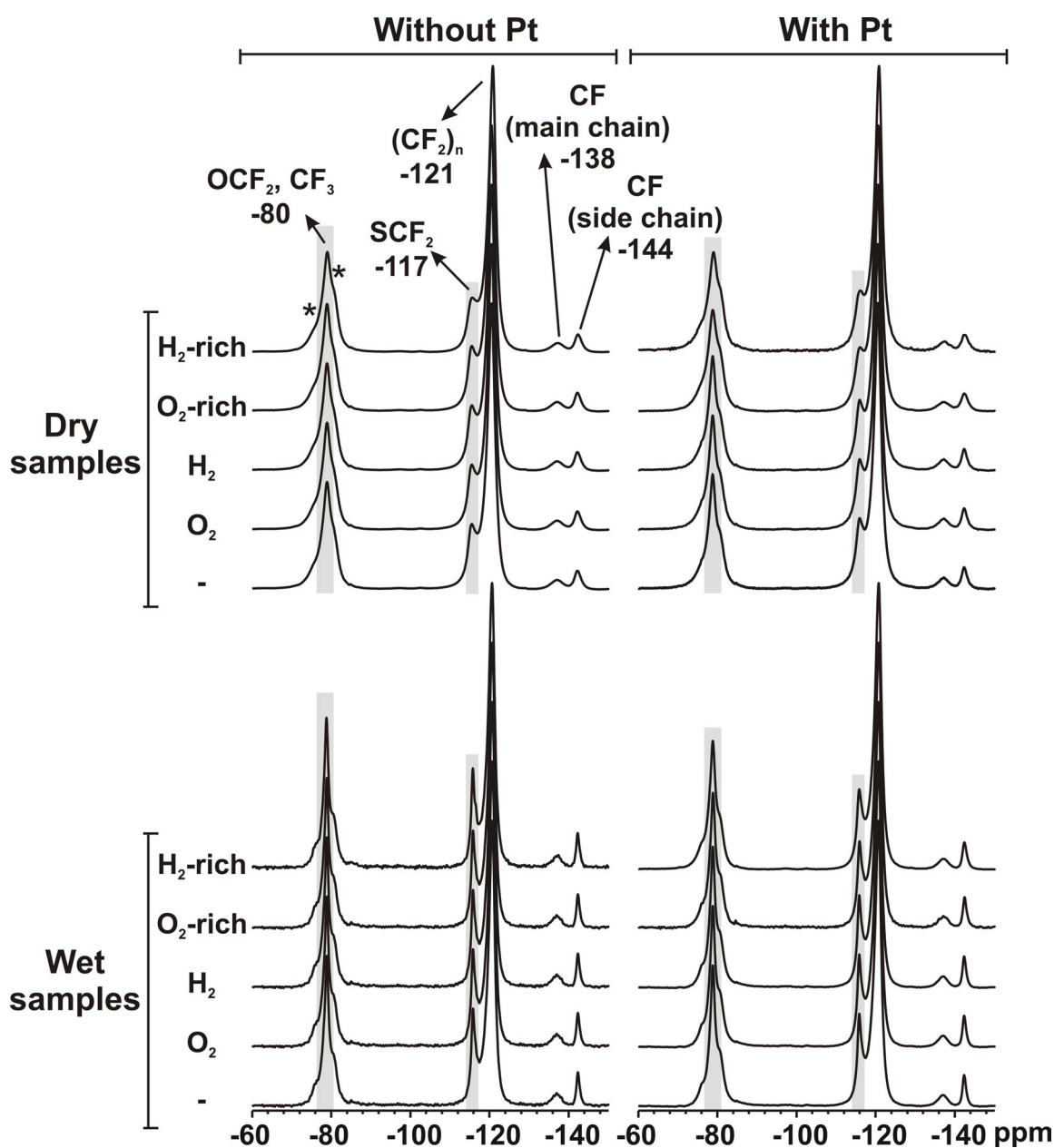


**Figure 5.3.** Solid-state  $^{19}\text{F}$  NMR for samples from different ex-situ tests in the dry and wet state. Asterisks indicate spinning sidebands. The given spectra are normalized to the spectra of the dominant peak of the backbone  $\text{CF}_2$  groups. The sample spinning was 15 kHz.

**Table 5.2.** Chemical shift values (in ppm) and assignment of the  $^{19}\text{F}$  resonances in Nafion membranes.

CF (side chain)	CF (main chain)	$(\text{CF}_2)_n$	$\text{SCF}_2$	$\text{OCF}_2$	$\text{CF}_3$
-144	-138	-121	-117	-80.1 79.9	-80

The spectra shown in Figure 5.3 were taken at a spinning speed of 15 kHz which was the upper speed that was reached safely for this sample in the 4 mm MAS probe. The low field signal (-80 ppm) originating from the  $\text{OCF}_2$  and  $\text{CF}_3$  groups appear broadened because of their overlap with the spinning sidebands of the backbone  $\text{CF}_2$  group and the side chain  $\text{SCF}_2$  group signals (asterisks in Figure 5.3). For this reason, for examination of the NMR linewidths, the sample spinning speed was reduced to 10.5 kHz at which these latter signals are not affected by spinning sidebands from other resonances.

The linewidths are generally smaller for the wet membranes, and the lines are slightly broadened for samples with Pt coating. Comparing the spectra of the samples before and after the ex-situ tests, but with the same hydration state and with Pt coating, a reduced intensity for the polymer side chain signals is found. This effect is most pronounced for the intensities of the  $\text{OCF}_2$  and  $\text{SCF}_2$  peaks at -80 and -117 ppm, respectively. In order to quantify the spectral changes, all spectra were deconvoluted and normalized to the integral intensity of the  $\text{CF}_2$  backbone signal. Figure 5.4 shows the normalized integrals of the  $^{19}\text{F}$  NMR signals for the  $\text{OCF}_2$  and  $\text{SCF}_2$  groups before and after the ex-situ tests. Apart from the aforementioned linewidths and spectral resolution differences, the area under the spectra of the corresponding wet and dry samples are identical which make us confident that deconvolution allows for quantitative analysis, indeed.

As a general result, practically no intensity changes are observed for samples without Pt coating after treatment (Figure 5.4, left). For membranes coated with Pt catalyst, however, pronounced reductions in signal intensity after treatment with  $\text{H}_2/\text{O}_2$  gas mixtures are registered. The largest effect occurs in the case of  $\text{H}_2$ -rich conditions, and the  $\text{SCF}_2$  group

signal appears to be somewhat more affected than the  $\text{OCF}_2$  group signal (Figure 5.4, right).

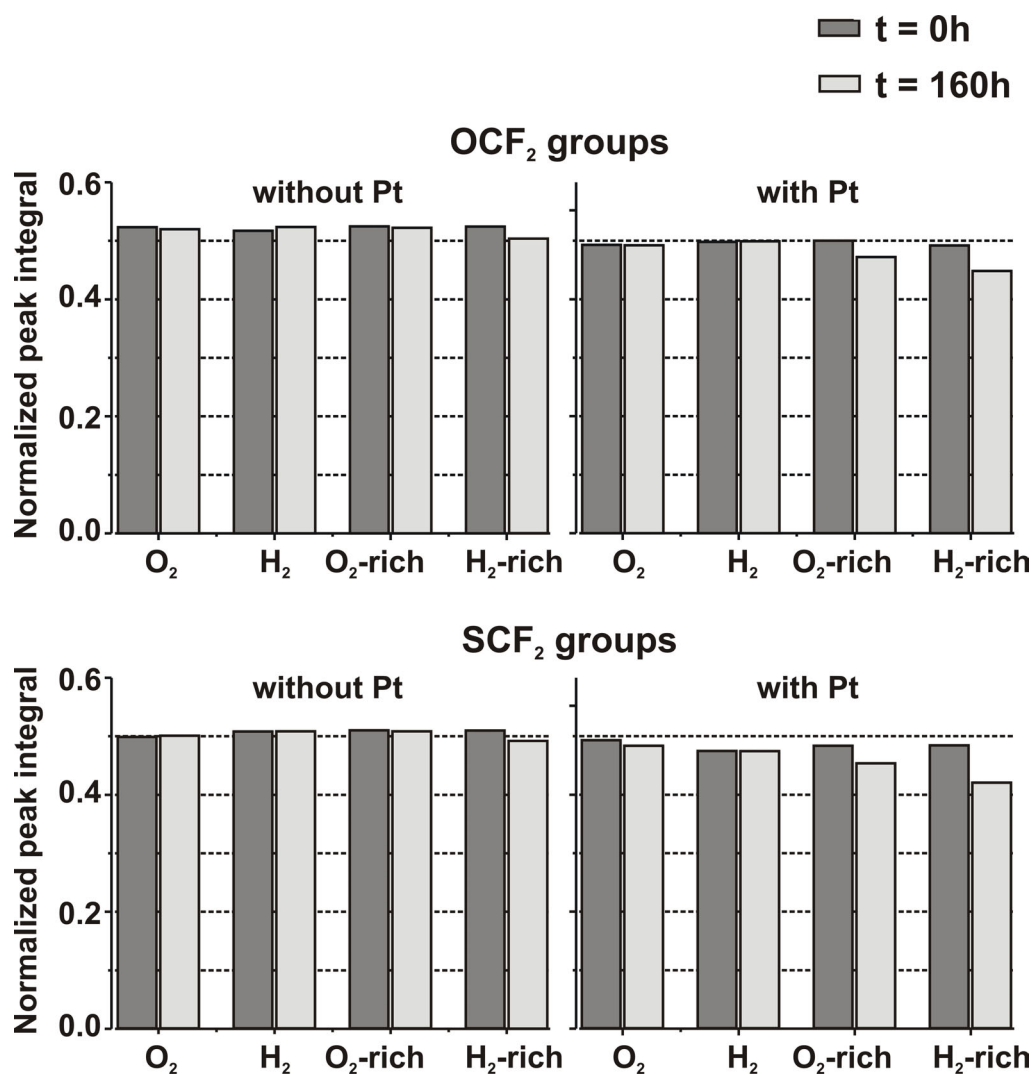


**Figure 5.4.** Peak integrals of side chain groups,  $\text{OCF}_2$  and  $\text{SCF}_2$  in the solid-state  $^{19}\text{F}$  NMR spectra. The integral of the backbone  $\text{CF}_2$  peak at -121 ppm was put to unity.

**Liquid-state  $^{19}\text{F}$  NMR.** In order to identify possible reaction products released via the humidified gas stream, liquid-state  $^{19}\text{F}$  NMR measurements were done on the water collected during the tests. No  $^{19}\text{F}$  NMR signal is detected if during the tests the cell is flushed by either  $\text{H}_2$  or  $\text{O}_2$  only, regardless whether the samples are coated with Pt or not. But if the membranes are exposed to mixtures of both gases,  $^{19}\text{F}$  NMR signals are clearly

detected, and the pH of the collected water is significantly reduced (pH  $\sim$  4.5). The latter may be the result of HF release which is also indicated by the appearance of a strong fluoride ( $F^-$ ) signal in the NMR spectra. The representative  $^{19}F$  NMR spectrum given in Figure 5.5 (taken on the water released from the  $H_2$ -rich condition ex-situ test) shows this signal (-127.6 ppm) together with  $^{19}F$  resonances originating from  $CF_3$  and  $OCF_2$  (-76.8 ppm),  $SCF_2$  (-116.5 ppm), and  $CF$  (-144 ppm) groups following the assignment from literature [64].

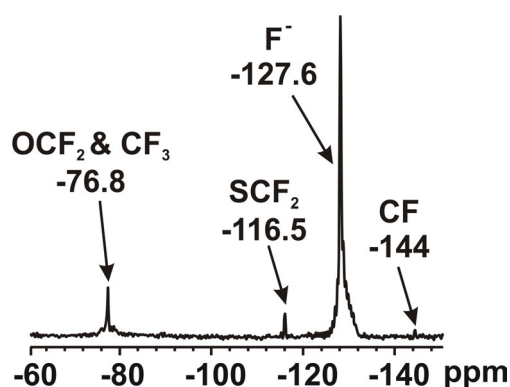


**Figure 5.5.** Liquid-state  $^{19}F$  NMR spectrum for the water extracted from the  $H_2$ -rich cell.

It should be noted that the resolution of the present spectra is rather poor, since the  $^{19}F$  NMR spectra were recorded with the MAS probe and without any special precautions for high-resolution conditions.

**Sideband intensity and linewidth analysis.** A series of variable temperature  $^{19}F$  MAS NMR spectra of Nafion (prior to the ex-situ test) at a sample spinning frequency of 10.5 kHz is shown in Figure 5.6. At this spinning frequency the  $^{19}F$  NMR spectra contain spinning sidebands which stem from the large chemical shift anisotropies and strong dipolar couplings of the  $^{19}F$  nuclei. These spectra were analyzed (on a semi-quantitative level) by considering the linewidths and intensities of the spinning sidebands which can be related to structural and dynamic changes within the various samples.

Due to the limited resolution only the linewidths for the central lines of the backbone  $CF_2$  and side chain  $OCF_2/CF_3$  resonances were analyzed. These resonances were assumed to consist of a single component each, although from a former 1D and 2D NMR study it is

known that several spectral components have to be considered for both signals [129]. For a qualitative discussion of the  $^{19}\text{F}$  NMR linewidths, however, the present simplifying approach appears to be justified.

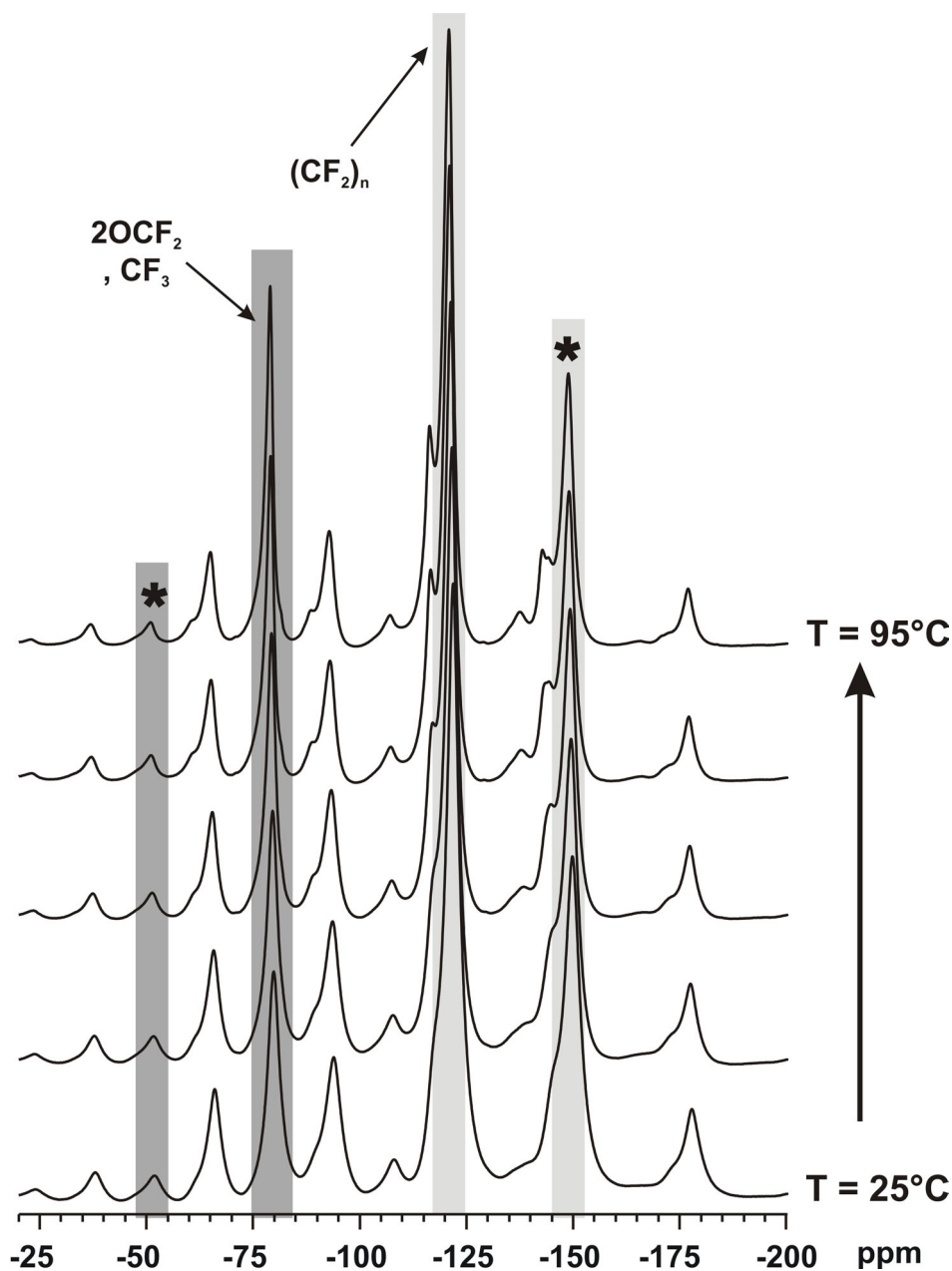


**Figure 5.6.** Variable temperature solid-state  $^{19}\text{F}$  NMR spectra of Nafion at a spinning speed of 10.5 kHz. Asterisks indicate the spinning sidebands used for the data plotted in Figure 5.7. The sidebands and the respective central peaks are shown by the same color.

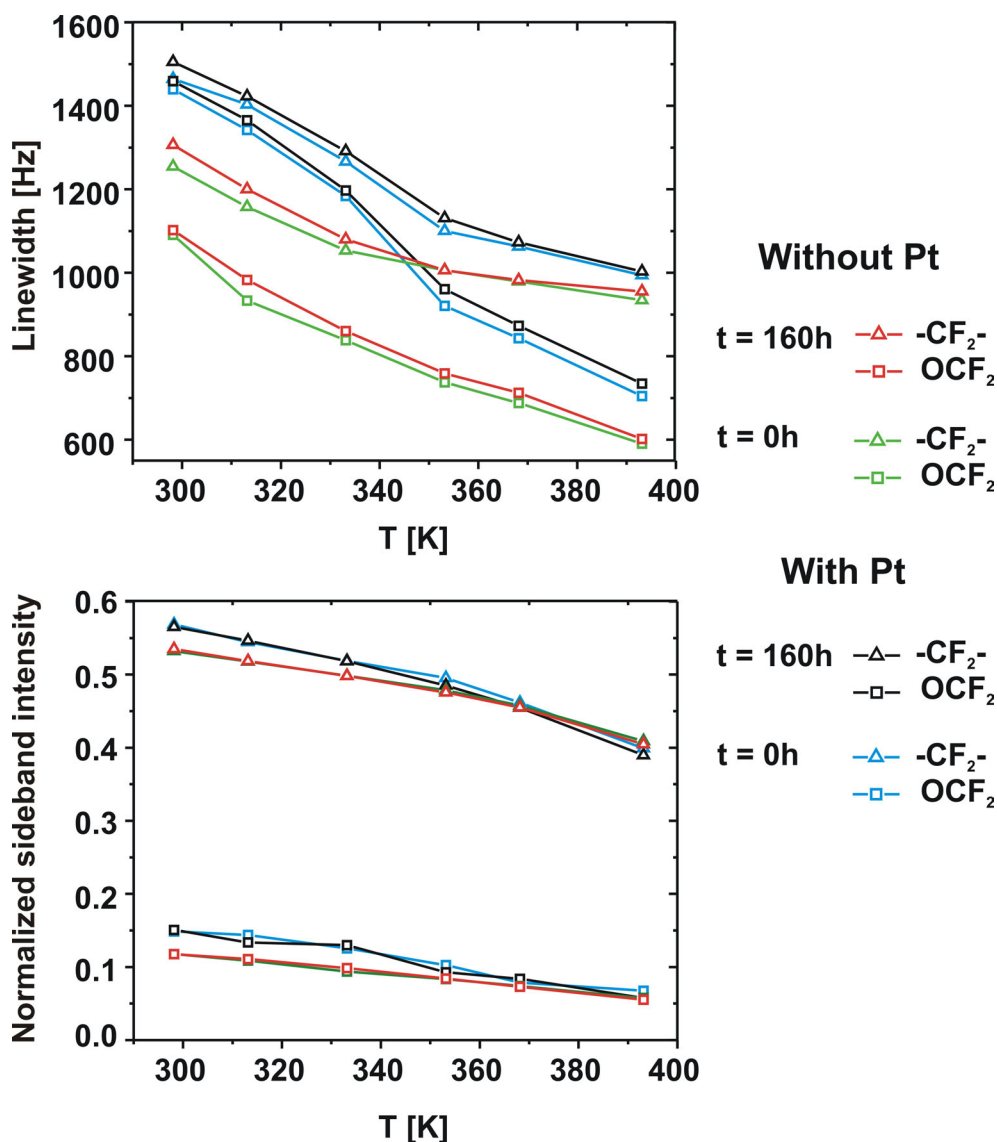


**Figure 5.7.**  $^{19}\text{F}$  NMR linewidths and relative sideband intensities (normalized to the respective central peak) for the polymer backbone and side chain at a sample spinning speed of 10.5 kHz for the samples before and after the  $\text{H}_2$ -rich condition test.

Widths and intensities of peaks associated with both backbone and side chain of a samples treated under  $\text{H}_2$ -rich condition (Figure 5.7) decrease with temperature. Coating the membranes with Pt increases the  $^{19}\text{F}$  NMR linewidths, which might stem from susceptibility or packing effects due to the presence of the metallic Pt particles. The NMR linewidths of side chain signals are generally smaller than those of the main chain, pointing towards higher side chain mobility. In general, the degradation test is accompanied by only

small linewidth alterations. As a general trend, somewhat larger linewidths are registered for the treated samples.

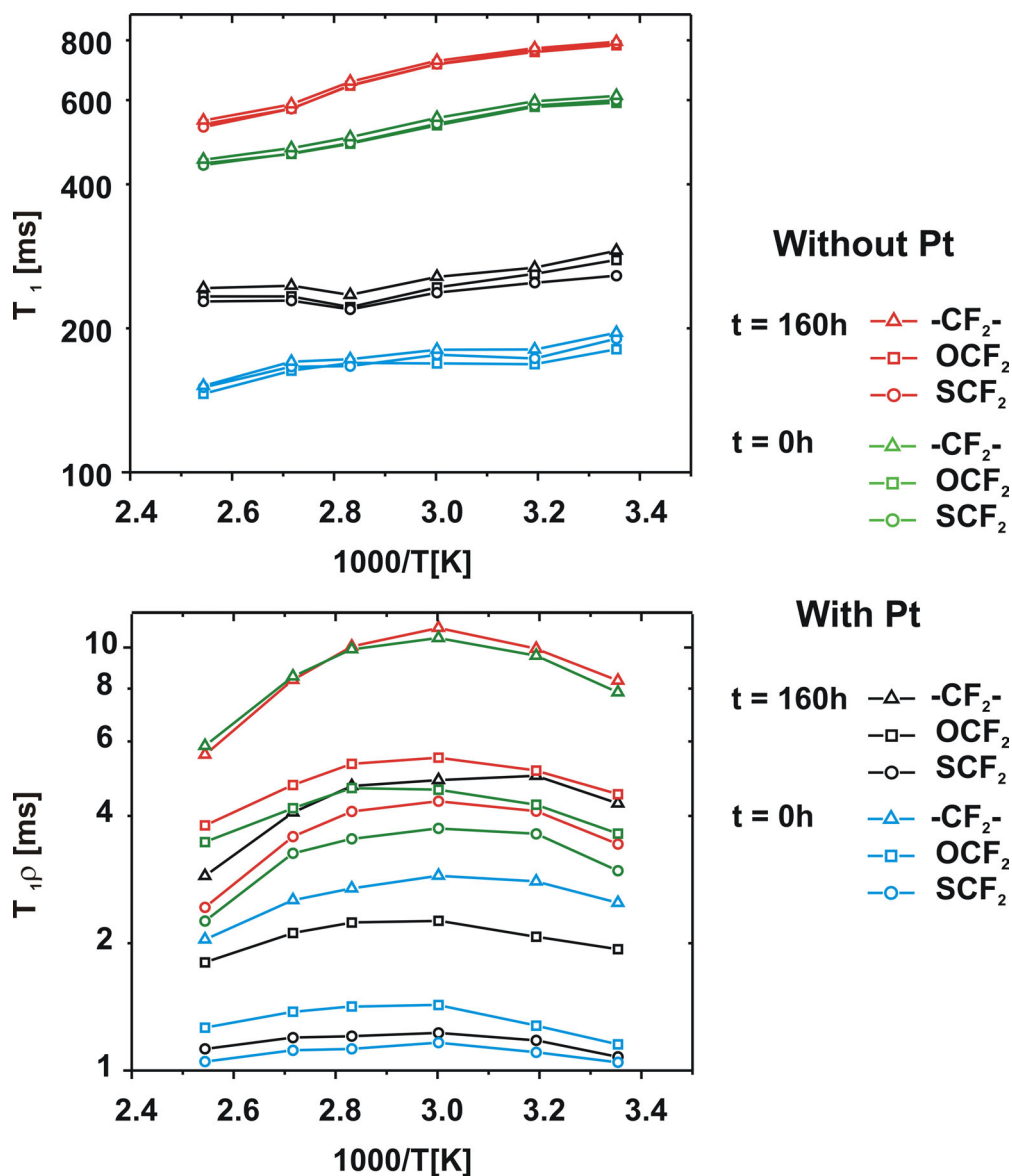


**Figure 5.8.**  $^{19}\text{F}$   $T_1$  and  $T_{1\rho}$  values of the samples before and after the  $\text{H}_2$ -rich condition test (dry samples, sample spinning speed: 15 kHz). The estimated error is less than 3%.

The same  $^{19}\text{F}$  NMR spectra were used to derive the relative intensities of the spinning sidebands [167] which contain qualitative information about changes of the underlying chemical anisotropies and dipolar interactions as a function of various experimental parameters. The sideband intensities for both the side and the main chain signals

(normalized to the intensities of their respective central peaks) also decrease with increasing temperature (Figure 5.7), although the differences between the samples with and without Pt coating are very small. The presence of Pt is found to slightly increase the side band intensity, at least at lower temperatures. These findings point to an increased chemical shift anisotropy due to the interaction with the metallic Pt particles, in analogy to the aforementioned NMR linewidths.

The relative intensities of the spinning sidebands of the backbone  $\text{CF}_2$  signal are significantly higher than those of the  $\text{OCF}_2/\text{CF}_3$  side chain peaks, once more suggesting a higher anisotropy of the underlying magnetic interactions (i.e. chemical shift anisotropy, dipolar couplings) in the main chain region.

**$^{19}\text{F}$  relaxation.** To obtain further insights into the chain mobility,  $^{19}\text{F}$  relaxation data ( $T_1$  and  $T_{1\rho}$ ) were recorded at a sample spinning frequencies of 15 kHz for a membrane which had been subjected to a degradation test under  $\text{H}_2$ -rich conditions.

The observed  $T_1$  values are almost identical for side chain and backbone segments and slightly decrease with increasing sample temperature (Figure 5.8). This observation is in line with a former relaxation study on Nafion and is explainable by spin diffusion due to the strongly dipolar coupled  $^{19}\text{F}$  network [132]. Pt coating of the membrane causes a shortening of the  $T_1$ . After the ex-situ degradation test, a general increase of the  $T_1$  values is observed, regardless whether the membrane was coated with Pt or not.

For the  $T_{1\rho}$  data the situation appears to be more complex. For all signals, a maximum of the relaxation curves is found at around  $T = 60$  °C. Unlike the quite uniform  $T_1$  data,  $T_{1\rho}$  values are generally longer for the backbone signals than for the side chain resonances. Within the side chain, shorter  $T_{1\rho}$  values are found at the end of the side chain (see data for  $\text{OCF}_2$  and  $\text{SCF}_2$  groups). The effect of Pt coating on the  $T_{1\rho}$  values is the same as found for the  $T_1$  data, i.e., upon addition of Pt the  $T_{1\rho}$  values become shorter. The degradation test, using the  $\text{H}_2$  rich condition, in general is accompanied by an increase of the  $T_{1\rho}$  values. The absolute changes, however, also depend on both the segmental position and the presence or absence of the Pt coating.

**Equivalent weight and water uptake.** Table 5.3 summarizes EW,  $\lambda$  and  $\phi$  values for samples before and after the degradation tests. In agreement with the above results, only the samples treated in the H<sub>2</sub>/O<sub>2</sub> mixtures exhibit some changes of the EW values, which are even larger for the samples with Pt coating. For all samples, an increase of the equivalent weight is accompanied by a decrease of the water volume fraction  $\phi$ , while the hydration number  $\lambda$  remains constant or slightly increases. Again, the most significant effects on EW and  $\phi$  are detected for the membrane which was treated under H<sub>2</sub>-rich conditions.

**Table 5.3.** Equivalent weight (EW), number of water molecules per sulfonic acid group ( $\lambda$ ) and water volume fraction ( $\phi$ ) of Nafion 117 before and after the degradation tests

sample	Nafion 117					Nafion 117 + Pt coating				
	-	O <sub>2</sub>	H <sub>2</sub>	O <sub>2</sub> -rich	H <sub>2</sub> -rich	-	O <sub>2</sub>	H <sub>2</sub>	O <sub>2</sub> -rich	H <sub>2</sub> -rich
EW	1108	1123	1109	1155	1333	1106	1111	1098	1443	1979
$\lambda$	21.2	21.5	21	21.5	21.6	21.2	21.2	21.5	23.2	24.9
$\phi$	0.34	0.34	0.34	0.33	0.27	0.34	0.34	0.34	0.28	0.22

## 5.4. Discussion

The experimental techniques of the present work, comprising solid-state and liquid-state NMR along with ion exchange capacity and water uptake data, clearly prove that membrane degradation takes only place, if O<sub>2</sub> and H<sub>2</sub> are present together with Pt.

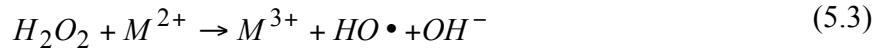
According to the literature [30,40,42,55,56,71,168-170], Nafion membrane degradation occurs via radical attack. Inside the fuel cell, there are different sources for radical formation. One relevant reaction is formation of hydrogen peroxide by oxygen reduction [36,49,101].



Hydrogen peroxide leads to radical formation in the presence of heat or traces of transition metal cations:



or:



Since the radical precursor ( $H_2O_2$ ) is formed in an electrochemical reaction, this source of radicals must not be considered for the present experiments, in which no current is applied. In a running fuel cell, however, in which electrochemical oxygen reduction takes place, the above radicals may form as side products.

The second possibility for radical formation is the direct reaction of  $H_2$  and  $O_2$  at the surface of the Pt catalyst, creating membrane degrading species [39,43,59,102]:



The rates of these reactions depend on the catalyst surface properties and the relative concentration of  $H_2$  and  $O_2$  at the catalyst surface [39,43,49]. This mechanism is of chemical nature, and it can therefore proceed in the present ex-situ experiments where  $H_2$ ,  $O_2$  and Pt catalyst are present. In a running fuel cell, this route of radical formation may occur on the surface of the anode or cathode catalyst depending on the current density.

Only at OCV or very low current densities, oxygen dissolves in the aqueous phase of the membrane and diffuses to the anode side, where it may participate in reaction (5.5). If a protonic current is flowing from the anode to the cathode, however, the electroosmotic water drag is anticipated to transport dissolved hydrogen from the anode to the cathode, where reactions (5.6) and (5.7) may then lead to the formation of radicals.

In the present ex-situ tests, degradation is observed only if H<sub>2</sub>, O<sub>2</sub> and Pt-catalyst are present (Figure 5.4), and this suggests that i) the chemical formation of radicals is occurring, indeed, and that ii) the presence of these radicals leads to bond cleavage processes. These reactions are most pronounced for H<sub>2</sub> rich conditions, suggesting that H• is reacting with a higher rate than HOO• radicals. Pt catalyzes the reaction of H<sub>2</sub> and O<sub>2</sub>. The observation of pinholes on the membrane after the degradation test is an evidence for the reaction of H<sub>2</sub> and O<sub>2</sub> on the surface of Pt and heat production.

As for the in-situ degradation tests [171], side chain signals are more affected by degradation than signals originating from the main chain (note that the spectra shown in Figure 5.3 are normalized to the backbone CF<sub>2</sub> signal). The presence of side chain fragments in the collected water (Figure 5.5), the reduction of the IEC (Table 5.3) and the reduction of the hydrophilic character is actually an independent confirmation of side chain cleavage.

Backbone degradation via a main chain unzipping mechanism [172] (Figure 5.9) is frequently considered in the literature [172]. On the basis of the solid-state <sup>19</sup>F NMR data, it cannot be decided to which extent the main chain is degraded. But the fact that the water collected during the test contains a significant quantity of fluoride ions (F<sup>-</sup>) points towards some backbone degradation.

In any case, the present ex-situ test results suggest predominant side chain degradation in accordance with earlier findings on low carboxyl content commercial PEM membranes [49,65,171]. Although carboxylic groups are found to be more reactive than ether linkages [65], the latter are higher in concentration by at least 2-3 orders of magnitude (every side chain has two bonds of this type) which makes side chain degradation more likely [173].

With this, one may even expect an increasing side chain to backbone degradation rate with increasing temperature.

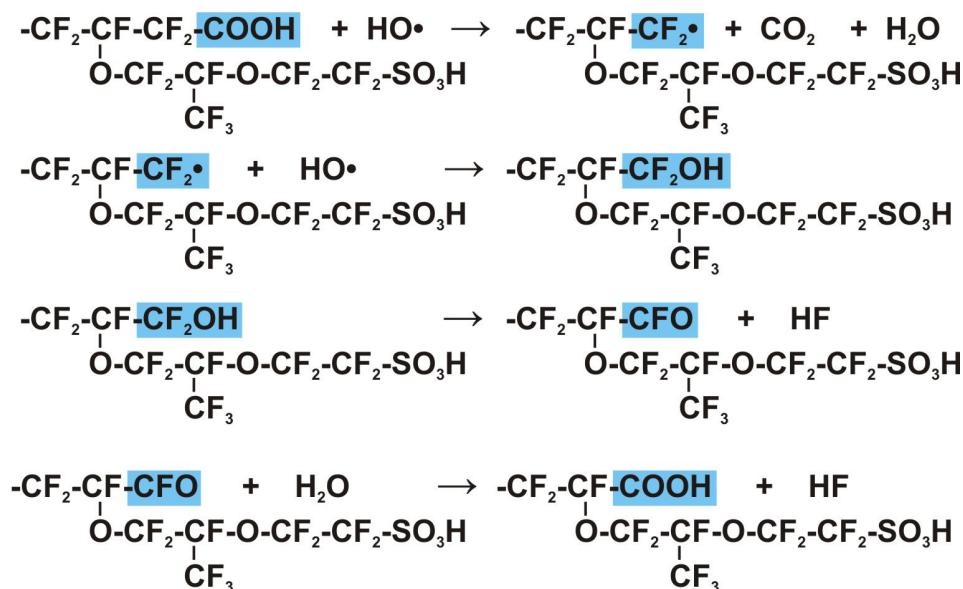


**Figure 5.9.** Main chain degradation mechanism, unzipping of the main chain by radical attacks to COOH groups.

Fluoride is thought to be released by the reaction shown in Figure 5.9. This reaction starts at the carboxylic acid end groups (-COOH) which are unintentionally introduced during the manufacturing process of Nafion via hydrolysis of the persulfate initiators used for the polymerization process [174]. Molecules containing terminal carboxylic acids generally degrade faster than non-carboxylated molecules [65]. For Nafion, however, COOH groups could not be detected by relatively insensitive  $^{13}\text{C}$  NMR spectroscopy [171], but the fact that postfluorination of backbone end groups reduces degradation suggests that the unzipping mechanism [172] contributes to fluorine release. On the other hand, there is still some residual fluorine release even when reactive end groups are virtually eliminated [65,172], and this points towards some additional mechanisms. To which extent this is taking place in the backbone and in the side chains cannot be decided at this point, but it should be mentioned that also side chain degradation may be a source of fluoride release (as HF).

But what is the mechanism of side chain degradation by radicals? One possibility is the

radical attack to the C-S bond at the end of the side chain (Figure 5.10) which is actually the weakest bond within this segment. From there, the reaction may proceed which progressively leads to a side chain shortening along with the formation of acid (HF). This mechanism is in agreement with the detection of  $-\text{O}-\text{CF}_2-\text{CF}_2-\text{SO}_3\cdot$  and  $-\text{O}-\text{CF}_2-\text{CF}_2\cdot$  radicals in EPR experiments on UV-induced Fenton treated membranes [30,56].

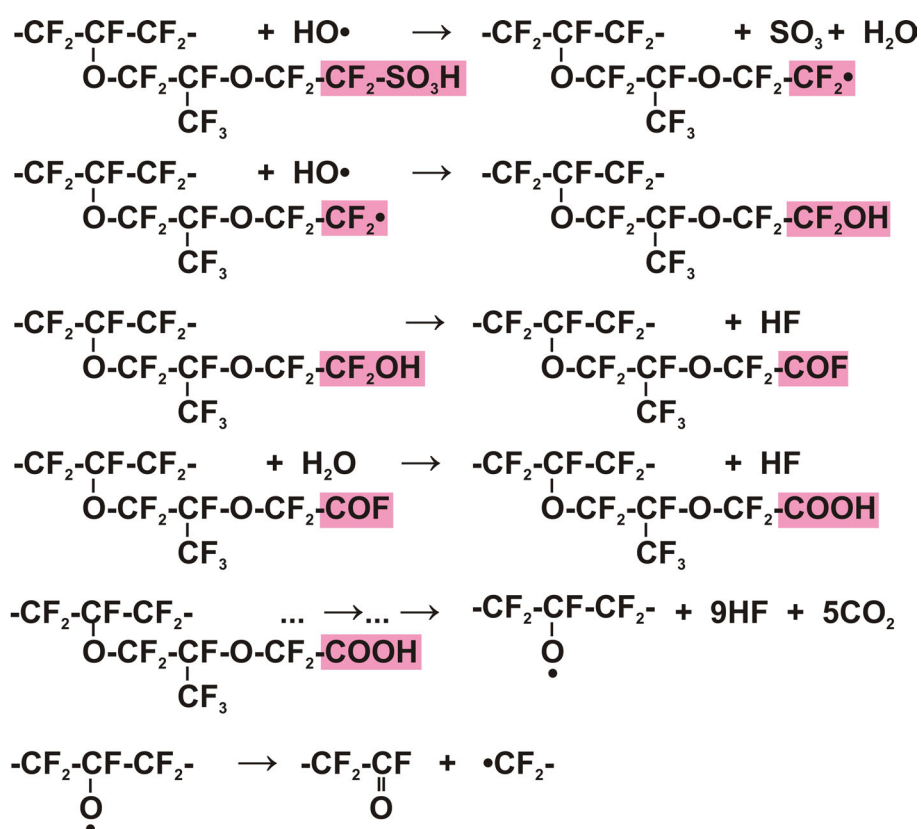


**Figure 5.10.** Side chain degradation mechanism, unzipping of the side chain by radical attacks to C-S bond.

The side chain degradation may also start at the backbone carbon bearing the side chain (secondary C-F bond) or the carbon which connects two ether groups within the side chain (tertiary C-F bond). These reactions can lead to a complete or partial release of the side chains [65,173] (Figure 5.11). In any case, this reaction is also a source for HF.

The effects of degradation on the membrane dynamics are further examined by  $T_1$  and  $T_{1\rho}$  relaxation data and NMR line shape effects.  $^{19}\text{F}$  and  $^1\text{H}$  NMR  $T_1$ ,  $T_{1\rho}$  and  $T_2$  relaxation

studies of unaged samples as a function of preparation route and water content have already been reported in the literature [132,175]. Also, spin relaxation and spectral anisotropies, in the presence of MAS, were explored for Nafion containing different counter ions [129,176].

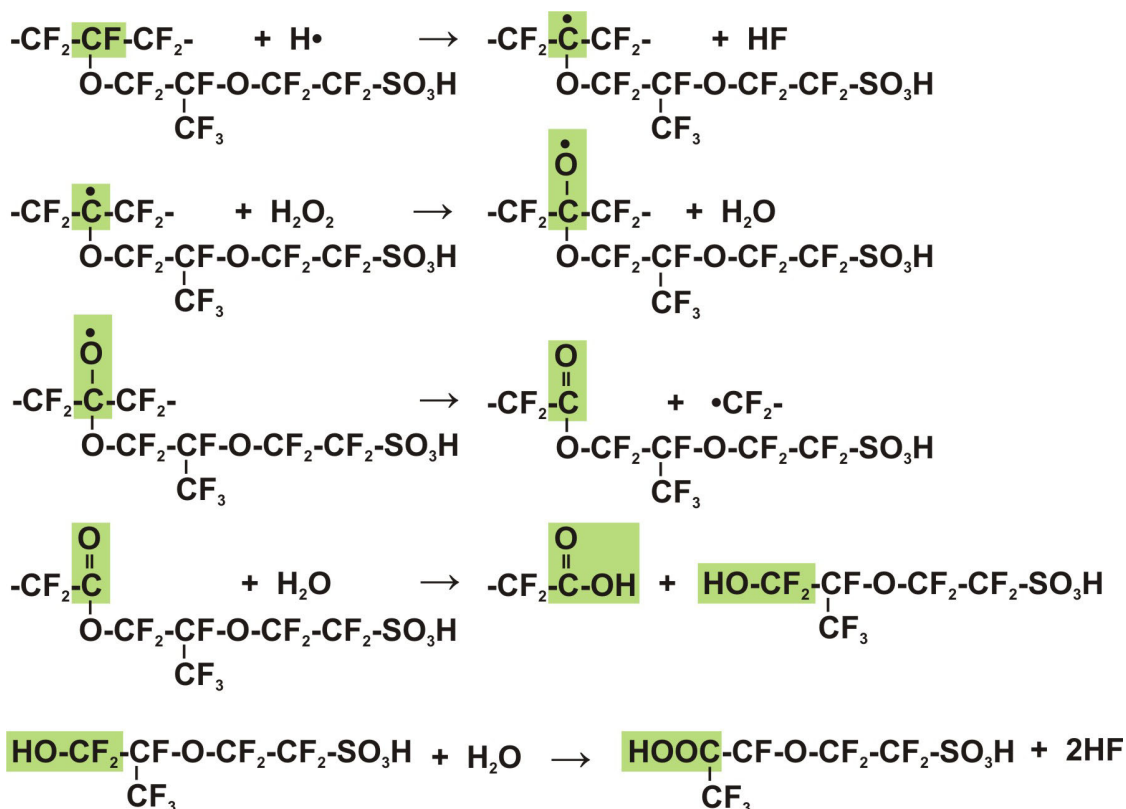


**Figure 5.11.** Side chain degradation mechanism, attack by radicals to the secondary C-F bond. The same mechanism can be assumed for attack of H• radicals to the tertiary C-F bond.

It was found that  $T_1$  relaxation is dominated by spin diffusion preventing a distinction of backbone and the side chain dynamics, but  $T_{1\rho}$  data revealed a dynamical coupling of the backbone and the side chain segments. An extensive investigation, based on one and two-dimensional  $^{19}\text{F}$  and  $^{13}\text{C}$  NMR studies on stationary and spinning samples, covered both structural aspects and the chain dynamics of Nafion membranes [123,131]. Analysis of these data proved fast uniaxial rotations of the helical backbone, as in polytetrafluoroethylene. There was even evidence for the movement of the backbone axis

as well as motions in the side chains with maximum amplitude at the center of the side chain.  $^{13}\text{C}$  and  $^{19}\text{F}$  NMR linewidths, obtained from fast MAS spectra, were traced back to the presence of static disorder in the Nafion backbone in the vicinity of the branching site.

The presence of water has not only a plasticizing effect [76], it also leads to cross-relaxation effects between the  $^{19}\text{F}$  and  $^1\text{H}$  spin system reservoirs complicating the interpretation of NMR data [65, 78]. The dynamical study of the present work is therefore based on relaxation data recorded on dry samples only.

The experimental  $^{19}\text{F}$  NMR linewidths showed (i) a decrease with increasing temperature, (ii) larger values for the backbone, and (iii) an increase for the samples with Pt coating. The latter effect might be related to susceptibility effects or packing effects due to the presence of the metallic Pt particles. Based on earlier high-speed MAS investigations, the linewidths can be understood by static disorder in the vicinity of the chain branching CF segment and also within the Nafion side chain. Moreover, a restricted backbone reorientation, and a higher motional freedom of the side chain segments explain the differences in linewidths. Since the overall chain motions occur in the fast motional limit, at about 100 kHz or above [132], changes of the motional rates cannot be responsible for the temperature dependent linewidth reductions. Rather, they reflect a thermally activated increase of the fluctuation amplitudes which cause a reduction in static disorder. The stronger temperature dependence of the respective linewidths is explainable by the higher mobility, i.e. minor spatial hindrance, of the side chains. Likewise, the successive convergence of the linewidths for the samples with and without Pt coating can be understood by the thermally activated changes in static disorder.

The same assumptions can be used to explain the experimental findings for the overall spectral widths (due to chemical shift anisotropy and homonuclear dipolar coupling), which is reflected by the relative intensities of the spinning sidebands. The significantly smaller sideband intensities for the side chain segments are thus consistent with a higher fluctuation amplitude. The relative changes upon temperature increase are larger for the side chain segments than for the backbone, and the differences between the samples with and without Pt coating vanish at elevated temperatures, in agreement with the aforementioned linewidth

effects. However, chemical degradation, in general, is found to have only little (for the linewidths) or no effect on the NMR lineshape parameters.

The results and trends for the derived  $T_1$  data (see Figure 5.8) are in agreement with previous investigations. The observation of identical  $^{19}\text{F}$   $T_1$  values for all positions in the sample can be understood by the presence of spin diffusion due to the strong homonuclear dipolar interactions between the  $^{19}\text{F}$  nuclei which equalizes the spin-lattice relaxation values for the different chain positions [123,132]. Moreover, all experimental  $T_1$  values lie on the low temperature side of the  $T_1$  curve, i.e. below the curve minimum..

A general shift of the  $^{19}\text{F}$   $T_1$  values towards higher values is observed for the samples after the degradation test. Surprisingly, this also holds for the sample without Pt coating, which – as discussed above – should not be affected by chemical degradation. At present, this latter finding is not fully understood. It is very likely that the degradation tests give rise to some polymer aging, which is not related to chemical degradation. That is, structural annealing may occur with alterations of the magnetic interactions responsible for spin-lattice relaxation. Hence, a reduction for the homonuclear dipolar couplings can explain the aforementioned increase of the  $^{19}\text{F}$   $T_1$  values. Likewise, the chain motions may become more restricted which would cause the same trend for the  $T_1$  relaxation data.

For the samples with Pt coating the changes in  $T_1$  are somewhat larger which are related to an additional effect by chemical degradation. It appears very likely that the responsible chain motions experience an additional restriction which would then lift the  $T_1$  values (see also discussion of  $T_{1\rho}$  experiments).

The derived  $T_{1\rho}$  data are more complex than the  $T_1$  data, as the values (i) change with the chain position (i.e. decrease from backbone to side chain, and towards the end of the side chains;  $T_{1\rho}(\text{CF}_2) > T_{1\rho}(\text{OCF}_2) > T_{1\rho}(\text{SCF}_2)$ ), (ii) decrease by the addition of Pt coating, (iii) increase after the degradation tests, and (iv) exhibit a maximum at around 60 °C. Obviously, spin diffusion does not affect the  $T_{1\rho}$  data, and the values for the individual segments can be clearly distinguished. Moreover, the trends by the presence of the Pt coating and after the degradation test are the same as found for the  $T_1$  data. The observation of a maximum in the  $T_{1\rho}$  curves is in agreement with previous studies, and was attributed to

the appearance of a new motional mechanism which dominates  $T_{1\rho}$  relaxation at higher temperatures [123]. It was reported that the position of the maximum is strongly dependent on the counter ion in the Nafion sample and the water content. In agreement with earlier work [176], the additional mechanism was attributed to the  $\alpha$ -process which yields a  $T_{1\rho}$  minimum above 100 °C, that is further related to the glass transition.

The motional mechanism which is responsible for  $T_{1\rho}$  relaxation at temperatures below the curve maximum is attributed to the aforementioned rotation and reorientational motions of the backbone and the side chain segments, which at room temperature and above occur in the fast motional limit, i.e., at frequencies  $\geq 100$  kHz [177]. In fact, a further variable temperature  $T_{1\rho}$  study showed a low-temperature  $T_{1\rho}$  minimum at around -20 °C, at which the frequency of the underlying motional process should be 40 kHz (= strength of experimental spin-lock field in the experiment) [177].

Accordingly, the aforementioned decrease of the  $T_{1\rho}$  values towards the side chain ends reflects an increase of the motional amplitude, due to higher chain flexibility, in the same direction. The slight increase of the  $T_{1\rho}$  values for the sample without Pt coating after the degradation test is again attributed to a decrease of the motional amplitude and/or reduction of the dipolar interactions due to structural annealing, as mentioned during the discussion of the  $T_1$  data. Upon Pt coating a much more pronounced increase of the  $T_{1\rho}$  values after the chemical degradation test is registered which is in line with the aforementioned reduction of the motional amplitude.

In summary, the same motional modes are assumed to be responsible for  $T_{1\rho}$  and  $T_1$  relaxation. The stronger rise of the relaxation data for the Pt coated sample after the degradation test may originate from chemical and thus structural changes of the Nafion membrane. In this context, chain cross-linking, as a result of the degradation process, may take place, which directly reduces the motional amplitudes and hence the chain flexibility.

## 5.5. Conclusion

Chemical degradation of Nafion membranes has been studied by treatments in an ex-situ set-up and subsequent NMR analysis of the membranes and the water, which had been in

contact with the membrane during the tests. Temperature and gas composition ( $\text{H}_2\text{O}$ ,  $\text{H}_2$ , and  $\text{O}_2$ ) were controlled and varied independently during the tests, and as samples, membranes with and without Pt catalyst coating were used. In this way, in-situ fuel cell operating conditions could not only be mimicked, the controlled variation of single parameters also allowed for the identification of the parameters controlling chemical aging. Since no current was applied during the aging process, electrochemical reactions could not contribute to the observed effects. But the fact, that in-situ degradation effects were reproduced by the present ex-situ experiments, suggest that membrane degradation in a running fuel cell is mainly the consequence of chemical aging. Post aging solid-state  $^{19}\text{F}$  NMR spectroscopy clearly shows that remarkable degradation only takes place, if the membrane is coated with Pt, and if both gases,  $\text{H}_2$  and  $\text{O}_2$ , are present. This observation points toward the importance of radicals in the degradation process, which, in a running fuel cell (in-situ conditions), may only form in the presence of some gas cross-over allowing  $\text{H}_2$  and  $\text{O}_2$  to react at the Pt catalyst of the anode or cathode structure.

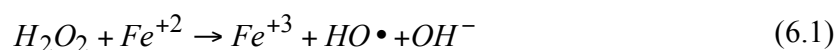
Solid-state NMR of the membrane before and after aging also shows that side chain degradation is prevailing. Side chain fragments are actually identified in the collected water. But this also contains significant amounts of fluoride ions, which may, to some extent, originate from backbone degradation.

Solid-state  $^{19}\text{F}$  relaxation and NMR lineshape data were analyzed to get further insights into the dynamic properties of the Nafion membranes along with the alterations upon degradation. The temperature dependent decrease in NMR linewidths and spectral anisotropies points to a reduction of the static disorder in the Nafion membrane upon sample heating. The relaxation data give evidence for structural annealing, as expressed by a reduction of the motional amplitudes and/or modulated dipolar interactions, and which is not related to chemical degradation. Chemical degradation amplifies this effect, which may result from chain cross-linking.

## 6. Fenton Degradation Tests

### 6.1. Introduction

In 1894, Fenton reported that the combination of  $H_2O_2$  and a Ferrous salt, “Fenton’s reagent”, is an effective oxidant for a wide variety of organic substrates [178]. The produced  $HO\cdot$  and  $HOO\cdot$  radicals in a Fenton reaction can therefore be a source for radicals to attack the polymer chains in PFSA ionomers.



Although the situation in a Fenton test is simulating neither the cathode nor the anode side of the cell, the stability of the polymers against the Fenton’s reagent is taken as one of the basic tests to evaluate the durability of polymer electrolyte membranes [29,30,60,70,71,100,168,172]. The presence of a metallic catalyst and high concentration of hydrogen peroxide provides very drastic conditions, upon which the membranes become very rigid in a short time; a situation which is very different from that in an operating fuel cell. Nevertheless, the Fenton test is considered as a very fast and easy evaluation test that can be applied to any kind of membrane. It provides radicals that can attack the polymer in a similar way as expected to happen in a fuel cell under operation. As a primary test prior to real fuel cell tests, the Fenton ex-situ test is very practical, and the membranes that can

survive the Fenton test with less degradation, typically also show better stability during an in-situ fuel cell test.

In this chapter the optimization for a Fenton degradation test and the effect of extra metallic impurities on the line broadening of NMR spectra is discussed. Based on the optimized condition, the effect of degradation on the polymer structure of short and long side chain perfluorinated polymers are examined and the degradation rate of these two polymers are compared.

## **6.2. Experimental**

### **6.2.1. Sample preparation and Fenton test**

The tests were done on Nafion and Hyflon Ion membranes. The relevant material parameters and the procedure for the membrane pre-treating were mentioned in chapter 4. PFSA ionomers are normally floating on the water surface or Fenton solution, and therefore the samples do not possess a homogeneous surface after the test, but are deformed and rolled. This is a serious problem for any evaluating measurement because the different parts of the membrane do not exhibit the same rate of degradation, and a repetition of the evaluation test on the same material may provide different results. In order to overcome this problem, the membrane should be kept completely inside the Fenton solution and not float on the surface of the solution. Also it should be kept flat and should not roll during the experiment. In order to have a reliable catalyst concentration in a Fenton reaction, any metallic accessories should be avoided.

In this work, a glass frame has been used to keep the membrane inside the solution (Figure 6.1.a). The membrane was laid on a glass frame with some holes in the corners. The same holes were made on the membrane in the proper places. A small glass nail was passing through each hole. A long glass nail was then passing through the holes of the small nails in each row which keeps the small nails in their places. In this way, the membrane was fixed loosely between the frame and the small nails, and does not roll or move to the surface of solution.

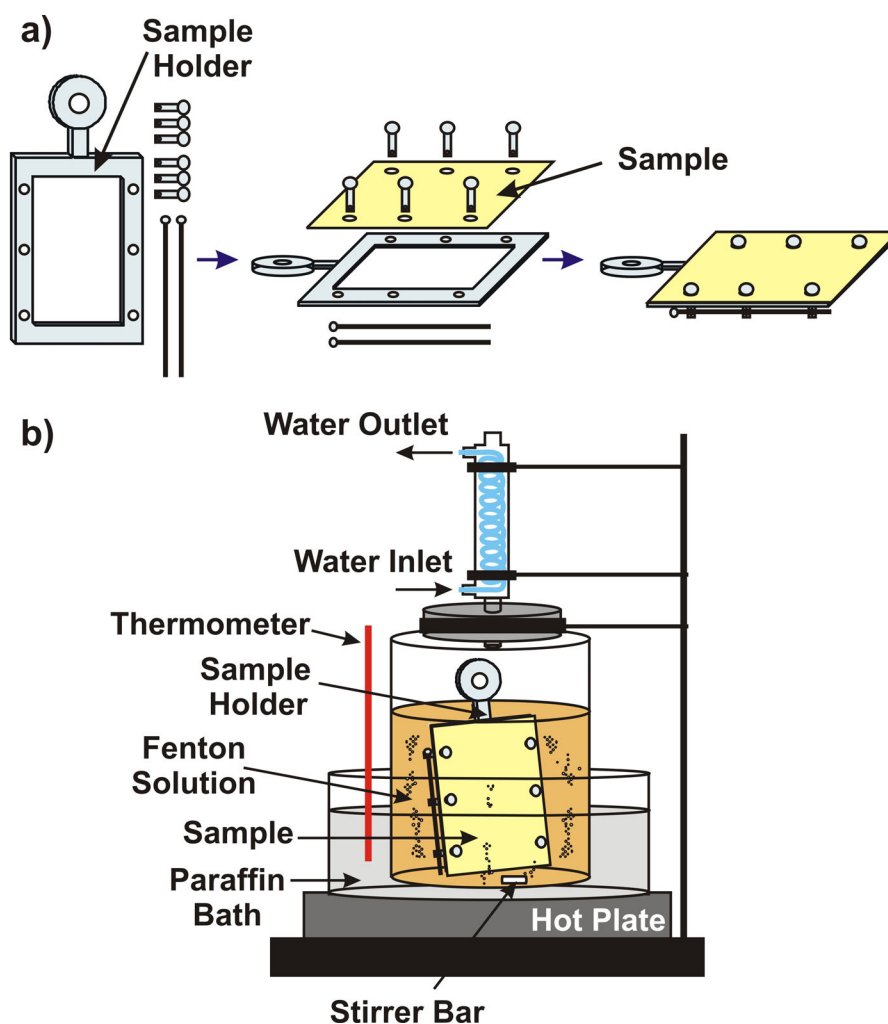


**Figure 6.1.** Ex-situ degradation Fenton test. a) Putting the membrane in the glass frame. b) Set-up of Fenton test cell.

A very easy setup for the Fenton reaction is shown in Figure (6.1.b). For each test, a certain amount of  $\text{FeCl}_2 \cdot 6\text{H}_2\text{O}$  was measured and added to a completely dry dish (Table 6.1). The glass frame with the sample was placed in the dish. In the last step a certain amount of  $\text{H}_2\text{O}_2$  (30 v/v%) was added to the dish and the top of the dish was closed. This dish was placed in a paraffin bath at  $80^\circ\text{C}$ . A distillation column was connected to the top of the dish. Table 6.1 summarizes the conditions for each test. After the tests, the membranes were washed in distilled water for 1 hour and dried at  $110^\circ\text{C}$  overnight in a vacuum oven and prepared for the solid-state NMR and ATR-IR measurements. The remaining Fenton's solution was used for the liquid-state NMR measurements. The latter solution was kept at

room temperature under a slow N<sub>2</sub> gas flow for about 2 days. During this time, water evaporated and the total amount of the solution decreased to about 10 ml which was then used for the liquid-state <sup>19</sup>F NMR experiments.

**Table 6.1.** Fenton test condition in different experiment.

Sample	Test Duration	FeCl <sub>2</sub> concentration in H <sub>2</sub> O <sub>2</sub> 30 v/v % (Molar)	Results
<b>Nafion 117</b> (thickness:0.007 inch)	0	0.1	Figure 6.2
	3 hours		
	6 hours		
	12 hours		
	1 day		
	2 days		
<b>Nafion 117</b>	0	0.001	Figure 6.3
	0.0002		
	0.0005		
	0.01		
	0.05		
	0.1		
<b>Nafion 117</b>	0	0.0002	Figure 6.4, 6.5
	1 hours		
	3 hours		
	6 hours		
	12 hours		
	1 day		
<b>Nafion 112</b> (thickness:0.002 inch) & <b>Hyflon Ion E87</b> (thickness: 0.00078 inch)	0	0.0002	Figure 6.6, 6.7, 6.8, 6.9
	6 hours		
	12 hours		
	18 hours		
	1 day		

### 6.2.2. NMR Spectroscopy

Solid-state NMR spectra were acquired for <sup>19</sup>F nuclei at a spinning rate of 15 kHz, with the same specifications mentioned in chapter 4.

Liquid-state  $^{19}\text{F}$  NMR spectra of the remaining Fenton's solutions were recorded using the same MAS probe with the same parameters, however without spinning the sample. In all measurements 1024 transients were recorded and averaged. Fluoride emission was calculated from the solution NMR spectra by calibrating the signal intensity by a potassium fluoride solution of known concentration and with the known amount of polymer which was subjected to the respective Fenton test.

### 6.2.3. ATR-FTIR Spectroscopy

Attenuated Total Reflection Infrared (ATR-IR) spectra (Appendix A) were measured with a Bruker IFS 66 spectrometer using a single reflection diamond ATR accessory. Spectra were recorded with a DTGS detector at a resolution of  $2\text{ cm}^{-1}$ . The membranes were squeezed between the surface of a diamond crystal and by pressing a counterpart device in order to achieve a good contact. For all measurements 250 scans were averaged covering a spectral range of 400 to  $4000\text{ cm}^{-1}$ .

## 6.3. Results

The assignment for the  $^{19}\text{F}$  MAS NMR of Nafion and Hyflon Ion was shown previously in chapter 4. It is again summarized in Table 6.2.

**Table 6.2.** Chemical shift values (in ppm) and assignment of the  $^{13}\text{C}$  and  $^{19}\text{F}$  resonances in Nafion and Hyflon Ion membranes

		CF (side chain)	CF (main chain)	$(\text{CF}_2)_n$	$\text{SCF}_2$	$\text{OCF}_2$	$\text{CF}_3$
$^{19}\text{F}$	Nafion	-144	-138	-121	-117	-80.1 79.9	-80
	Hyflon Ion	—	-138	-121	-117	-80	—

To examine the degradation of these membranes with the Fenton test, in a first attempt Nafion 117 was treated with a  $0.1\text{ M Fe}^{2+}$ , as also done in the aforementioned Fenton ex-situ study [40]. Figure 6.2 shows the respective solid-state  $^{19}\text{F}$  NMR spectra of these

samples after exposure to the Fenton test (with 0.1 M  $\text{Fe}^{2+}$ ) for the periods given in the figure.

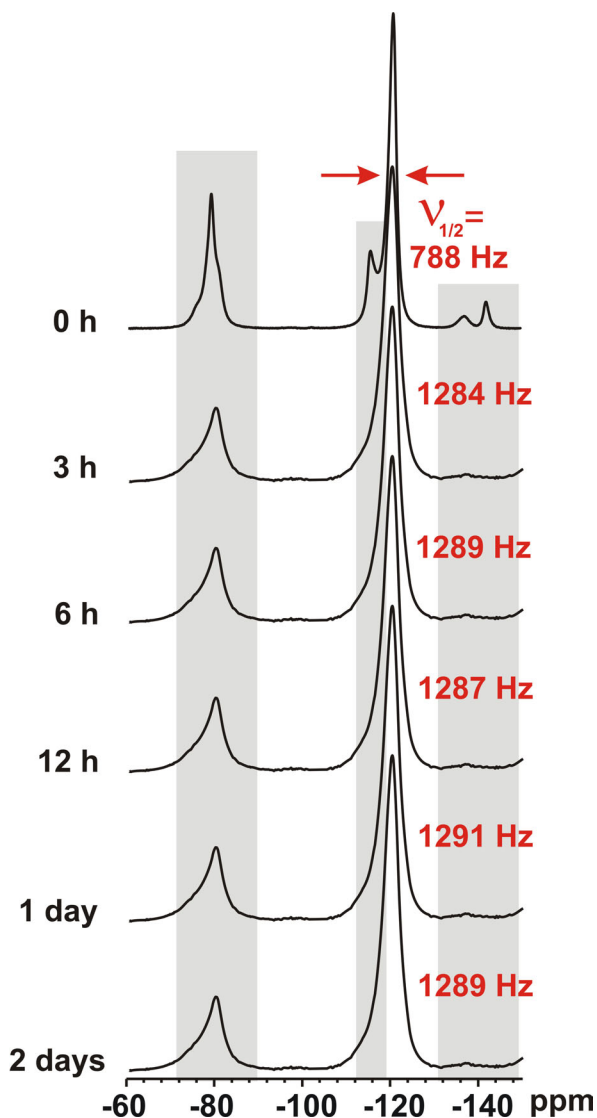


**Figure 6.2.** Solid-state  $^{19}\text{F}$  NMR spectra of Nafion 117 samples after treatment with 0.1 M  $\text{Fe}^{2+}$  in 30 v/v%  $\text{H}_2\text{O}_2$ . The linewidth of the peak ( $\nu_{1/2}$ ) at -121 ppm, referring to the backbone  $\text{CF}_2$  groups, is shown (exposure times are given in the figure).

A general line broadening was observed for all samples after treatment with Fenton's solution. In agreement with the former publication, the spectra of the samples referring to different exposure times are practically identical and are characterized by a substantial line broadening by almost a factor of two, if compared to the untreated sample (see top

spectrum). Hence, it appears very likely that the distinct spectral broadening obscures all other spectral alterations which might occur as a result of this ex-situ test.

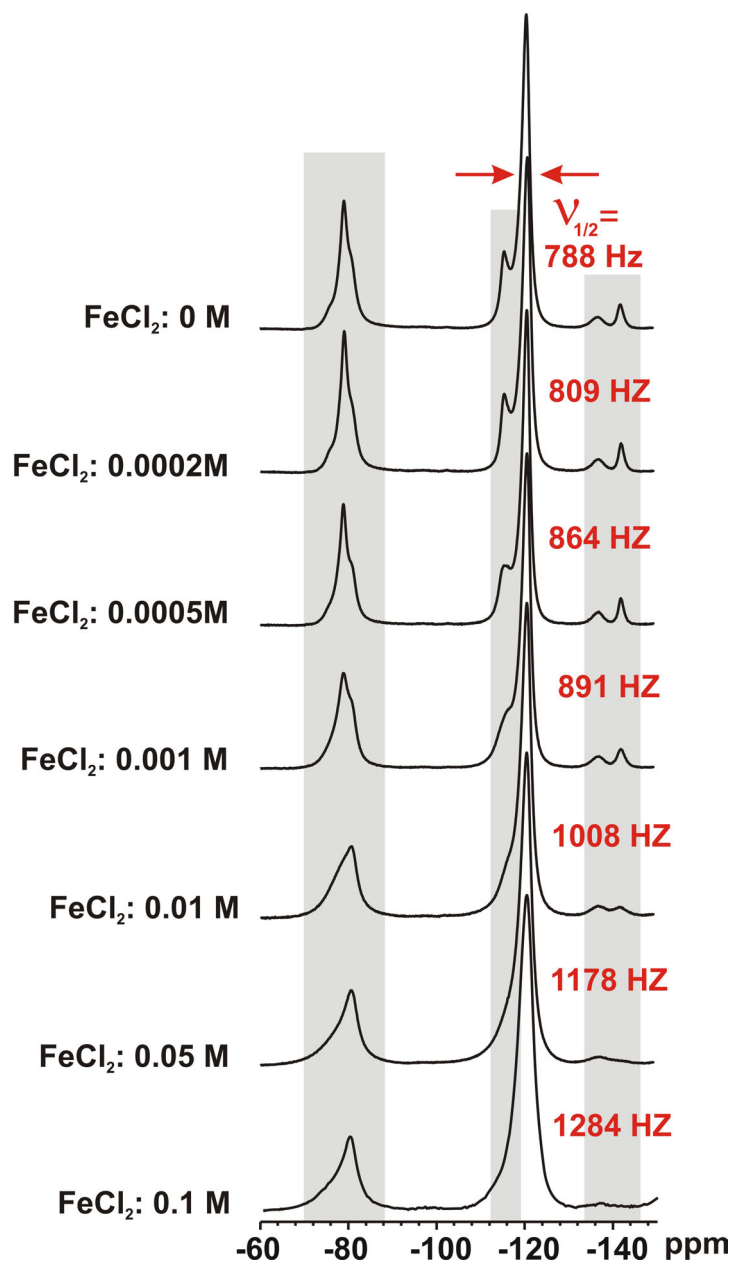


**Figure 6.3.** Solid-state  $^{19}\text{F}$  NMR spectra of Nafion 117 samples after 3 hours ex-situ Fenton test with different  $\text{Fe}^{2+}$  concentration in 30 v/v%  $\text{H}_2\text{O}_2$  solutions. The linewidth of the peak ( $\nu_{1/2}$ ) related to the backbone  $\text{CF}_2$  groups is shown.

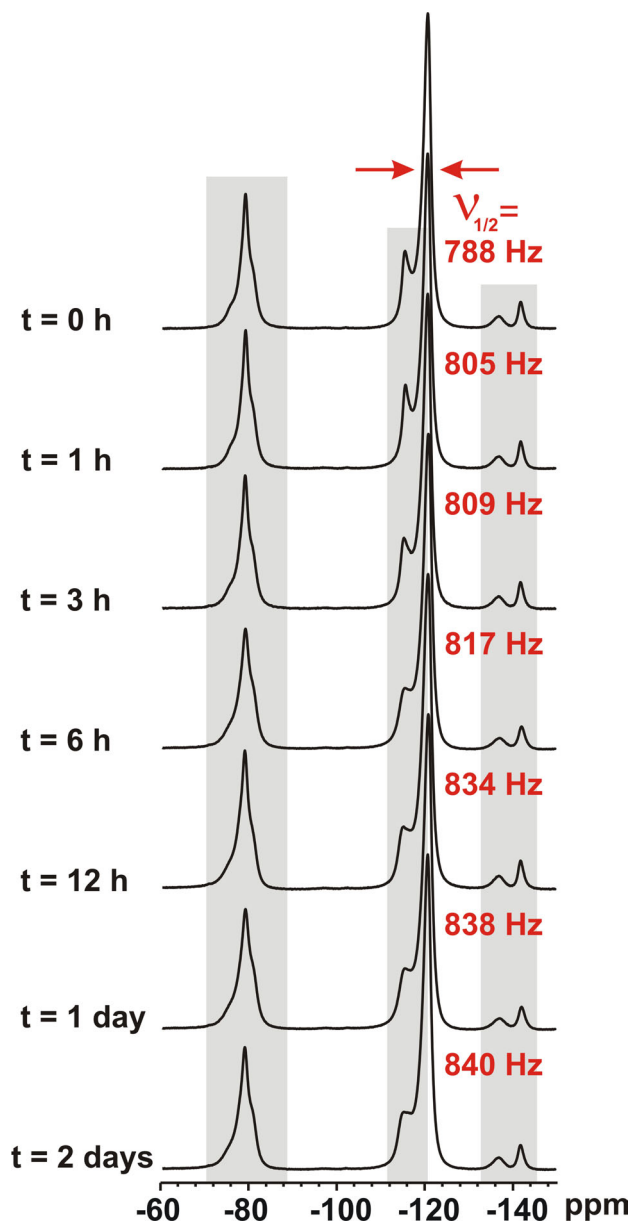


**Figure 6.4.** Solid-state  $^{19}\text{F}$  NMR for Nafion 117 samples after ex-situ Fenton tests with 0.0002 M of  $\text{Fe}^{2+}$  in 30 v/v% of  $\text{H}_2\text{O}_2$ .

To further clarify these findings, the test was repeated with different concentrations for the Fenton's reagent. Figure 6.3 displays  $^{19}\text{F}$  NMR spectra of Nafion 117 samples which were exposed for 3 hours to Fenton's reagent with the  $\text{Fe}^{2+}$  concentrations given in the figure. It is seen that the linewidths strongly vary with the actual concentration. As an example, the linewidth of the main chain  $\text{CF}_2$  group,  $\nu_{1/2}$ , is shown in the Figure. The difference in

spectral linewidth for the samples treated with 0.0002 M and 0.1 M  $\text{Fe}^{2+}$  is almost 500 Hz. Due to the line broadening, for  $\text{Fe}^{2+}$  concentrations  $> 0.0005$  M the  $\text{SCF}_2$  group signal only appears as a shoulder next to the dominant  $\text{CF}_2$  peak, and at the highest concentrations it is obscured completely. A similar broadening effect is seen for all other resonances. However, independent of the spectral broadening, a decrease of the relative intensity for the side chain  $\text{SCF}_2$  group can be identified for the lower concentrated solutions ( $< 0.1$  M).

In order to follow the time evolution of the spectra during the ex-situ Fenton test, a  $\text{Fe}^{2+}$  concentration of 0.0002 M has been chosen. The respective  $^{19}\text{F}$  NMR spectra are given in Figure 6.4. It is seen that the linewidth of the main chain  $\text{CF}_2$  peak, as given in the figure, slightly increases by about 50 Hz, if the non-treated membrane is compared to the membrane which is treated in the Fenton's solution for 2 days. At the same time, a continuous decrease (with exposure time) of the  $\text{SCF}_2$  group intensity can be clearly identified.

The structural evolution of the Nafion 117 sample during the Fenton test was also studied by ATR-FTIR spectroscopy. The respective IR spectra of the same Nafion samples are shown in Figure 6.5. The major peaks in these ATR-FTIR spectra and their assignment [88] are also listed. The comparison of the spectra before and after the Fenton degradation test shows a general decrease in the intensity of the C-O-C (at 960 and 980  $\text{cm}^{-1}$ ), S-C (at 805  $\text{cm}^{-1}$ ) and S-O (at 1056  $\text{cm}^{-1}$ ) stretching modes. At the same time, an intensity decrease is detected for the peaks at 1132 and 1196  $\text{cm}^{-1}$  which are related to the stretching modes of the  $\text{CF}_2$  groups.

A further, very interesting result is the appearance of two new peaks at around 2850 and 2920  $\text{cm}^{-1}$  which are attributed to symmetric and antisymmetric CH stretching modes, and whose intensities increase with increasing exposure time. It is worthwhile to note that attempts were made to detect such a CH group formation also by solid-state  $^1\text{H}$  NMR spectroscopy. These experiments, however, failed, most probably due to the low concentration of the formed CH segments.

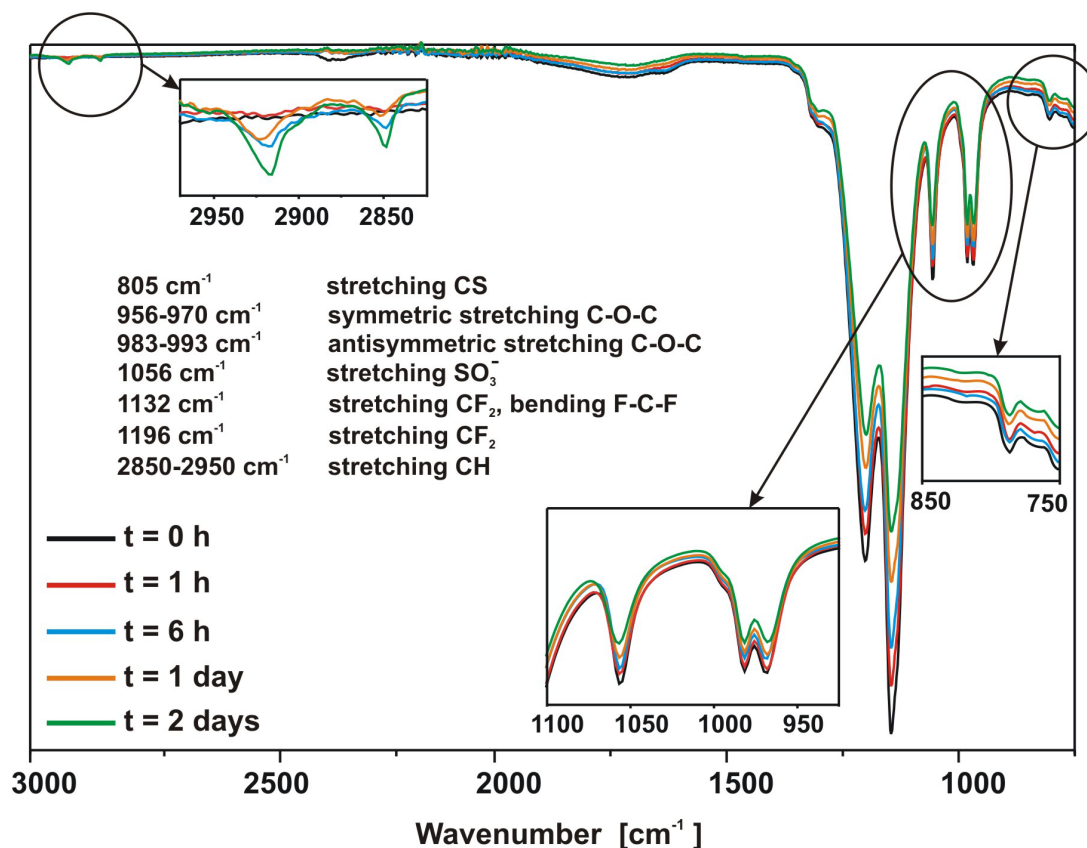


**Figure 6.5.** ATR-IR spectra for Nafion 117 samples after ex-situ Fenton tests with 0.0002 M of  $\text{Fe}^{2+}$  in 30 v/v% of  $\text{H}_2\text{O}_2$ .

To compare the stability of Nafion and Hyflon Ion membranes, samples of these ionomers were subjected to the same Fenton test solution, with a  $\text{Fe}^{2+}$  concentration of 0.0002 M, for 12 hours. Since the thickness of Hyflon Ion is much less than that of Nafion 117, this test was done with the thinner Nafion 112 membrane. The respective spectra for these membranes before and after the test are shown in Figure 6.6. It is seen that the Hyflon Ion side chain is also sensitive to radical attack during the Fenton test. The relative stability of the two fuel cell membranes can be identified by the graphs given in Figure 6.7. Here, the relative peak integrals of the resolvable signals (from deconvolution of the  $^{19}\text{F}$  NMR spectra; each signal was first normalized to the  $\text{CF}_2$  signal of the main chain; and the intensity for the signal prior to the test were put to 100 as reference for the samples after the test) are plotted prior and after the Fenton test.

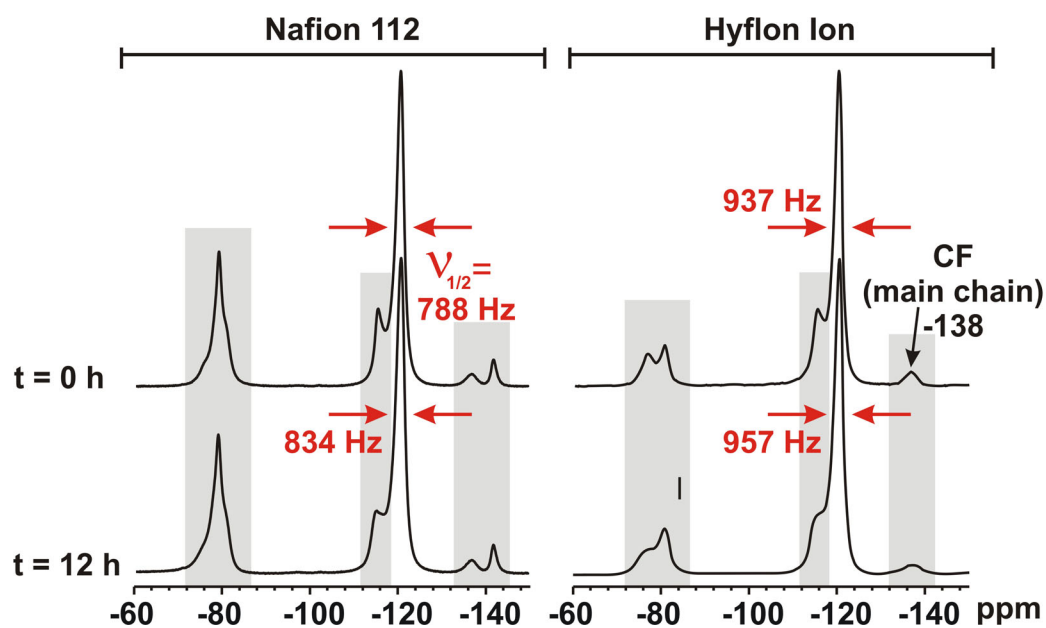


**Figure 6.6.** Solid-state  $^{19}\text{F}$  NMR spectra of Nafion 112 and Hyflon Ion after 12 hours ex-situ Fenton tests with  $0.0002\text{ M Fe}^{2+}$  in  $30\text{ v/v}\%$   $\text{H}_2\text{O}_2$ .

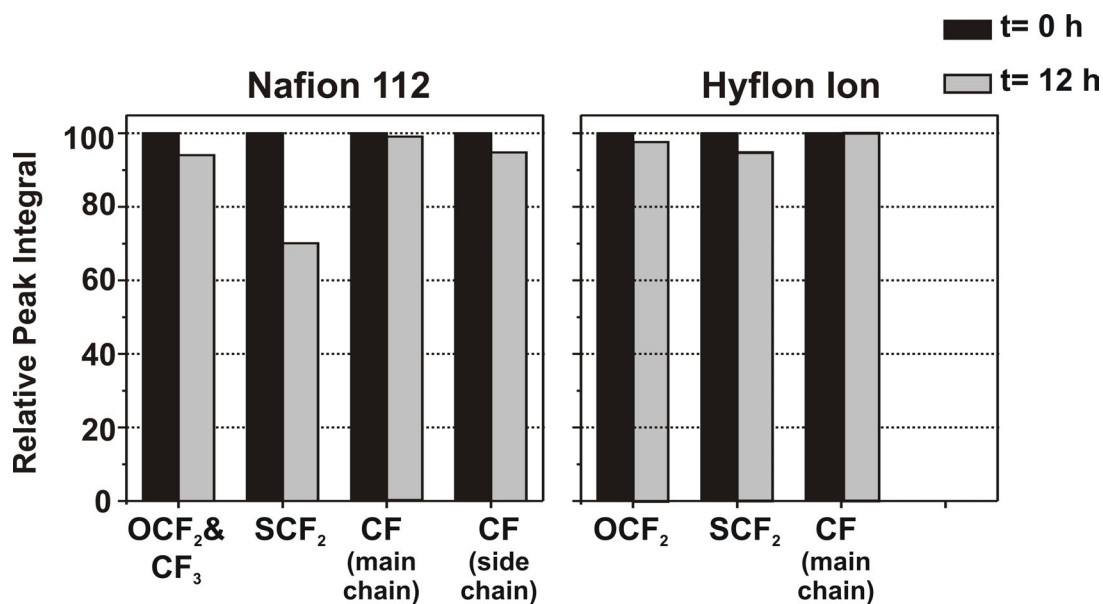


**Figure 6.7.** Relative peak area after 12 hours ex-situ Fenton tests with  $0.0002\text{ M Fe}^{2+}$  in  $30\text{ v/v}\%$   $\text{H}_2\text{O}_2$  of Nafion 112 and Hyflon Ion membranes. The given numbers are the ratios of the peak area after the ex-situ tests relative to the original intensities prior to the tests in percentage, as taken from the  $^{19}\text{F}$  NMR spectra.

Inspection of Figure 6.7 clearly reveals that degradation in the Hyflon Ion is much less pronounced than in Nafion 112. Moreover, for both membranes the main chain CF group signal is only little affected, and the biggest signal loss is detected for the SCF<sub>2</sub> signal. In general, the data imply a gradient for side chain degradation, i.e. degradation continuously increases towards the chain end with the CF<sub>2</sub>SO<sub>3</sub>H group.

As a crosscheck, liquid-state <sup>19</sup>F NMR measurements were done on the Fenton solution during the latter tests. In fact, <sup>19</sup>F NMR signals can be clearly detected after treatment of the membranes in the Fenton's solution. As an example, Figure 6.8 presents the <sup>19</sup>F NMR spectrum of the Fenton solution after 12 hours treatment of Nafion 112 which is compared with the blind test carried out with the fresh Fenton solution, before any membrane treatment. The signal-to-noise ratio is very poor since the <sup>19</sup>F NMR spectra were recorded with the MAS probe and without any special precautions for high-resolution conditions. Another reason for the poor signal-to-noise ratio might be the presence of paramagnetic ions in the solution. The peak in the spectrum at -127.6 ppm is attributed to the F<sup>-</sup> signal, in agreement with the literature [64].

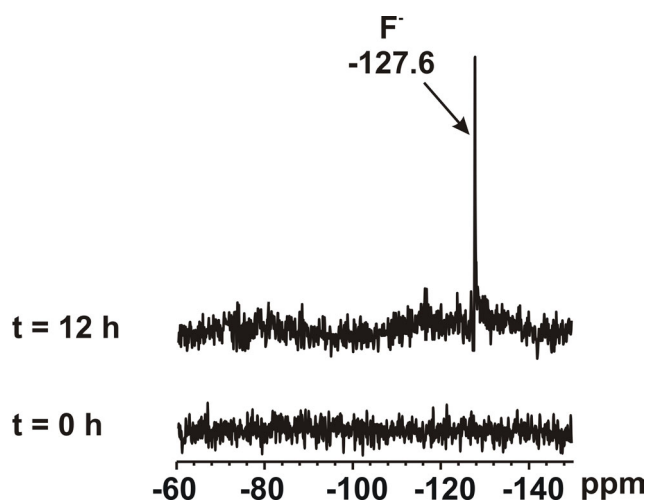


**Figure 6.8.** Liquid-state <sup>19</sup>F NMR spectrum for the Fenton solution after the test of Nafion 112 for 12 hours. The result of a blind test carried out with fresh Fenton solution is given for comparison (0 h).

The peak intensity from the solution <sup>19</sup>F NMR measurements were further used to calculate the fluoride emission during these Fenton tests (see experimental). The results for the

Nafion 112 and Hyflon Ion membranes are plotted in Figure 6.9. The derived results are comparable with the reported fluoride emission from Fenton solution tests in other works [70,71]. In the present case, the fluoride emission for Hyflon Ion is slightly less as compared to Nafion 112, in qualitative agreement with the solid-state  $^{19}\text{F}$  NMR data (see Figure 6.7).

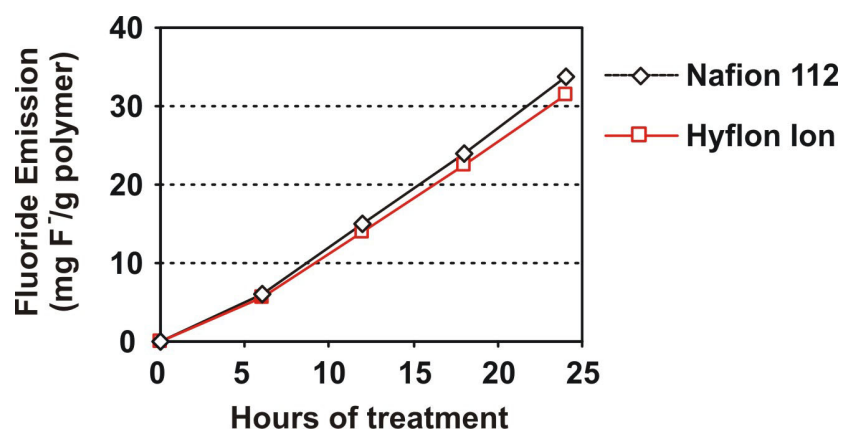


**Figure 6.9.** Fluoride emission for Nafion 112 and Hyflon membranes after ex-situ Fenton tests with 0.0002 M  $\text{Fe}^{2+}$  in 30 v/v%  $\text{H}_2\text{O}_2$ .

## 6.4. Discussion

In chapter 4, solid-state NMR spectroscopy was successfully applied for the characterization of polymer membranes which have been subjected to in-situ tests. These studies clearly proved that substantial degradation also takes place in the polymer side chains. The results from the present ex-situ Fenton test studies confirm these former results, and demonstrate that membrane degradation not only involves the polymer main chain. Rather structural changes and bond cleavages also take place in the polymer side chains, and provide an important contribution to polymer degradation.

It is found that the membranes, treated with Fenton's solution at  $\text{Fe}^{2+}$  concentrations larger than 0.0005 M, exhibit substantial line broadening in the solid-state  $^{19}\text{F}$  NMR spectra. This spectral broadening is visible for all  $^{19}\text{F}$  resonances, but is somewhat more pronounced in the side chain region of the polymers. In fact, a similar line broadening effect was also observed after soaking the membrane just in a  $\text{FeCl}_2$ /water solution which implies that the

spectral changes are not simply related to membrane degradation, but to the presence of the paramagnetic iron. The presence of iron not only affects the solid-state NMR data, but is also visible during other experimental studies. Hence, ferrous ions can easily exchange with the acidic proton in the membrane, and - without any chemical degradation or bond cleavage in the membrane - decrease the ion exchange capacity and electric conductivity. Normally these changes are reversible after treating the membrane with an acidic solution.

Performing the Fenton test with the lowest manageable concentration of  $\text{FeCl}_2 \cdot 6\text{H}_2\text{O}$  (a molar concentration of 0.0002 M corresponds to a mole fraction of 10 ppm) yields experimental  $^{19}\text{F}$  NMR spectra with acceptable resolution. Their analysis shows continuous degradation in the side chain region with increasing reaction time. Side chain degradation is independently confirmed by the ATR-FTIR spectra which also – along with the detection of the strong  $\text{F}^-$  peak in the liquid NMR spectra - give evidence for main chain degradation, and which directly cannot be seen in the solid-state  $^{19}\text{F}$  NMR spectra. Based on these results and in agreement with other works, the possible points for radical attack in PFSA membranes are both the main and the side chain of the polymers.

The comparative studies on the stability of Nafion and Hyflon Ion membranes in the Fenton test show that the side chains of the latter one are also sensitive to radical attacks, but much less than Nafion. In general, the polymer side chains can be attacked via the C-S bond or via the tertiary carbons in the side and main chain [30,56,65,173].

The comparison of the CF peak intensities for the side chain and main chain of Nafion after the degradation shows that the changes for the main chain CF group is very small, while the side chain CF group signal shows a much stronger intensity decrease. Therefore, for Nafion the intensity reduction for the peak at -80 ppm (referring to the  $\text{OCF}_2$  and  $\text{CF}_3$  groups) is primarily related to intensity changes of the  $\text{OCF}_2$  peak closer to the end of the side chain and of the  $\text{CF}_3$  group than of the  $\text{OCF}_2$  group closer to the polymer main chain.

These NMR data confirm the generally accepted and aforementioned positions for radical attacks for side chain degradation at the S-C bond and the C-F bond in tertiary carbons. Obviously, the C-F bond in the main chain is more stable than the C-F at the tertiary carbon in the inner part of the Nafion side chain. The absence of this latter segment can directly

explain the substantially improved side chain stability of the Hyflon Ion. Accordingly, for Nafion the more pronounced signal decrease of the SCF<sub>2</sub> unit can be traced back to both an attack at the tertiary carbon within the side chain and at the C-S bond.

The liquid-state NMR spectra of the Fenton solution exhibit a poor signal-to-noise ratio due to the presence of iron ions, the small peaks arising from the side chain fragments are not visible, as reported in chapter 5. The only visible signal at -127.6 ppm reflects the release of a substantial amount of F<sup>-</sup> ions. Surprisingly, the present liquid-state NMR data show a very similar fluoride emission – and thus degradation – for the Nafion and the Hyflon Ion, and the derived values are comparable with the fluoride emission data reported from ion selective electrode measurements [70,71]. At first sight, they seem to contradict the solid-state NMR results with minor side chain degradation for Hyflon Ion. However, the liquid-state NMR data represent the total amount of fluoride release during the Fenton test due to both main and side chain degradation. The reason for these contradictory results from the solid-state and liquid-state NMR experiments is probably the higher main chain degradation rate in Hyflon Ion E87 as compared to Nafion 112 which proceeds from carboxyl groups terminating the PTFE backbone [172]. In the commercial Nafion 112, the number of carboxyl groups is minimized by capping the end of the main chain with CF<sub>3</sub> groups. In Hyflon Ion E87, the endcapping is not done. Merlo et. al. showed that the fluoride emission of Hyflon Ion E87 after endcapping decreases by a factor of 5 [70,71].

It can be therefore concluded that for stabilized perfluorosulfonic acid polymers the total degradation rate is determined primarily by the degradation rate of the side chain. As shown in the present work, the polymer with shorter side chains (Hyflon Ion) exhibits higher stability and less degradation in comparison with the polymer having longer side chains (Nafion). This may also explain the better performance of short side chain membranes in the fuel cell devices.

## 6.5. Conclusions

Solid-state NMR spectroscopy was successfully used for the study of the structural changes within perfluorosulfonic acid membranes after ex-situ Fenton tests. It was shown that great care should be taken during the study of such Fenton tests, since the presence of

paramagnetic iron ions can strongly affect the results. After optimization of the procedure and working with a minimum  $\text{Fe}^{2+}$  concentration, it was possible to follow the structural changes due to membrane degradation initialized by the Fenton's reagent. The results from liquid-state and solid-state  $^{19}\text{F}$  NMR as well as ATR-FTIR measurements before and after Fenton tests demonstrate that degradation can take place in the polymer side chain as well as in the polymer main chain.

The comparative study shows that the Nafion and Hyflon Ion membranes exhibit similar total degradation rates. This result is explainable by the more pronounced main chain degradation of the Hyflon Ion membrane since no endcapping was made. However, the shorter side chains in Hyflon Ion are more stable than the longer side chains in Nafion which is attributed to the presence of an additional tertiary carbon in the side chains of latter polymer, and which is relatively sensitive for radical attacks leading to degradation.

On the basis of these results, the membrane stability should be greatly improved by using polymers with short side chains (i.e. without tertiary CF groups) and endcapped main chains, both of which being much less vulnerable by radical attack, the key mechanism of membrane degradation.

## 7. Dynamics in Composite Membranes

### 7.1. Introduction

This chapter focuses on  $^{19}\text{F}$  MAS NMR studies of Nafion/SiO<sub>2</sub> composites. The impact of the SiO<sub>2</sub> particles on the polymer dynamics and their effect on the performance of the polymer electrolyte membrane is discussed. Here we are not concerned about the chemical degradation of composite membranes but their better performance in low water content.

### 7.2. Experimental

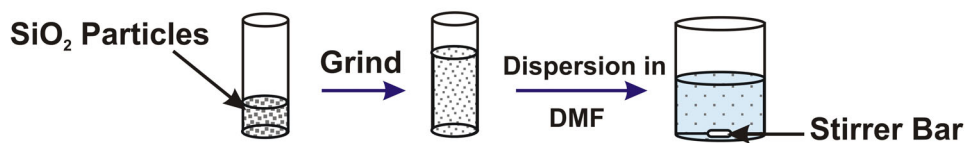
#### 7.2.1. Sample preparation

The sample preparation procedure has been shown in Figure 7.1. Micron-sized SiO<sub>2</sub> particles were milled in a planetary ball mill for 2 h at 500 rpm in order to decrease the particle sizes to about 50 nm. Six [Nafion/(SiO<sub>2</sub>)<sub>X</sub>] nano-composite membranes with SiO<sub>2</sub> weight percent, X, ranging from 0 to 15 were prepared by a general solvent casting procedure as follows:

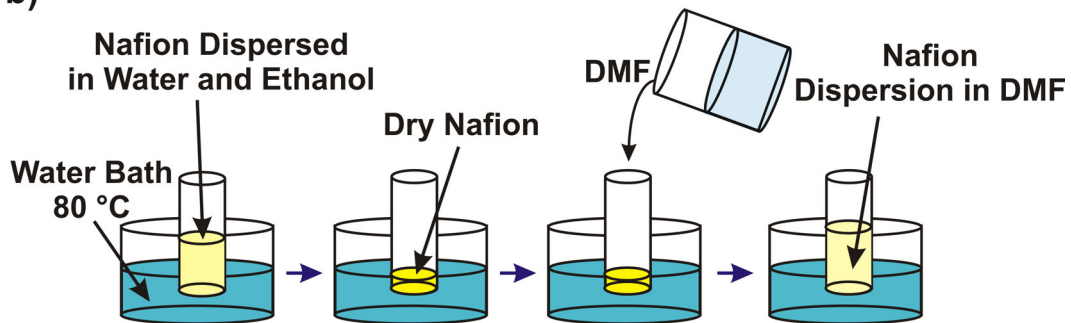
An appropriate amount of Nafion 5 w/w% dispersion in water and ethanol was kept in a water bath at 80 °C in order to remove the solvents. The obtained brittle cast film was dispersed in 20 mL of dimethylformamide (DMF) and mixed with the desired quantity of SiO<sub>2</sub> (see Table 7.1). The resulting mixture was homogenized by treatment in an ultrasonic bath for 2 h. The obtained homogeneous solution was recast in a Petri dish at 100 °C for 4 h

under a flow of hot air. The resulting composite Nafion film was separated from the Petri dish in a bath with milli-Q water heated to  $T = 80^\circ\text{C}$ . The membrane was then hot pressed at 1000 psi for 5 min to improve its mechanical properties. The thickness of the prepared membranes was found to be in the range of 150 to 300  $\mu\text{m}$ . The membrane was then activated and purified with the pretreatment procedure described in chapter 4.

a)



b)



c)

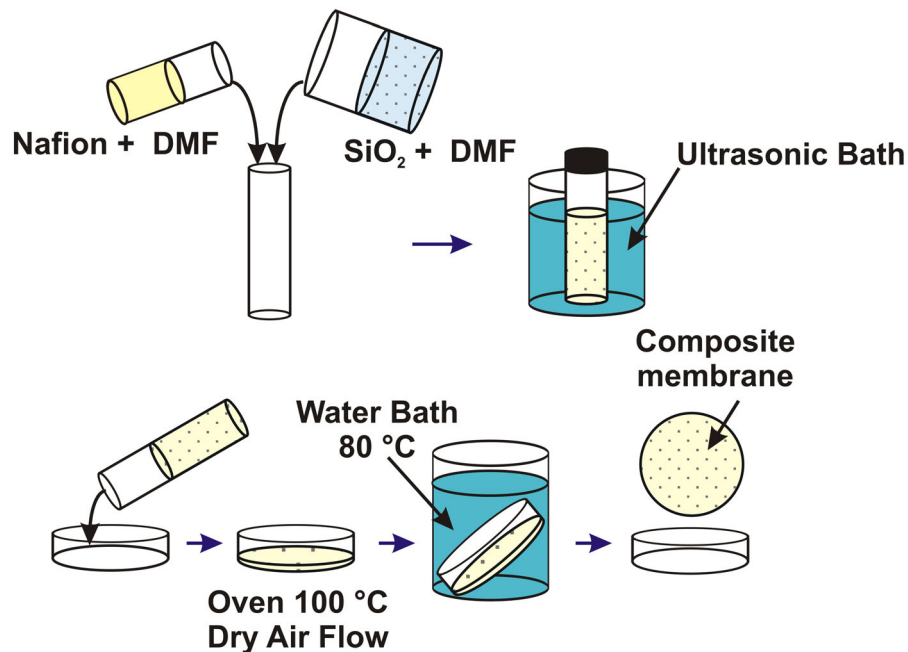


**Figure 7.1.** Composite membrane preparation: a) preparation of  $\text{SiO}_2$  particles, b) preparing Nafion solution, c) casting the composite membrane.

**Table 7.1.** Reagent composition and molar ratios for [Nafion/(SiO<sub>2</sub>)<sub>x</sub>].

Nafion (g)	SiO <sub>2</sub> (g)	X (w/w% SiO <sub>2</sub> )	mol (SiO <sub>2</sub> )/mol (-SO <sub>3</sub> H)
1.35	0	0	0
1.35	0.04175	3.76	0.64
1.35	0.07105	5	1.09
1.35	0.01335	9	2.06
1.35	0.2012	13	3.1
1.35	0.2382	15	3.67

### 7.2.2. NMR Spectroscopy

Variable temperature <sup>19</sup>F solid-state NMR spectra (between 25 and 95 °C) were recorded at spinning rates of 10.5 and 15 kHz with the same specifications as it mentioned in chapter 4 and 5. <sup>19</sup>F {<sup>1</sup>H} CP/MAS spectra were recorded with a <sup>1</sup>H 90° pulse length of 5 μs (at 399.76 MHz for <sup>1</sup>H nuclei), a contact pulse of 1.5 ms and a recycle delay of 2 s without proton decoupling. 1024 transients were recorded for each sample. Prior to Fourier transformation a line broadening of 80 Hz was applied (not used for the normal <sup>19</sup>F NMR spectra). <sup>19</sup>F spin-lattice relaxation times T<sub>1</sub> and T<sub>1ρ</sub> were obtained in the same way as described in chapter 5.

For the NMR measurements two different hydrated states were chosen for each sample. One example was dried at 110 °C in the vacuum oven (1000 mbar) for 12h, and kept inside a desiccator until the NMR measurements were started. The other piece was kept in water at room temperature before the NMR measurements. These samples referred to the dry and wet state for the solid-state NMR investigations, as discussed in the following.

### 7.2.3. Equivalent weight (EW)

The determination of the EW is described in chapter 5.

### 7.3. Results

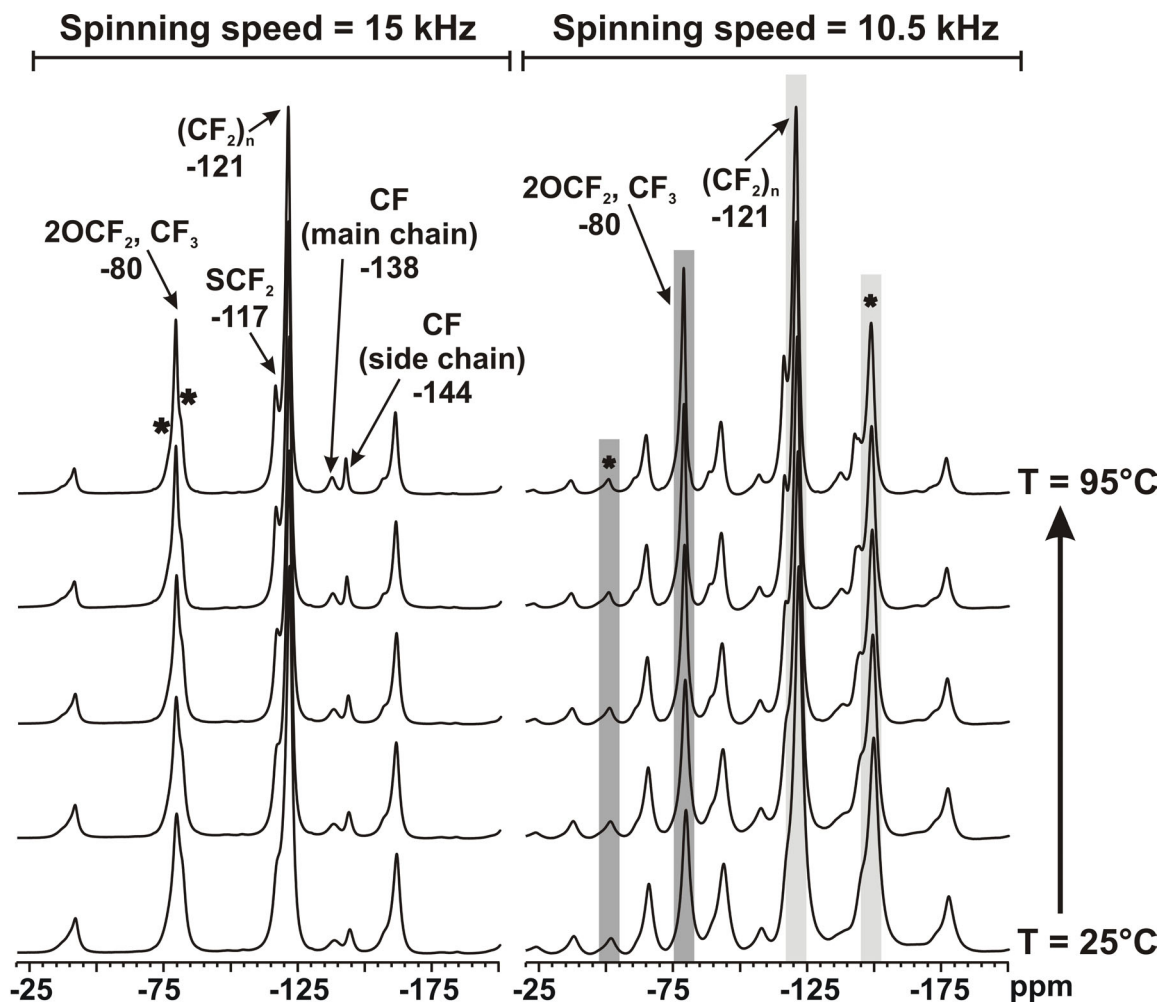


**Figure 7.2.** Solid-state  $^{19}\text{F}$  NMR spectra of Nafion at spinning speeds of 10.5 and 15 kHz at different temperature. Asterisks indicate spinning sidebands used for the data plotted in Figure 7.3 and 7.5. The sidebands and the respective central peaks are shown by the same color.

**$^{19}\text{F}$  MAS NMR.** A series of variable temperature  $^{19}\text{F}$  MAS NMR spectra of Nafion recast at a sample spinning frequency of 10.5 and 15 kHz is shown in Figure 7.2. It is apparent that for the elevated temperatures the linewidths are reduced resulting in an enhanced resolution. The spinning speed of 15 kHz was the upper speed that was reachable safely for this sample in the dry and wet state in the 4 mm MAS probe. As indicated by the asterisks,

at this spinner frequency the low field signal of  $\text{OCF}_2$  and  $\text{CF}_3$  groups are partially overlapped with the spinning sidebands of the backbone  $\text{CF}_2$  group and the side chain  $\text{SCF}_2$  group signals. For this reason, for examination of the NMR linewidths, the sample spinning speed was reduced to 10.5 kHz at which former signals are not affected by spinning sidebands from other resonances. However, the  $^{19}\text{F}$  NMR spectra exhibit more spinning sidebands and larger linewidths which stem from the larger chemical shift anisotropies and strong dipolar couplings of the  $^{19}\text{F}$  nuclei.

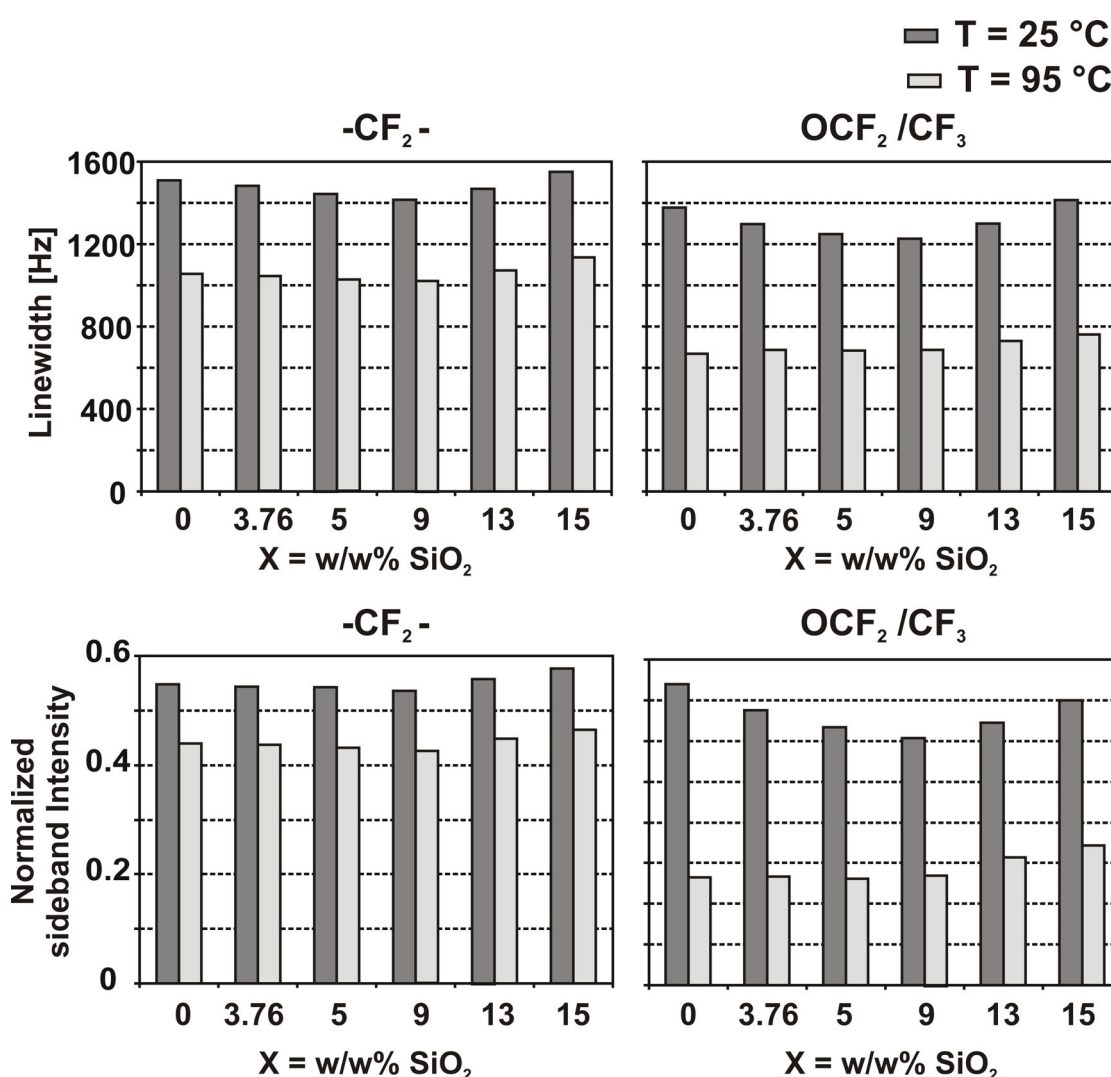


**Figure 7.3.**  $^{19}\text{F}$  NMR linewidths and relative sideband intensities (normalized to the respective central peak) for the polymer backbone and side chain at a sample spinning speed of 10.5 kHz, for  $[\text{Nafion}/(\text{SiO}_2)_X]$  with  $X = 0, 3.76, 5, 9, 13$  and  $15$ .

**Sideband intensity and linewidth analysis.** The  $^{19}\text{F}$  MAS NMR spectra at a spinning speed of 10.5 kHz were analyzed on a semi-quantitative level by considering the linewidths and intensities of the spinning sidebands which can be related to structural and dynamic changes within the various samples. The results, obtained from the analyses of the linewidth for the dry [Nafion/( $\text{SiO}_2$ ) $_X$ ] samples with  $X = 0$  to 15 w/w% are summarized in Figure 7.3.

It can be seen that adding the  $\text{SiO}_2$  particles to the membrane will primarily decrease the linewidth of both the main chain and the side chain of the polymer. The minimum linewidths are observed for the samples with  $X = 9$ . At higher  $\text{SiO}_2$  content, the linewidth increase again. The effect is more obvious for the room temperature measurements but the same trend is also visible at 95 °C.

The same  $^{19}\text{F}$  NMR spectra were used to derive the relative intensities of the spinning sidebands [167] which again provide qualitative information about changes of the underlying chemical anisotropies and dipolar interactions as a function of various experimental parameters. The given sideband intensities were normalized with respect to the intensities of their respective central peaks, and are shown in Figure 7.3 for all samples in the dry state. In agreement with the linewidth changes, upon increase of the content of the  $\text{SiO}_2$  particles, the sideband intensity of both the main chain and the side chain decreases until reaching the lowest values for  $X = 9$ . Beyond this value, the sideband intensity increases again, which implies the highest membrane mobility for  $X = 9$ . It is interesting to note that previous conductivity measurements on the same samples, also showed the highest conductivity for the membrane with  $X = 9$  (Figure 7.4) [88], which may imply a correlation between conductivity and polymer mobility. On the other hand, it should be mentioned that these conductivity measurements were done at 100% RH.

The derived linewidths and relative sideband intensities for the [Nafion/( $\text{SiO}_2$ ) $_X$ ] samples with  $X = 0$  and 9 in the range between  $T = 25$  °C and 95 °C for the dry and wet samples and summarized in Figure 7.5. By increasing the sample temperature the  $^{19}\text{F}$  NMR linewidths decrease continuously, which is true for both the main and the side chain peaks of all samples. Moreover, the NMR linewidths of the side chain signals are less than those of the main chain, which point to an enhanced mobility in the side chains. It is further seen

that by decreasing the water content, the linewidths generally increase for both the side chain and the main chain of the polymer. Addition of  $\text{SiO}_2$  is accompanied by a decrease of the linewidths. These latter changes are bigger for the wet samples.

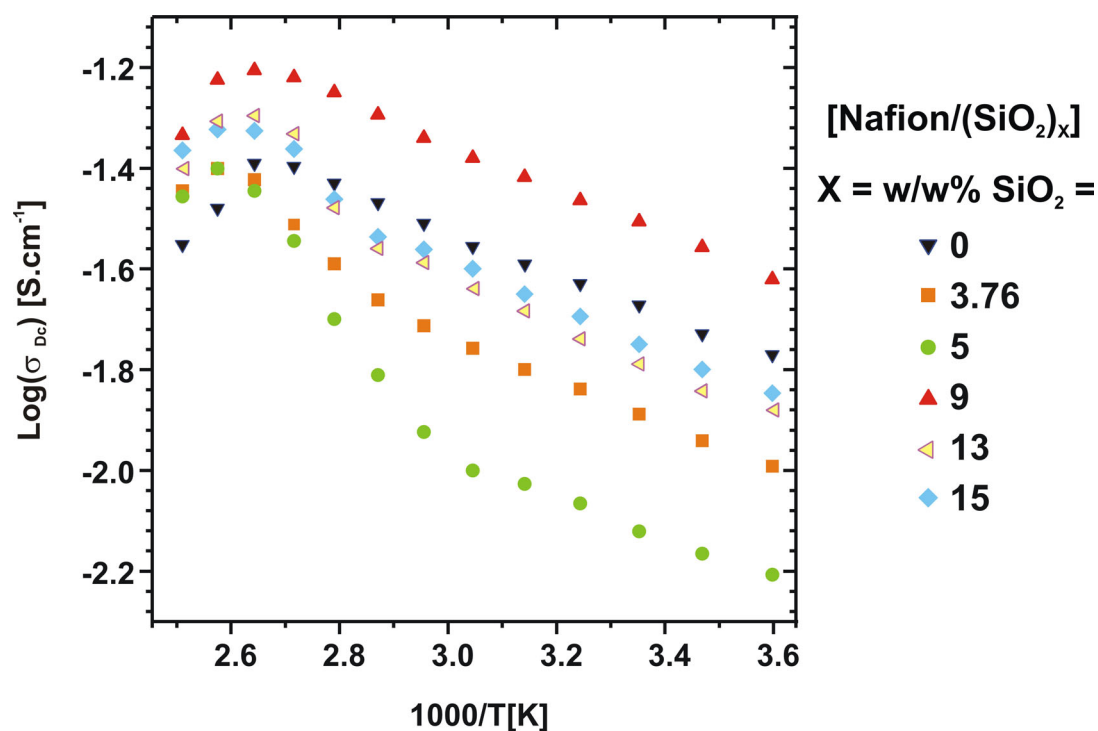


**Figure 7.4.** Temperature dependence of the conductivity for  $[\text{Nafion}/(\text{SiO}_2)_X]$ , with  $X = 0, 3.76, 5, 9, 13$  and  $15$ . [88]

Similar trends are observed for the relative spinning sideband intensities. Hence, for all samples the normalized sideband intensities for both the side and the main chain show a decrease as the sample temperature increases. The relative intensities of the spinning sidebands for the backbone  $\text{CF}_2$  signal are significantly higher than those of the  $\text{OCF}_2/\text{CF}_3$  side chain peaks. This observation can be understood by differences in the averaged chemical shift anisotropy and/or dipolar couplings along with a higher mobility of the side chain segments.

The presence of water decreases the sideband intensities for all samples. Although the differences between the samples with and without  $\text{SiO}_2$  particles are very small, the

presence of particles is found to slightly decrease the sideband intensity due to the higher chain mobility, in agreement with the aforementioned NMR linewidth data.

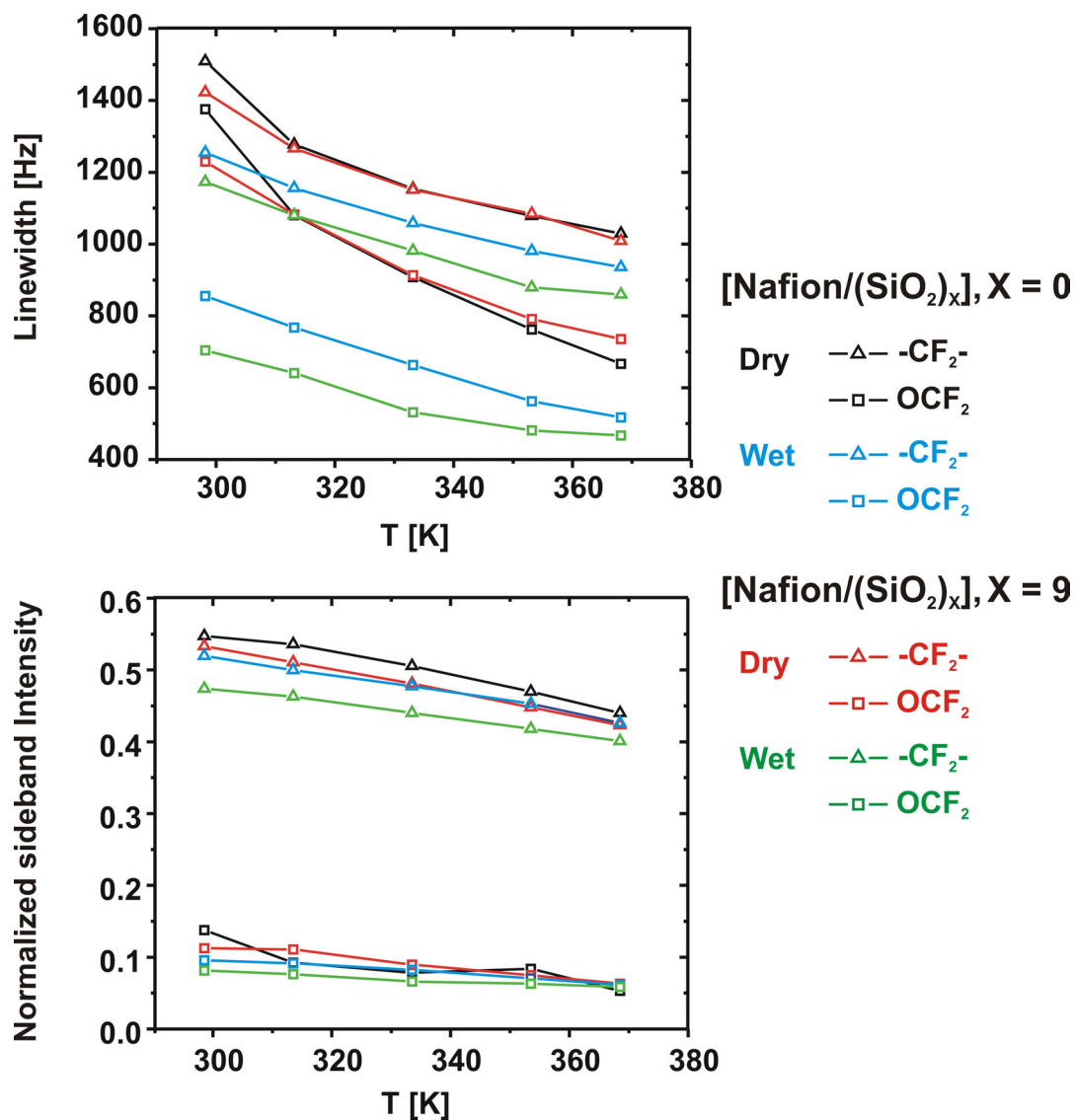


**Figure 7.5.** <sup>19</sup>F NMR linewidths and relative sideband intensities (normalized to the respective central peak) for the polymer backbone and side chain at a sample spinning speed of 10.5 kHz for [Nafion/(SiO<sub>2</sub>)<sub>x</sub>] with X = 0 and 9 for the temperature range of 25 – 95°C .

**<sup>19</sup>F relaxation.** To get further insights into the chain mobility, <sup>19</sup>F relaxation measurements at sample spinning frequencies of 15 kHz were performed for the

membranes with  $X = 0$  and  $9$  in the dry and wet states. The results for the  $T_1$  and  $T_{1\rho}$  relaxation data are plotted in Figure 7.6 and 7.7.

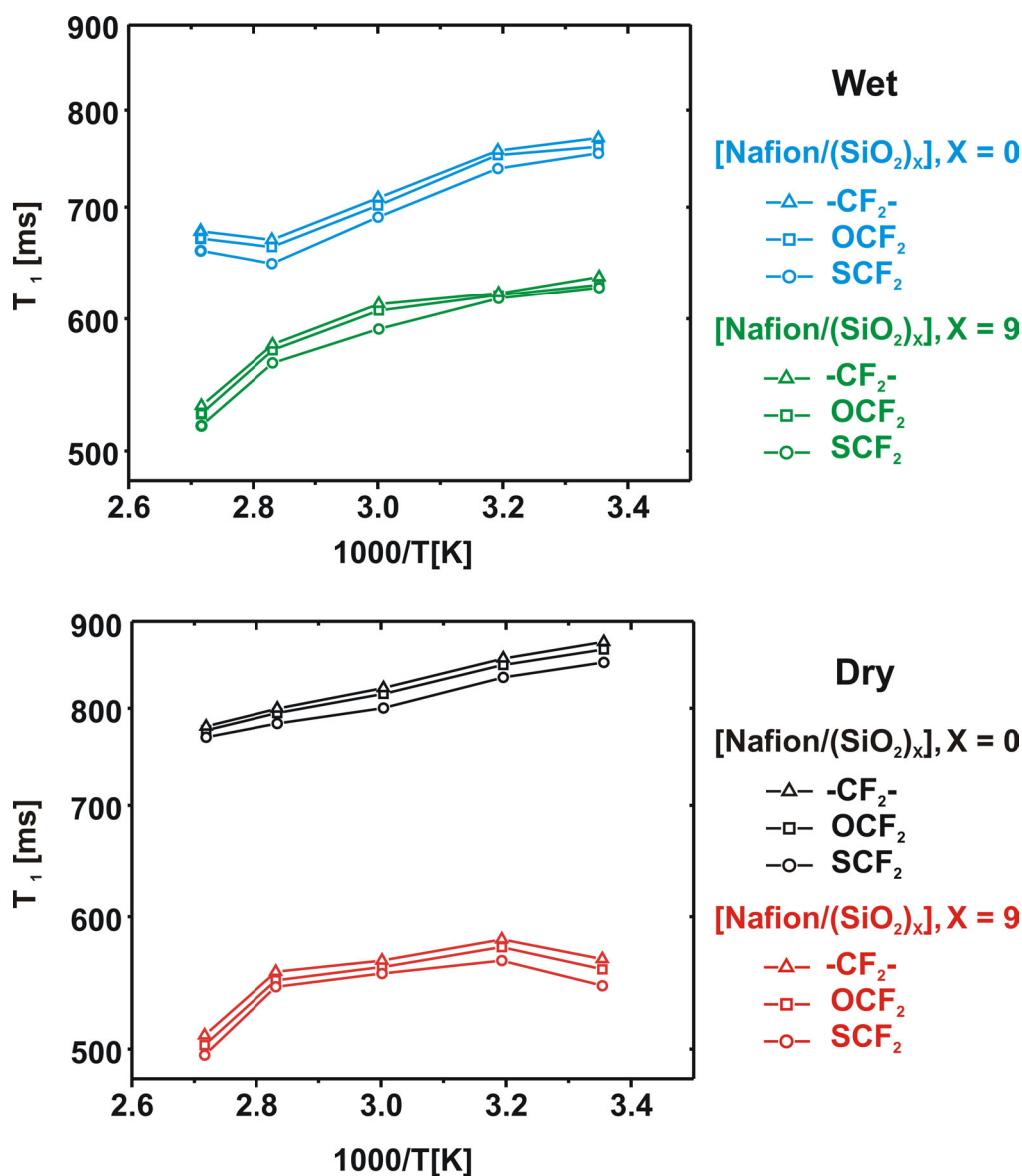


**Figure 7.6.**  $^{19}\text{F}$   $T_1$  values for  $[\text{Nafion}/(\text{SiO}_2)_x]$  with  $X = 0$  and  $9$  in the dry and wet state at a spinning speed of  $15$  kHz.

In general, the  $T_1$  values show a slight decrease with increasing sample temperature. It is noted that the  $T_1$  relaxation data of all segments, i.e. the side chain and the backbone segments, are almost identical. This observation is in line with a former relaxation study on Nafion and is explainable by spin diffusion due to the strongly dipolar coupled  $^{19}\text{F}$  network

[132]. Adding  $\text{SiO}_2$  particles to the membrane causes a shortening of  $T_1$ . By decreasing the water content of the samples a general increase of the  $T_1$  values is registered for the recast Nafion, while for the composite sample the changes are almost negligible.

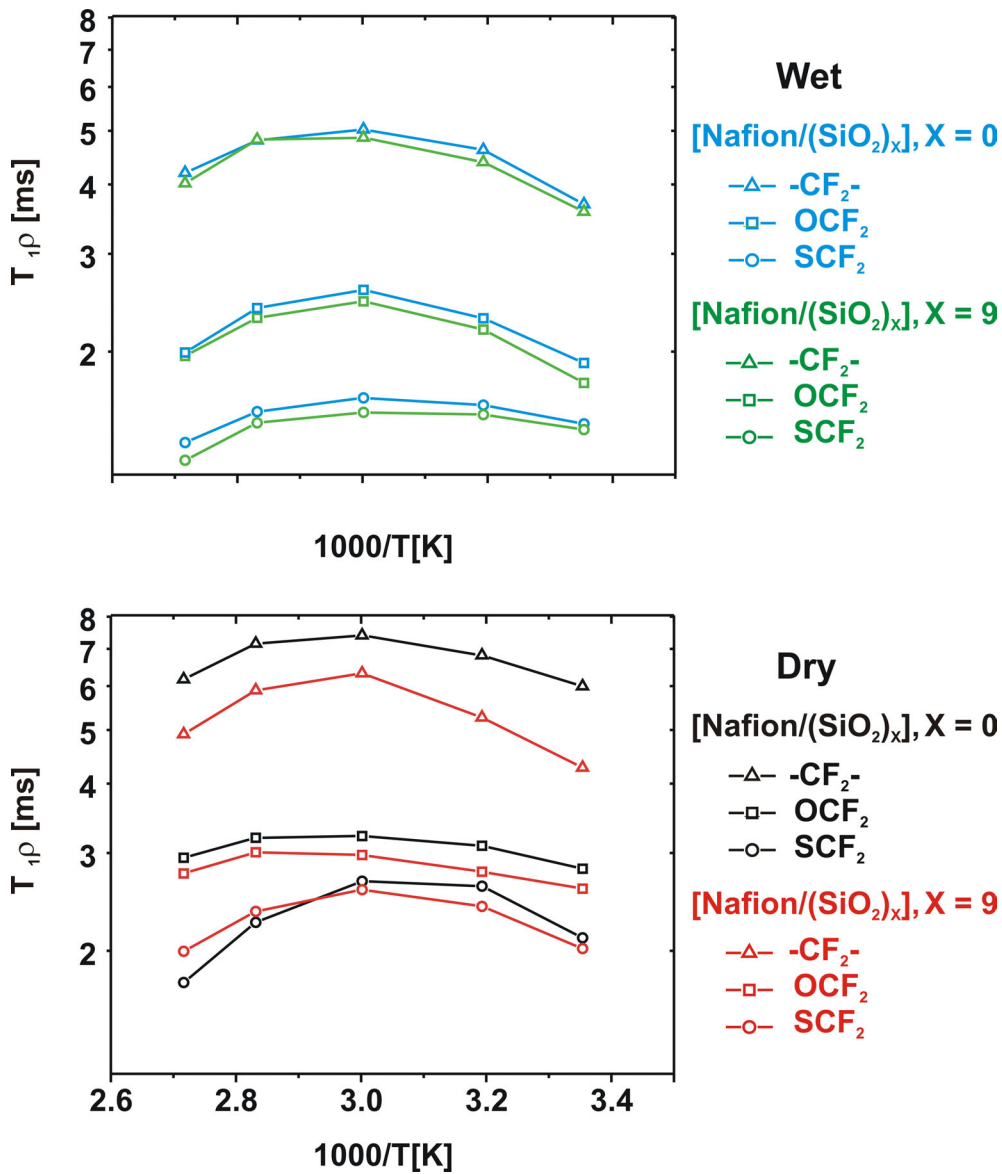


**Figure 7.7.**  $^{19}\text{F}$   $T_{1\rho}$  values for  $[\text{Nafion}/(\text{SiO}_2)_x]$  with  $X = 0$  and  $9$  in the dry and wet state at a spinning speed of  $15$  kHz.

For the  $T_{1\rho}$  data the situation appears to be more complex. As a general trend, a maximum in the relaxation curves is found at around  $60$  °C. Unlike the  $T_1$  data, longer  $T_{1\rho}$  values are observed for the backbone segments than for the side chain units. Within the side chain,

shorter  $T_{1\rho}$  values are found at the end of the side chain. The effect of  $\text{SiO}_2$  particles on the  $T_{1\rho}$  values is the same as found for the  $T_1$  data, i.e., upon addition of particles, the  $T_{1\rho}$  values decrease. The absolute changes, however, strongly depend on both the segment position as well as water content. Hence, by decreasing the water content of the samples, a slight increase in  $T_{1\rho}$  can be observed which is more intense for the recast Nafion as compared to the composite Nafion.

**Equivalent weight and water uptake.** In order to see the effect of drying, i.e. dehydration, on the ion exchange capacity and water uptake, these two parameters are given in Table 7.2 for Nafion and Nafion composite with  $X = 9$ . It is clear that addition of the  $\text{SiO}_2$  particles increase the water content and EW of the membrane. Due to a certain ratio of  $-\text{SO}_3\text{H}$  groups in the Nafion membrane, the respective EW is known to be constant. However, the values for EW are observed to increase for both the recast and the composite membranes after drying. The increase of EW is less for the composite compare to recast Nafion. For the dry state, the water content of both membranes is clearly reduced. However, the water content of the composite membrane remains higher than for the recast Nafion.

**Table 7.2.** Equivalent weight (EW), number of water molecules per sulfonic acid group ( $\lambda$ ) and water volume fraction ( $\varphi$ ) of Nafion recast and [Nafion/ $(\text{SiO}_2)_9$ ] membrane before and after drying process.

	Nafion recast		Nafion recast + 9 w/w% $\text{SiO}_2$	
	Before drying	After drying	Before drying	After drying
EW	1111	1233	1163	1262
$\lambda$	22	12	24.5	13.2
$\varphi$	0.43	0.26	0.44	0.27

**$^{19}\text{F}\{^1\text{H}\}$  CP/MAS NMR.** In order to see the effect of dehydration on the structural changes of Nafion polymer, we also compared the  $^{19}\text{F}\{^1\text{H}\}$  CP/MAS NMR spectra of [Nafion/ $(\text{SiO}_2)_X$ ] with  $X = 0$  and 9 in the dry state (Figure 7.8). In general the spectrum is

similar to the sample  $^{19}\text{F}$  MAS NMR spectrum, but for the  $^{19}\text{F}\{^1\text{H}\}$  CP/MAS NMR spectrum, the intensity of the peaks related to the polymer side chains are enhanced. By transferring the polarization from protons to the fluorine nuclei, the fluorine nuclei which are closer to the proton groups will show an increase in peak intensity. A comparison of the intensities of the side chain peaks in the  $^{19}\text{F}\{^1\text{H}\}$  CP/MAS NMR spectra shows for the  $\text{SCF}_2$  side chain segment of the composite membranes a higher signal intensity, most probably due to more water molecules, in agreement with the results from EW and water uptake.

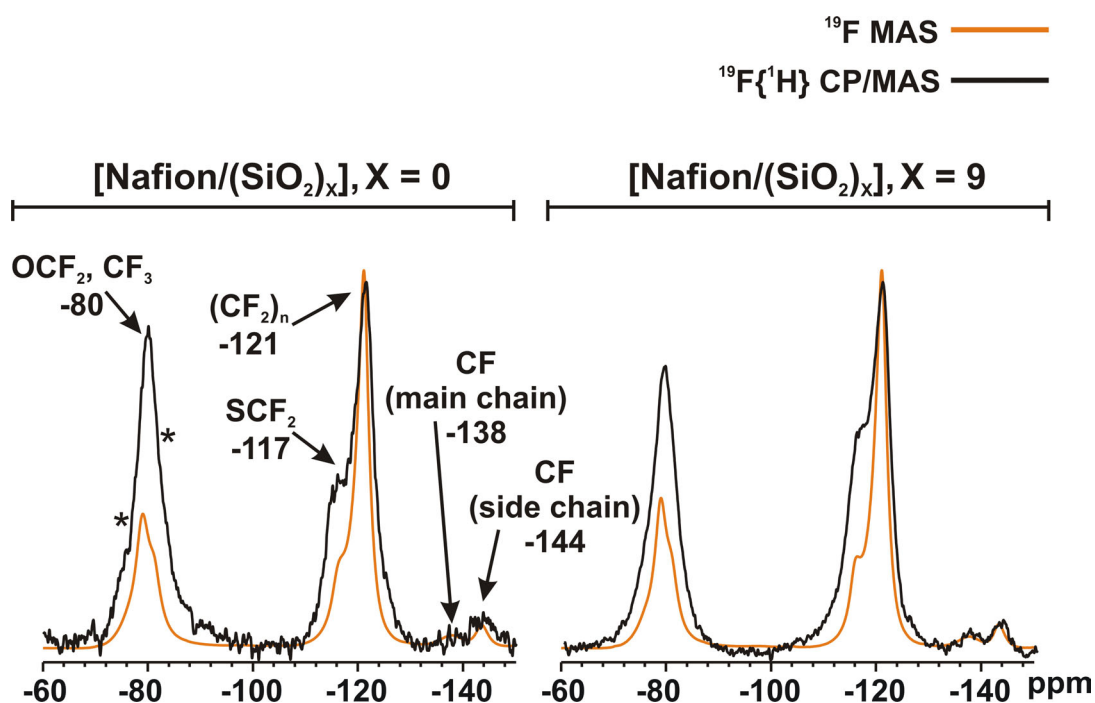


**Figure 7.8.**  $^{19}\text{F}$  NMR and  $^{19}\text{F}\{^1\text{H}\}$  CP/MAS NMR spectra for  $[\text{Nafion}/(\text{SiO}_2)_x]$  with  $X = 0$  and  $9$ , in the dry state at  $T = 25^\circ\text{C}$  at a spinning speed of  $15\text{ kHz}$ .

**$^{19}\text{F}$  MAS NMR after rehydration.** Recently it has been reported that dehydration of Nafion membrane can result in condensation reactions which reduce the ion exchange capacity, water diffusion and proton conductivity of this polymer [179]. In order to be sure that the effect of drying (at  $110^\circ\text{C}$ ) affects only the polymer dynamics and does not cause any changes in the chemical structure of the polymer, a comparison of the  $^{19}\text{F}$  MAS NMR spectra for the samples in the dry and wet state as well as rehydrated state was done. For

this reason,  $^{19}\text{F}$  MAS NMR spectra were recorded for the dry samples after keeping these membranes in water at RT for 1 day (Figure 7.9).

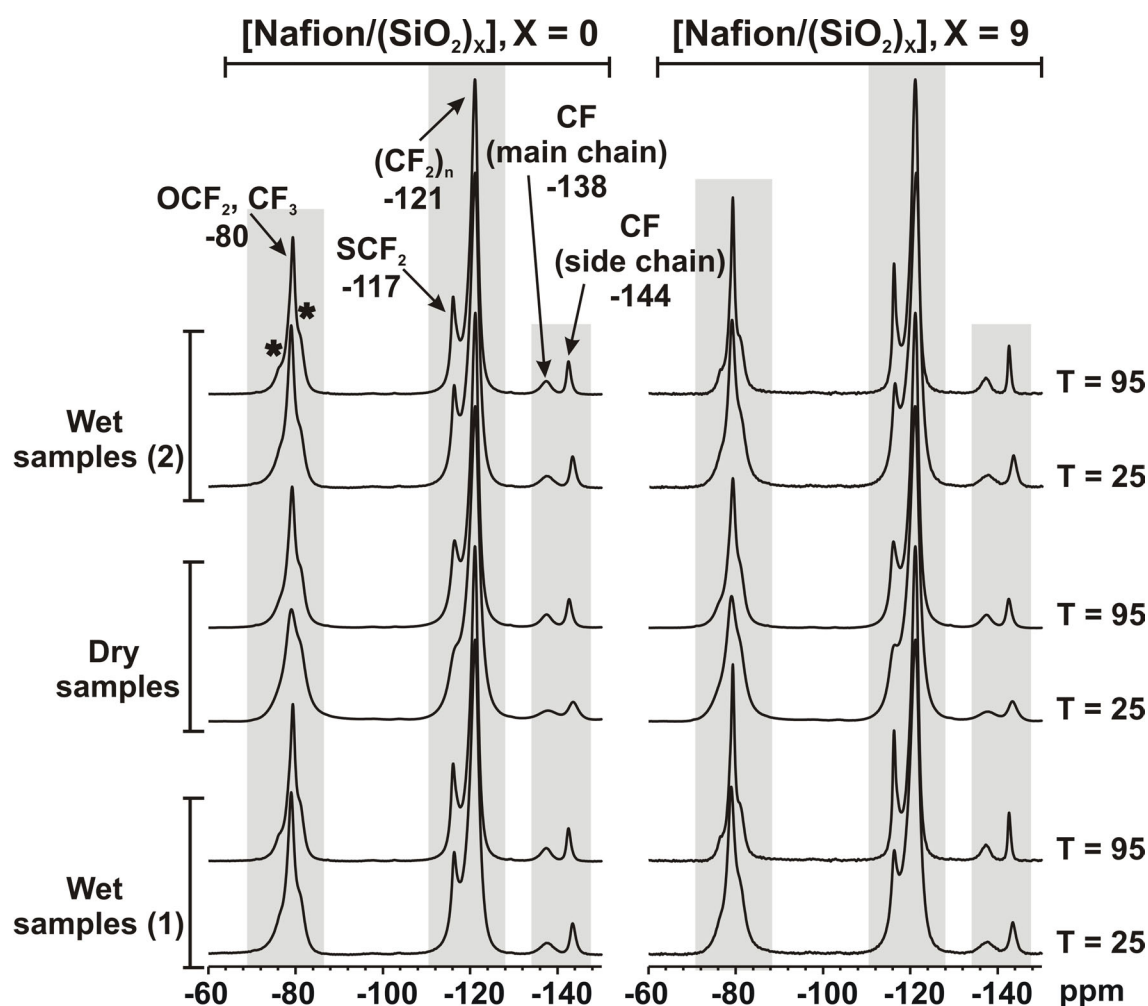


**Figure 7.9.** Solid-state  $^{19}\text{F}$  NMR spectra for  $[\text{Nafion}/(\text{SiO}_2)_x]$  with  $X = 0$  and  $9$  in the wet and dry state as well as in the rehydrated state (wet samples 2). Asterisks indicate spinning sidebands. The given spectra are normalized to the dominant peak of the backbone  $\text{CF}_2$  groups. The sample spinning was  $15\text{ kHz}$ .

Comparison of the spectra for two different wet states, before and after drying, shows no changes in the linewidth as well as the total area of side chain peaks. Comparing any of these wet samples with the dry sample shows that apart from the aforementioned linewidths and spectral resolution differences, the area under the spectra of the wet and dry samples

are identical. The above observations are similar for both pure Nafion and supported Nafion membranes.

## 7.4. Discussion

$^{19}\text{F}$  NMR spectroscopy along with ion exchange capacity and water uptake data were used to examine Nafion membranes with and without  $\text{SiO}_2$  particles. Solid-state NMR showed that membranes with higher conductivity also possess higher mobility. By adding  $\text{SiO}_2$  particles to Nafion, the linewidth and spinning sideband intensity of the  $^{19}\text{F}$  NMR spectra decrease until a value of 9 w/w%  $\text{SiO}_2$  is reached. Similar trends reported by Di Noto et al. for the FT-IR and FT-Raman absorption spectra of  $[\text{Nafion}/(\text{SiO}_2)_x]$  membranes where up to 9 w/w%  $\text{SiO}_2$ , the peak broadening was found to decrease. This phenomenon was explained by an increasing crystallinity, in close analogy to PTFE. It was suggested that the coordination symmetry of  $\text{R-SO}_3\text{H}\dots[\text{SiO}_2]\dots\text{HSO}_3\text{-R}$  will be diminished as the particle concentration will increase over 9 w/w% [88]. An increase of crystallinity for the composite membranes is also reported from the XRD results where the polyfluorocarbon crystalline peaks showed a higher area as compared to the recast Nafion [91]. The effect of using filler particles was further examined by  $^1\text{H}$  MAS NMR of Nafion and Nafion/ $\text{SiO}_2$  samples [147]. It was concluded that higher concentration of particles is a reason for blocking the pathway of proton transport in the Nafion/ $\text{SiO}_2$  composites. Therefore, although by adding  $\text{SiO}_2$  particles to the membrane the water content increases, a higher concentration of filler particles has a negative effect on the mobility as well as on the conductivity.

Former experiments [131,132] and our own experience confirmed that the water content has a strong influence on the NMR parameters that are indicative for the dynamic properties of Nafion. It has been mentioned earlier that because of the effect of water as a plasticizer as well as possible cross-relaxation effects between the  $^{19}\text{F}$  and  $^1\text{H}$  spin system reservoirs, interpretation of  $^{19}\text{F}$  NMR data for the hydrated Nafion with different water content is complicated. Therefore the measurements on both dry and wet samples with defined conditions were done. The experimental data for the  $^{19}\text{F}$  NMR linewidths showed (i) a decrease with increasing temperature, (ii) an increase with decreasing water content

(iii) larger values for the backbone, and (iv) a decrease for the samples with SiO<sub>2</sub> particles ( $X = 9$ ). The linewidths normally can be understood by static disorder in the vicinity of the branching CF segment and also within the Nafion side chain. Moreover, the backbone reorientation is more restricted, and the motional freedom of the side chain segments is higher which explains the differences in linewidths. Since the overall chain motions occur in the fast motional limit, at about 100 kHz or above [176], changes of the motional rates cannot be responsible for the temperature dependent linewidth reductions. Rather, it appears very likely that they reflect (a thermally activated) increase of the fluctuation amplitudes for both the backbone and side chain segments which cause a reduction in static disorder. The stronger temperature dependence of the respective linewidths is explainable by the higher mobility (i.e. larger fluctuation amplitudes) of the side chains.

The same assumptions can be used to explain the experimental findings for the spectral anisotropies (due to chemical shift anisotropy and homonuclear dipolar coupling), which is reflected by the relative intensity of the spinning sidebands. The significant smaller sideband intensities for the side chain segments are thus consistent with their higher fluctuation amplitudes.

The results and trends for the derived  $T_1$  data are in agreement with previous investigations. The observation of identical <sup>19</sup>F  $T_1$  values for all positions in the sample can be understood by the presence of spin diffusion due to the strong homonuclear dipolar interactions between the <sup>19</sup>F nuclei which equalizes the spin-lattice relaxation values for the different chain positions [132]. The decrease of the <sup>19</sup>F  $T_1$  values for the samples with SiO<sub>2</sub> particles is explainable by the additional presence of water which leads to a higher polymer flexibility. After drying the samples, the effect of additional water kept by the SiO<sub>2</sub> particles leaves the respective  $T_1$  values almost unchanged, while for the samples without SiO<sub>2</sub> filler, a stronger decrease in water content causes a remarkable increase in the  $T_1$  values.

Such alterations in the dynamics reflect the changes in the morphology of the polymers after drying, and probably for the closely spaced side chains even condensation reactions might take place. However, as the <sup>19</sup>F NMR spectra of the rehydrated samples demonstrate, these reactions are reversible and therefore no further bond cleavage occurs. SiO<sub>2</sub> particles

keep the side chains separate and avoid condensation reaction between the side chain groups, as reflected by a higher polymer mobility.

The derived  $T_{1\rho}$  data appear much more complex than the  $T_1$  data, as the values (i) change with the chain position (i.e. decrease from backbone to side chain, and towards end of side chain;  $T_{1\rho}(\text{CF}_2) > T_{1\rho}(\text{OCF}_2) > T_{1\rho}(\text{SCF}_2)$ , (ii) decrease for composite membranes, (iii) increase after membrane drying, and (iv) exhibit a maximum at around 60 °C. Obviously, spin diffusion does not affect the  $T_{1\rho}$  data, and the values for the individual segments can be clearly distinguished. Moreover, the trends by the presence of the  $\text{SiO}_2$  particles and after drying are the same as found for the  $T_1$  data. The observation of a maximum in the  $T_{1\rho}$  curves is also in agreement with previous studies [123,132], and was attributed to the appearance of a new motional mechanism which dominates  $T_{1\rho}$  relaxation at higher temperatures. It was also found that the position of the maximum is strongly dependent on the counter ion in the Nafion sample. In agreement with earlier work [123], the additional mechanism is attributed to the  $\alpha$ -process which yields a  $T_{1\rho}$  minimum above 100 °C, and which is responsible for the glass transition.

Accordingly, the aforementioned decrease of the  $T_{1\rho}$  values towards the side chain ends reflects an increase of the motional amplitude in the same direction. The slight decrease of the  $T_{1\rho}$  values for the sample with  $\text{SiO}_2$  particles is again attributed to an increase of the motional amplitude and/or increase of the dipolar interactions due to structural annealing by the higher water content. Upon dehydration, an increase of the  $T_{1\rho}$  values is registered which points to a decrease of the motional amplitude, as discussed earlier.

On the basis of these assumptions it is possible to provide a consistent description of the experimental  $T_{1\rho}$  and  $T_1$  data. Furthermore, it is assumed that the same motional modes are responsible for  $T_{1\rho}$  and  $T_1$  relaxation. The somewhat smaller relaxation values for the sample containing  $\text{SiO}_2$  particles reflect a higher polymer mobility due to the higher water content and even the effects of the absence of condensation reactions of neighboring chains after sample dehydration.

The higher water content and the resulting enhanced polymer mobility also explain the higher conductivity of composite membranes. A comparison of the  $^{19}\text{F}\{^1\text{H}\}$  CP/MAS NMR spectra of Nafion with and without  $\text{SiO}_2$  particles proved the presence of more water in the composite membrane.

Reversible changes by rehydration showed that drying the samples at  $110\text{ }^\circ\text{C}$  did not lead to any irreversible degradation in polymer structure as it is known from the chemical degradation of Nafion caused by radicals [171].

## 7.5. Conclusion

Based on the data from the solid-state NMR investigations and changes of the EW and water uptake, it is concluded that  $\text{SiO}_2$  particles play an important role in stabilizing the chemical structure and morphology of the polymer, especially in the dry state. The presence of particles increases the water uptake of the membranes, with an optimization value of 9 w/w%  $\text{SiO}_2$  at which also the higher conductivity is observed, leading to faster motions of the polymer chains.



## Summary

It is generally believed that fuel cells will play an important role in energy technology already in the near future. Operating polymer electrolyte membrane fuel cells (PEMFCs) at temperatures higher than 100 °C and reduced humidity is anticipated to avoid most of the shortcomings associated with the low-temperature fuel cell operation, such as CO poisoning of the electrode catalysts, slow electrode kinetics of the oxygen reduction reaction and expensive water/thermal management. To date, the operation temperature of PEMFCs is limited to about 90 °C, and this limit is given by the properties of the perfluorosulfonic acid (PFSA) ionomer, Nafion, which is commonly used as a separator material. Apart from the proton conductivity decay at higher temperature and lower humidification, it is also the limited stability of Nafion preventing it from long term operation. Despite the high stability of the PTFE backbone in Nafion, severe deterioration is observed during fuel cell operation. Formation of pinholes and cracks, thinning of the membranes and decrease of ion exchange capacity were reported. The fluorine release indicated that the bond cleavage process takes place under fuel cell operating conditions. Bond cleavage was initially believed to proceed from radical attacks to the carboxyl groups terminating the PTFE backbone of Nafion, and it was claimed to be controlled by the endcapping of the polymer backbone with a CF<sub>3</sub> group. However, the release of fluoride was reported even after endcapping of the materials. The observations proved that bond cleavage limits the stability of PFSA membranes, but the elementary reactions and consequences on the membrane microstructure are not fully understood yet.

In this work, it has been tried to get new insights into the problems of long term stability of polymer electrolytes for low temperature fuel cells. The aim was to identify the changes in the chemical structure of the membrane after operating in a fuel cell. This understanding is essential for extending the operation limit of PFSA-type membranes by either improving the membrane properties or adjusting the conditions within the running fuel cell. In the present work, therefore the changes taking place in PFSA membranes after applying in-situ

and ex-situ aging protocols have been investigated. While the in-situ experiments provide a global picture, the analysis of membranes after ex-situ tests, with various conditions, allows the separation of different types of reactions. In previous studies the degradation changes were mainly monitored by analyzing the released water of the fuel cell or by using the liquid ionomers. In this work with the help of solid-state NMR spectroscopy, the direct study of the chemical structure and dynamics of the polymer membranes before and after the degradation tests became possible.

The structural changes in different parts of the PFSA membranes were first inspected after an in-situ aging test. These examined membranes (Nafion and Hyflon Ion) differed by the length of the side chains. The comparison of the solid-state  $^{13}\text{C}$  and  $^{19}\text{F}$  NMR data of polymers before and after the in-situ degradation test showed that changes can take place not only in the main chain of the polymer, but also within the polymer side chains, as reflected by changes of NMR signals associated with  $\text{CFSO}_3$ ,  $\text{CF}_3$ ,  $\text{OCF}_2$  and  $\text{CF}$  groups. The degree of degradation is found to decrease with increasing membrane thickness while for a given thickness the short side chain polymer, Hyflon Ion, appears to degrade less than Nafion.

In order to understand the reason for these observations, a new ex-situ method has been developed to mimic the degradation of polymer electrolyte membranes in PEM fuel cells (caused by the cross-leakage of  $\text{H}_2$  and  $\text{O}_2$ ). In this ex-situ setup, it was possible to expose membranes to flows of different gases with controlled temperature and humidity.  $\text{H}^+$ -form Nafion films with and without electrode layer (Pt) have been treated in the presence of different gases in order to simulate the anode and cathode side of a PEMFC. The changes of the chemical structure occurring during the degradation tests were primarily examined by solid-state  $^{19}\text{F}$  NMR spectroscopy. For completion, liquid-state NMR studies and ion exchange capacity measurements were performed. It was found that degradation occurs only when both  $\text{H}_2$  and  $\text{O}_2$  are present (condition of gas cross-leakage), and when the membrane is coated with Pt catalyst. The chemical degradation rate is found to be highest for  $\text{H}_2$ -rich mixtures of  $\text{H}_2$  and  $\text{O}_2$ , which corresponds to the conditions at the anode under OCV. It is further shown that side chain disintegration is very important for chemical degradation, although backbone decomposition also might take place. The fact that in-situ

degradation effects were reproduced by the present ex-situ experiments, suggest that membrane degradation in a running fuel cell is mainly the consequence of chemical aging. Detecting the degradation for the membranes coated with Pt in the presence of both gases, H<sub>2</sub> and O<sub>2</sub>, points toward the importance of radicals in the degradation process, which in a running fuel cell (in-situ conditions) may only form in the presence of some gas cross-over, allowing H<sub>2</sub> and O<sub>2</sub> to react at the Pt catalyst of the anode or cathode structure. Since the gas cross-over increases for the thinner Nafion membrane, these results indirectly explain the higher degradation rate of thin Nafion in the in-situ degradation test.

The chemical degradation and stability of PFSA membranes against radical attacks was also investigated in a Fenton ex-situ degradation test. Liquid and solid-state NMR as well as ATR-FTIR spectroscopy were applied to the samples before and after the Fenton reaction. A Comparison of the degradation rate of Nafion and Hyflon Ion in the ex-situ Fenton test again proved that the Hyflon Ion membrane is more stable than Nafion. Comparing the degradation rate of the side chain in these two polymers showed that the stability of Hyflon Ion is mainly due to the shortening of the side chain in this polymer. Hence, the absence of one ether group and the tertiary carbon reduces the degradation rate of the side chain and makes this polymer less sensitive to the radical attacks than Nafion.

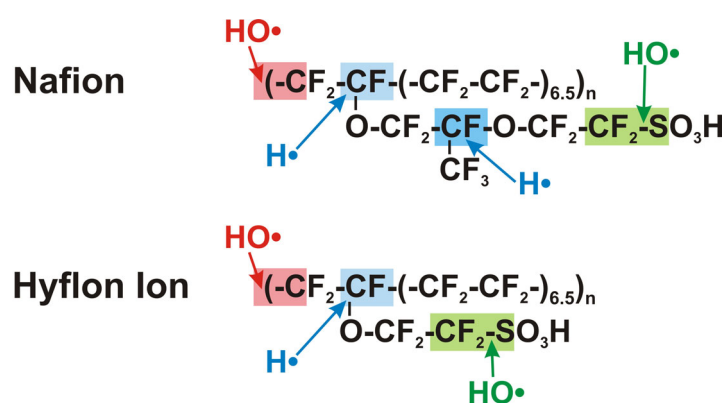


**Figure 1.** Schematic representation of the suggested mechanisms for radical attacks to the main and side chain of Nafion and Hyflon Ion membranes based on the liquid and solid-state NMR results in this work.

For the performance of a membrane not only the chemical structure but also the polymer dynamics is important. Therefore the molecular mobility of the ionomer was investigated

by variable temperature  $^{19}\text{F}$  NMR lineshape,  $T_1$  and  $T_{1\rho}$  relaxation experiments. The decrease of the temperature dependent linewidth was explained by the reduction of static disorder in the Nafion membrane. From the relaxation data there was evidence for structural annealing, which is independent of the chemical degradation. Chemical degradation is considered to reduce the chain flexibility (i.e. the motional amplitudes), which may be explained by chain cross-linking and condensation reaction for the side chains.

To overcome the problem of Nafion's low conductivity at temperatures above 100 °C and low relative humidity, also composite membranes were introduced. These membranes consist of Nafion modified by inorganic oxide additives. It has been reported that under dry conditions, these membranes show enhanced water uptake and water diffusion when compared with filler-free Nafion. In order to understand the reason for the better performance of these polymers, the impact of the oxide particles on the polymer dynamics has been investigated. [Nafion/ $(\text{SiO}_2)_x$ ] composite membranes in the dry and wet state with  $x$  ranging from 0 to 15 w/w% were investigated by variable temperature solid-state  $^{19}\text{F}$  NMR spectroscopy.  $^{19}\text{F}$   $T_1$  and  $T_{1\rho}$  relaxation times and NMR lineshapes were analyzed in order to get details about the polymer mobility.

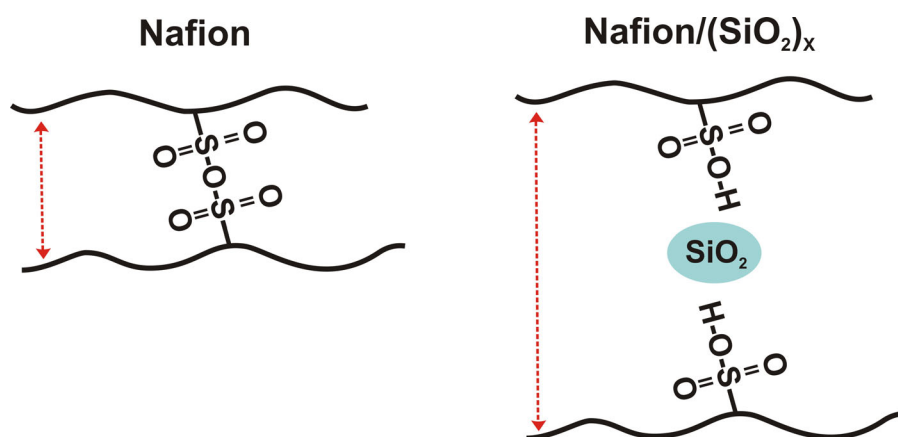


**Figure 2.** Schematic representation of the structure of dried Nafion and Nafion/ $\text{SiO}_2$  polymers. The closer contact of the polymer chains in filler free Nafion increases the chance of condensation reactions.

It is concluded that solid oxide  $\text{SiO}_2$  particles play an important role in stabilizing the chemical structure and morphology of the polymer especially in the dry state. The filler particles lead to higher mobility of polymer chains, if the filler content has an optimized value of about 9 w/w%. The results were further supported by comparing the sideband intensity as well as the linewidth in  $^{19}\text{F}$  NMR and recording the  $^{19}\text{F}\{^1\text{H}\}$  CP/MAS NMR spectra. Furthermore, it has been shown that the structure of composite membranes is more stable after dehydration and possible condensation reactions are less likely in these membranes. The presence of filler particles decrease the chance for morphology changes and close packing of polymer chains in the dry state. Also the decrease of ionic exchange capacity after dehydration is less severe for the composite membrane as compared to filler-free Nafion.

In conclusion, the present results provide a complete picture of solid membrane before and after degradation and of possible mechanisms for radical formation and radical attacks to the polymer. In addition, it is shown which changes can occur in the morphology of polymer chains in low humidification and high temperature. Some general suggestions for the better performance of polymer electrolyte membrane are therefore: For improving the performance of polymer electrode membrane, the sources for the radical formation in the fuel cell should be controlled. This can be possible to some extent by avoiding the use of iron end plates in the fuel cells. Also the chance for the gas crossover through the membrane should be decreased. Thicker membranes show less gas cross-over. By taking into account the higher resistivity of thicker membranes, an optimized membrane thickness should be selected. Hydrocarbon sulfonated polyetherketones possess narrower hydrophilic channels which significantly reduce electroosmotic drag, water permeation as well as gas cross-over. Also the short side chain perfluorinated polymer, Hyflon Ion, with lower electroosmotic drag of water should possess a reduced gas cross-over though the membrane.

The more efficient way for decreasing degradation is to use membranes which are stable against radical attacks. At this point the perfluorinated polymers are still the best available membranes. Endcapping of the backbone in these polymers and decreasing the concentration of reactive end groups like  $\text{COOH}$  during the polymer manufacturing process

can significantly decrease degradation. To minimize degradation of the side chains in perfluorinated polymers, short side chain polymers are suggested because of less reactive groups for the radical attacks and higher concentration of acidic groups. When higher operation temperatures are required, composite Nafion membranes might be used. The higher stability of these membranes makes them advantageous for operating at evaluated temperatures and low relative humidity.

The novel results from the present work lead to a better understanding of membrane degradation, which still represents a serious problem for fuel cells under operation conditions, and provide important indications for future developments of membranes with improved performance for alternative energy conversion devices.

## Deutsche Zusammenfassung

Es ist davon auszugehen, dass Brennstoffzellen in naher Zukunft eine wesentliche Rolle bei der Energiegewinnung spielen werden. Sollte es gelingen, Polymerelektrolytbrennstoffzellen (PEMFCs) bei Temperaturen oberhalb 100 °C und bei reduzierter Feuchtigkeit zu betreiben, dann ließen sich damit die bekannten Nachteile beim laufenden Betrieb – wie CO-Vergiftung des Katalysators, langsame Elektrodenkinetik bei der Sauerstoffreduktion, aufwändiges Wasser- und Temperaturmanagement – größtenteils vermeiden. Bisher liegt die maximale Arbeitstemperatur von PEMFCs bei 90 °C, wobei dies im Wesentlichen durch die Eigenschaften der als Elektrolyt verwendeten Perfluorsulfonsäure-Membran, die unter dem Handelsnamen Nafion bekannt ist, bestimmt ist. Abgesehen von der Abnahme der Protonenleitfähigkeit bei höheren Temperaturen bzw. bei geringer Feuchtigkeit, spielt hier auch die begrenzte Stabilität von Nafion eine wichtige Rolle. Trotz der sehr guten Stabilität des PTFE-Rückgrats von Nafion beobachtet man einen starken Abbau unter realen Brennstoffzellenbedingungen. In diesem Zusammenhang wurde die Ausbildung von Poren und Rissen, eine teilweise Verdünnung der Folie sowie die Abnahme der Ionenaustauschkapazität nachgewiesen. Die beobachtete Fluorid-Freisetzung zeigte, dass während des Brennstoffzellenbetriebs auf molekularer Ebene Bindungen gebrochen werden. Zunächst ging man davon aus, dass dies im Wesentlichen durch Radikalangriff an den Carboxyl-Endgruppen des PTFE-Rückgrats hervorgerufen wird und dass dies durch „Endcapping“, d.h. Schutz mittels CF<sub>3</sub>-Gruppen, verhindert werden kann. Trotzdem wurde auch beim Einsatz entsprechend modifizierter Membranen eine merkliche Fluorid-Freisetzung nachgewiesen. Diese Beobachtungen zeigten, dass die Stabilität dieser Ionomer-Membranen im Wesentlichen durch molekulare Bindungsbrüche begrenzt ist, wobei die Elementarschritte und die damit verbundenen Folgen für die Mikrostruktur der Membranen noch immer nicht vollständig verstanden sind.

Die vorliegende Arbeit befasste sich mit der Langzeitstabilität von Ionomer-Membranen für Niedertemperatur-Brennstoffzellen. Das Ziel war, die Änderungen in der chemischen

Struktur der Membranen im Brennstoffzellenbetrieb zu ermitteln. Diese Informationen sind notwendig, um den begrenzten Arbeitsbereich der bisher eingesetzten Ionomer-Membranen zu vergrößern, sei es durch eine Verbesserung der Membraneigenschaften oder durch Optimierung der Arbeitsbedingungen im realen Brennstoffzellenbetrieb.

In dieser Arbeit wurden die strukturellen Veränderungen in Ionomer-Membranen untersucht, die bestimmten in-situ- und ex-situ-Testprotokollen unterworfen wurden. Die in-situ-Experimente lieferten dabei eher ein globales Bild, während mit Hilfe der ex-situ-Untersuchungen – durch Variation verschiedener Parameter – ein detaillierter Einblick in die verschiedenen Reaktionen, die bei der Membrandegradation eine Rolle spielen, erhalten wurde. In früheren Studien wurde die Membrandegradation meist indirekt durch die Analyse des freigesetzten Wassers und der flüssigen Ionomerkomponenten verfolgt. Demgegenüber wurde in dieser Arbeit die chemische Struktur und molekulare Dynamik der Polymermembranen vor und nach den verschiedenen Degradationstests direkt mittels Festkörper-NMR-Spektroskopie studiert.

Zunächst wurden die strukturellen Änderungen der Ionomermembranen nach definierten in-situ-Tests analysiert. Die in diesem Zusammenhang untersuchten Membranen (Nafion und Hyflon Ion) unterschieden sich in der Länge der Seitenketten. Der Vergleich der ermittelten  $^{13}\text{C}$  und  $^{19}\text{F}$  NMR-Daten für die Polymere vor und nach den in-situ-Degradationstests zeigte, dass strukturelle Änderungen nicht nur in der Hauptkette sondern auch in der Seitenkette stattfinden, was sich über die Änderungen in den Signalintensitäten der  $\text{CFSO}_3^-$ ,  $\text{CF}_3^-$ ,  $\text{OCF}_2^-$  und  $\text{CF}$ -Gruppen nachweisen lässt. Es zeigte sich, dass der Membranabbau mit zunehmender Membrandicke abnimmt. Zudem beobachtete man – bei gegebener Membrandicke – eine geringere Degradation bei der Ionomermembran mit der kürzeren Seitenkette (Hyflon Ion).

Um einen besseren Einblick in die Membrandegradation zu bekommen, wurde ein neuer Ex-situ-Testaufbau entwickelt, der die Degradation von Polymermembranen in Niedertemperaturbrennstoffzellen (beispielsweise bei  $\text{H}_2$  oder  $\text{O}_2$ -Gasdurchtritt) besser nachstellen soll. Mit Hilfe dieses Ex-situ-Testaufbaus war es möglich, die Degradation der Ionomermembranen in Gegenwart von definierten Gasströmen, bei kontrollierter Temperatur und Feuchtigkeit zu untersuchen. Nafion-Membranen mit und ohne Pt-

Elektrodenschicht wurden unterschiedlichen Gasgemischen ausgesetzt, um so die unterschiedlichen Gegebenheiten auf der Kathoden- und Anodenseite der Brennstoffzelle zu simulieren. Die Veränderungen in der chemischen Struktur während dieser Degradationstests wurden hauptsächlich mit Hilfe von  $^{19}\text{F}$  Festkörper-NMR-Spektroskopie studiert. Zusätzlich wurden  $^{19}\text{F}$  Lösungs-NMR- und Ionenaustauschkapazitäts-Messungen vorgenommen. Dabei zeigte sich, dass Degradation nur dann stattfindet, wenn sowohl  $\text{O}_2$  als auch  $\text{H}_2$  im Gasgemisch vorhanden sind (entspricht der Situation beim Gasdurchtritt) und wenn die Membran mit dem Pt-Katalysator beschichtet ist. Den stärksten Abbau findet man bei der Gasmischung mit dem höchsten  $\text{H}_2$ -Gehalt, was den OCV-Bedingungen auf der Anodenseite entspricht. Ebenfalls konnte gezeigt werden, dass der Seitenkettenabbau für die chemische Degradation sehr wichtig ist, obwohl Hauptkettendegradation ebenfalls stattfindet. Aus diesen Untersuchungen konnte geschlossen werden, dass der Membranabbau in einer laufenden Niedertemperaturbrennstoffzelle hauptsächlich auf chemische Degradation zurückzuführen ist. Die Tatsache, dass Degradation nur an Pt-beschichteten Membranen in Gegenwart von  $\text{O}_2$  und  $\text{H}_2$  stattfindet, zeigt die große Bedeutung der Radikale für den Degradationsprozess, die in der laufenden Brennstoffzelle nur bei Gasdurchtritt gebildet werden (Reaktion von  $\text{H}_2$  und  $\text{O}_2$  an der Pt-Oberfläche der Anoden- oder Kathodenseite). Da der Gasdurchtritt bei dünneren Membranen zunimmt, erklärt dies den stärkeren Abbau der dünneren Nafion-Membranen in den entsprechenden In-situ-Tests.

Die chemische Degradation und die Stabilität von Ionomer-Membranen gegen Radikalangriff wurden ferner mittels einem Ex-situ-Fenton-Test studiert. Lösungs-, Festkörper-NMR- sowie FTIR-spektroskopische Messungen wurden an ausgewählten Proben durchgeführt, welche dem Fenton-Test unterworfen wurden. Beim Vergleich zwischen den Nafion- und Hyflon Ion-Membranen zeigte sich wiederum eine bessere Stabilität für das letztgenannte Material, wobei dies im Wesentlichen auf die kürzere Seitenkette zurückgeführt werden kann. Offensichtlich führt hier die Abwesenheit der zusätzlichen Ethergruppe und des tertiären Kohlenstoffatoms zu einer deutlichen Reduktion der Degradationsrate für die Seitenkette und dementsprechend zu einer besseren Stabilität der Polymermembran gegenüber Radikalangriffen.

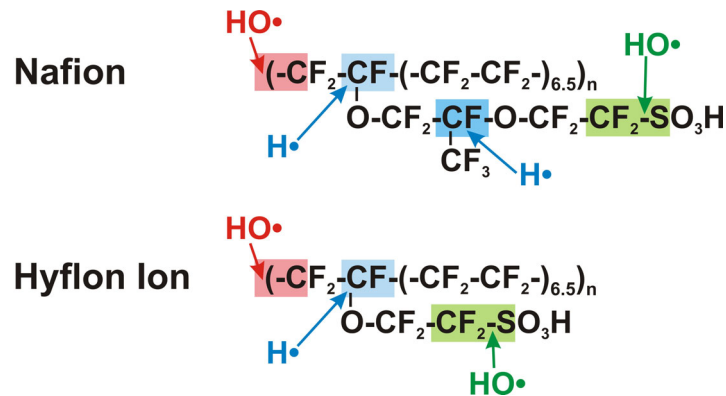


**Abbildung 1.** Schematische Darstellung der vorgeschlagenen Mechanismen, die zum Radikalangriff in der Hauptkette und in der Seitenkette von Nafion- und Hyflon Ion-Membranen führen (basierend auf den NMR-Studien dieser Arbeit).

Für die Membraneigenschaften ist nicht nur die chemische Struktur, sondern auch die Polymerdynamik sehr wichtig. Deshalb wurde die molekulare Beweglichkeit der Ionomer-Membranen mittels temperaturabhängigen  $^{19}\text{F}$  NMR-Linienprofilmessungen sowie  $T_1$ - und  $T_{1\rho}$ -Relaxationsmessungen untersucht. Die Abnahme der temperaturabhängigen Linienbreite wurde mit der Verringerung der statischen Unordnung in der Nafion-Struktur begründet. Die NMR-Relaxationsdaten deuteten die Gegenwart einer strukturellen Temperung der Proben an, unabhängig von der chemischen Degradation. Die eigentliche chemische Degradation führt zu einer Abnahme der Kettenflexibilität, was durch chemische Vernetzung und Kondensationsreaktionen der Seitenketten erklärt werden kann.

In jüngster Zeit wurden sog. Komposit-Membranen eingeführt, um die geringe Protonenleitfähigkeit in Nafion-Membranen bei Temperaturen oberhalb  $100\text{ }^\circ\text{C}$  und bei geringer Feuchtigkeit zu erhöhen. Komposit-Membranen bestehen aus Nafion, denen anorganische Oxide beigemischt werden. Es wurde berichtet, dass diese Membransysteme im Trockenzustand eine höhere Wasseraufnahme und eine verstärkte Wasserdiffusion zeigen als die entsprechenden Polymer-Membranen ohne anorganische Füller. Um die Ursachen dieser verbesserten Eigenschaften der Komposit-Membranen zu verstehen, wurde der Einfluss der anorganischen Komponente auf die Polymerdynamik in  $[\text{Nafion}/(\text{SiO}_2)_x]$ -Kompositen mit einem  $\text{SiO}_2$ -Gehalt im Bereich von  $x = 0$  bis  $15$  Gew. % im trockenen und feuchten Zustand mittels Festkörper-NMR-Spektroskopie untersucht, was

temperaturabhängige  $^{19}\text{F}$  NMR-Linienprofilmessungen,  $T_1$ - und  $T_{1\rho}$ -Relaxationsmessungen einschloss. Es konnte gezeigt werden, dass die  $\text{SiO}_2$ -Partikel eine wichtige Rolle für die Stabilisierung der chemischen Struktur und Morphologie des Polymers, insbesondere im trockenen Zustand, spielen. Die anorganischen Füllpartikel führen zu einer erhöhten Polymerbeweglichkeit, wenn der Füllergehalt einen Wert von ca. 9 Gew.% aufweist. Diese Ergebnisse zur Polymerdynamik begründen sich auf den Relaxationsdaten, Linienbreiten, Seitenbandintensitäten sowie  $^{19}\text{F}\{^1\text{H}\}$  CP/MAS-Spektren. Zudem wurde gezeigt, dass die Struktur der Komposit-Membranen auch nach der Dehydratisierung stabil bleibt, d.h. dass mögliche Kondensationsreaktionen weniger wahrscheinlich sind. Die Gegenwart der anorganischen Füllkomponente reduziert die Möglichkeit von Morphologieänderungen und Packungsänderungen der Polymerketten im trockenen Zustand. Schließlich zeigte sich, dass die Abnahme der Ionenaustauschkapazität nach der Dehydratisierung bei den Komposit-Membranen weniger ausgeprägt ist als für die Membranen ohne anorganischen Füller.

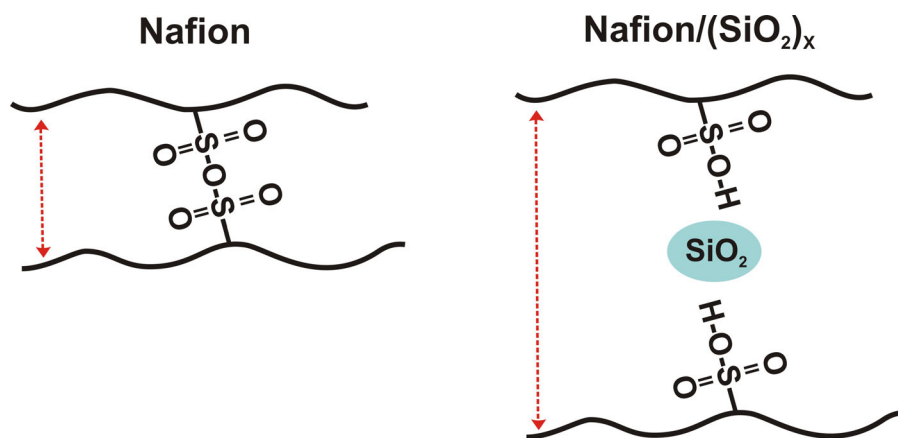


**Abbildung 2.** Schematische Darstellung der Strukturen von trockenen Nafion- und Nafion/ $\text{SiO}_2$ -Membranen. Der geringere Abstand der Polymerketten in der Nafion-Membran vergrößert die Wahrscheinlichkeit von Kondensationsreaktionen.

Zusammenfassend haben die hier vorliegenden Untersuchungen ein vollständiges Bild über die Ionomer-Membranen vor und nach den verschiedenen Degradationstests sowie mögliche Mechanismen zur Radikalbildung bzw. für die Radikalangriffe in diesen Membranen geliefert. Zusätzlich wurde gezeigt, welche Änderungen in der Morphologie

der Polymermembranen bei geringer Feuchtigkeit und hohen Temperaturen auftreten. Auf dieser Basis lassen sich folgende Vorschläge für die Verbesserung der Eigenschaften von Ionomer-Membranen machen: Zur Verbesserung der chemischen Stabilität der Polymerelektroden-Membran sollten die Ursachen der Radikalbildung in Brennstoffzellen kontrolliert werden. In gewissem Ausmaß ist dies möglich, indem man Endplatten aus Eisen in den Brennstoffzellen vermeidet. Ferner sollte ein Gasdurchtritt möglichst minimiert werden. In diesem Zusammenhang zeigen dickere Membranen weniger Gasdurchtritt. Angesichts des größeren Widerstands der dickeren Membranen sollte eine optimale Membrandicke festgelegt werden. Aromatische sulfonierte Polyetherketone zeigen engere hydrophile Kanäle mit reduziertem elektroosmotischen Widerstand, Wasserpermeation und geringerem Gasdurchtritt. Hyflon Ion, mit geringerem elektroosmotischem Widerstand, sollte ebenfalls einen geringeren Gasdurchtritt aufweisen.

Der beste Weg zur Reduzierung der Membrandegradation ist die Verwendung von Ionomer-Membranen, die gegen Radikalangriff stabil sind. Die geeignetsten Materialien sind bisher immer noch die perfluorierten Membransysteme. Ein Schutz der Polymerhauptkette durch „Endcapping“ mittels  $\text{CF}_3$ -Gruppen und eine generelle Verringerung der reaktiven Endgruppen, wie z.B.  $\text{COOH}$ , während des Herstellungsprozesses sollte zu einer deutlichen Verlangsamung der Degradationsrate führen. Eine Verringerung der Degradation der Seitenketten läßt sich durch Verwendung kürzerer Seitenketten (mit geringerer Anzahl potentiell reaktiver Gruppen) erzielen. Wenn höhere Arbeitstemperaturen gefordert sind, können Komposit-Membranen verwendet werden, die eine bessere Stabilität besitzen und auch bei geringer Feuchtigkeit betrieben werden können.

Insgesamt haben die in dieser Arbeit vorgestellten Ergebnisse zu einem besseren Verständnis einer Reihe von Problemen geführt, mit denen man beim Betrieb von Brennstoffzellen konfrontiert in was für die Entwicklung neuer Elektrolytmaterialien für Polymerelektrolytbrennstoffzellen eine wesentliche Voraussetzung darstellt.

## Appendix

### Attenuated Total Reflection Infrared Spectroscopy

Attenuated total reflection infrared (ATR-IR) spectroscopy is a special mode of conventional IR spectroscopy which is used for analysis of the surface of materials. It is also suitable for characterization of materials which are either too thick or absorbing too strong to be analyzed by transmission spectroscopy. The method takes advantage of the difference between refractive indices of the sample being measured and high refractive index crystal such as Si, Ge, or diamond. In ATR-IR spectroscopy the infra red radiation passes through an infrared transmitting crystal with a high refractive index, allowing the radiation to reflect within the crystal several times. To obtain internal reflectance, the angle of incidence must exceed the so called “critical” angle. This angle is a function of the real of the refractive indices of both the sample and the ATR crystal:

$$\theta_c = \sin^{-1} (n_2/n_1) \quad (1)$$

where  $n_2$  is the refractive index of the sample and  $n_1$  is the refractive index of the crystal. This internal reflectance creates an evanescent wave that extends beyond the surface of the crystal into the sample held in contact with the crystal. The evanescent wave decays into the sample exponentially over a distance of the order of microns. The depth of penetration  $d_p$  depends on the angle of the incident beam  $\theta$ , the optical constants of the interface and on the wavelength of radiation  $\lambda$ . It is given by:

$$d_p = \frac{\lambda/n_1}{2\pi\sqrt{\sin^2 \theta - (n_2/n_1)^2}} \quad (2)$$

In regions of the infrared spectrum where the sample absorbs energy, the evanescent wave will be attenuated or altered and less intensity is reflected.

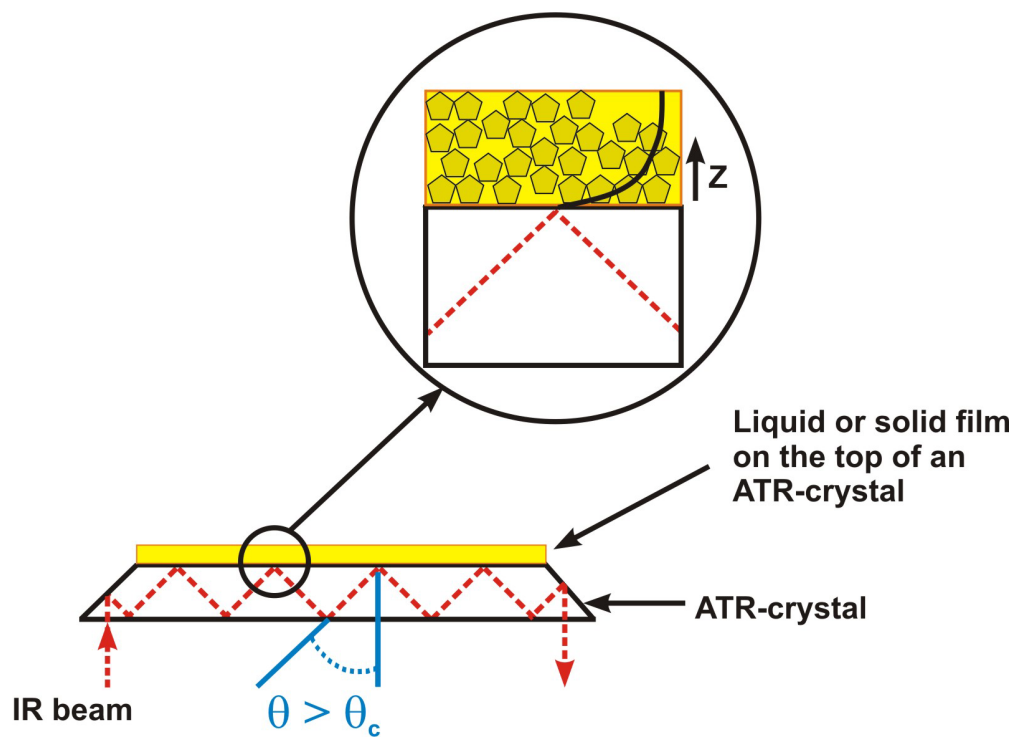


**Figure 1.** Schematic representation of the ATR-IR principle.

## References

- [1] W. Vielstich, A. Lamm, H.A. Gasteiger, Handbook of fuel cells: fundamentals, technology, and applications, Wiley, Chichester, England; Hoboken, N.J., 2003.
- [2] W.R. Grove, Philosophical Magazine and Journal of Science 14 (1839) 127.
- [3] F. Barbir, PEM fuel cells, Elsevier Academic Press, 2005.
- [4] K.A. Mauritz, R.B. Moore, Chemical Reviews 104 (2004) 4535.
- [5] W.C. Heitner, Journal of Membrane Science 120 (1996) 1.
- [6] T.D. Gierke, Bulletin of the American Physical Society 26 (1981) 462.
- [7] T.D. Gierke, G.E. Munn, F.C. Wilson, Journal of Polymer Science Part B-Polymer Physics 19 (1981) 1687.
- [8] H.L. Yeager, A. Steck, Journal of the Electrochemical Society 128 (1981) 1880.
- [9] S.C. Yeo, A. Eisenberg, Journal of Applied Polymer Science 21 (1977) 875.
- [10] M. Fujimura, T. Hashimoto, H. Kawai, Macromolecules 14 (1981) 1309.
- [11] M. Fujimura, T. Hashimoto, H. Kawai, Macromolecules 15 (1982) 136.
- [12] L. Rubatat, G. Gebel, O. Diat, Macromolecules 37 (2004) 7772.
- [13] L. Rubatat, A.L. Rollet, G. Gebel, O. Diat, Macromolecules 35 (2002) 4050.
- [14] H.G. Haubold, T. Vad, H. Jungbluth, P. Hiller, Electrochimica Acta 46 (2001) 1559.
- [15] K. Schmidt-Rohr, Q. Chen, Nature Materials 7 (2008) 75.
- [16] A.V. Anantaraman, C.L. Gardner, Journal of Electroanalytical Chemistry 414 (1996) 115.
- [17] Y. Sone, P. Ekdunge, D. Simonsson, Journal of the Electrochemical Society 143 (1996) 1254.
- [18] T.A. Zawodzinski, C. Derouin, S. Radzinski, R.J. Sherman, V.T. Smith, T.E. Springer, S. Gottesfeld, Journal of the Electrochemical Society 140 (1993) 1041.
- [19] K.D. Kreuer, Chemistry of Materials 8 (1996) 610.
- [20] K.D. Kreuer, Solid State Ionics 136 (2000) 149.
- [21] J.Y. Tilquin, R. Cote, D. Guay, J.P. Dodelet, G. Denes, Journal of Power Sources 193 (1996) 193.
- [22] R.M. Darling, J.P. Meyers, Journal of the Electrochemical Society 152 (2005) A242.
- [23] W. Bi, G.E. Gray, T.F. Fuller, Electrochemical and Solid State Letters 10 (2007) B101.
- [24] R.M. Darling, J.P. Meyers, Journal of the Electrochemical Society 150 (2003) A1523.
- [25] J.P. Meyers, R.M. Darling, Journal of the Electrochemical Society 153 (2006) A1432.
- [26] H. Tang, Z.G. Qi, M. Ramani, J.F. Elter, Journal of Power Sources 158 (2006) 1306.

- [27] Z. Luo, D. Li, H. Tang, M. Pan, R. Ruan, *International Journal of Hydrogen Energy* 31 (2006) 1831.
- [28] D.A. Stevens, M.T. Hicks, G.M. Haugen, J.R. Dahn, *Journal of the Electrochemical Society* 152 (2005) A2309.
- [29] A. Bosnjakovic, S. Schlick, *Journal of Physical Chemistry B* 110 (2006) 10720.
- [30] A. Bosnjakovic, M.K. Kadirov, S. Schlick, *Research on Chemical Intermediates* 33 (2007) 677.
- [31] Z.B. Wang, P.J. Zuo, Y.Y. Chu, Y.Y. Shao, G.P. Yin, *International Journal Of Hydrogen Energy* 34 (2009) 4387.
- [32] B. Smitha, S. Sridhar, A.A. Khan, *Journal of Membrane Science* 259 (2005) 10.
- [33] V. Neburchilov, J. Martin, H.J. Wang, J.J. Zhang, *Journal of Power Sources* 169 (2007) 221.
- [34] K.D. Kreuer, *Journal of Membrane Science* 185 (2001) 29.
- [35] E.N. Balko, J.T. Chaklos, *Journal Of Applied Polymer Science* 26 (1981) 1519.
- [36] A. Pozio, R.F. Silva, M. De Francesco, L. Giorgi, *Electrochimica Acta* 48 (2003) 1543.
- [37] M. Aoki, H. Uchida, M. Watanabe, *Electrochemistry Communications* 7 (2005) 1434.
- [38] V.O. Mittal, H.R. Kunz, J.M. Fenton, *Electrochemical and Solid State Letters* 9 (2006) A299.
- [39] V.O. Mittal, H.R. Kunz, J.M. Fenton, *Journal of the Electrochemical Society* 153 (2006) A1755.
- [40] T. Kinumoto, M. Inaba, Y. Nakayama, K. Ogata, R. Umebayashi, A. Tasaka, Y. Iriyama, T. Abe, Z. Ogumi, *Journal of Power Sources* 158 (2006) 1222.
- [41] W. Liu, K. Ruth, G. Rusch, *Journal of New Materials for Electrochemical Systems* 4 (2001) 227.
- [42] M. Aoki, H. Uchida, M. Watanabe, *Electrochemistry Communications* 8 (2006) 1509.
- [43] V.O. Mittal, H.R. Kunz, J.M. Fenton, *Journal of the Electrochemical Society* 154 (2007) B652.
- [44] H.L. Tang, P.K. Shen, S.P. Jiang, W. Fang, P. Mu, *Journal Of Power Sources* 170 (2007) 85.
- [45] A. Collier, H.J. Wang, X.Z. Yuan, J.J. Zhang, D.P. Wilkinson, *International Journal of Hydrogen Energy* 31 (2006) 1838.
- [46] C.D. Huang, K.S. Tan, H.Y. Lin, K.L. Tan, *Chemical Physics Letters* 371 (2003) 80.
- [47] M.L. Mittleman, J.R. Thomsen, C.A. Wilkie, *Abstracts Of Papers Of The American Chemical Society* 200 (1990) 211.
- [48] J. Surowiec, R. Bogoczek, *Journal Of Thermal Analysis* 33 (1988) 1097.
- [49] M. Danilczuk, F.D. Coms, S. Schlick, *Journal of Physical Chemistry B* 113 (2009) 8031.
- [50] M. Schulze, N. Wagner, T. Kaz, K.A. Friedrich, *Electrochimica Acta* 52 (2007) 2328.
- [51] D.W. Rhoades, M.K. Hassan, S.J. Osborn, R.B. Moore, K.A. Mauritz, *Journal of Power Sources* 172 (2007) 72.
- [52] S.H. Almeida, Y. Kawano, *Polymer Degradation and Stability* 62 (1998) 291.

- [53] A. Panchenko, H. Dilger, J. Kerres, M. Hein, A. Ullrich, T. Kaz, E. Roduner, *Physical Chemistry Chemical Physics* 6 (2004) 2891.
- [54] B. Vogel, E. Aleksandrova, S. Mitov, M. Krafft, A. Dreizler, J. Kerres, M. Hein, E. Roduner, *Journal of the Electrochemical Society* 155 (2008) B570.
- [55] M. Danilczuk, A. Bosnjakovic, M.K. Kadirov, S. Schlick, *Journal of Power Sources* 172 (2007) 78.
- [56] M.K. Kadirov, A. Bosnjakovic, S. Schlick, *Journal of Physical Chemistry B* 109 (2005) 7664.
- [57] A. Panchenko, H. Dilger, E. Moller, T. Sixt, E. Roduner, *Journal of Power Sources* 127 (2004) 325.
- [58] A. Lund, L.D. Macomber, M. Danilczuk, J.E. Stevens, S. Schlick, *Journal of Physical Chemistry B* 111 (2007) 9484.
- [59] E. Endoh, *Electrochemical And Solid State Letters* 7 (2004) A209.
- [60] C. Chen, G. Levitin, D.W. Hess, T.F. Fuller, *Journal of Power Sources* 169 (2007) 288–295.
- [61] F.M. Collette, C. Lorentz, G. Gebel, F. Thominette, *Journal of Membrane Science* 330 (2009) 21.
- [62] J.L. Qiao, M. Saito, K. Hayamizu, T. Okada, *Journal of the Electrochemical Society* 153 (2006) A967.
- [63] T. Xie, C.A. Hayden, *Polymer* 48 (2007) 5497.
- [64] J. Healy, C. Hayden, T. Xie, K. Olson, R. Waldo, A. Brundage, H. Gasteiger, J. Abbott, *Fuel Cells* 5 (2005) 302.
- [65] C. Zhou, M.A. Guerra, Z.M. Qiu, T.A. Zawodzinski, D.A. Schiraldi, *Macromolecules* 40 (2007) 8695.
- [66] M. Schulze, M. Lorenz, N. Wagner, E. Gulzow, *Fresenius Journal Of Analytical Chemistry* 365 (1999) 106.
- [67] M.C. Militello, S.W. Gaarenstroom, *Surface Science Spectra* 10 (2005) 117.
- [68] N.H. Jalani, K. Dunn, R. Datta, *Electrochimica Acta* 51 (2005) 553.
- [69] J. Xie, D.L. Wood, K.L. More, P. Atanassov, R.L. Borup, *Journal Of The Electrochemical Society* 152 (2005) A1011.
- [70] L. Merlo, A. Ghielmi, L. Cirillo, M. Gebert, V. Arcella, *Separation Science and Technology* 42 (2007) 2891.
- [71] L. Merlo, A. Ghielmi, L. Cirillo, M. Gebert, V. Arcella, *Journal of Power Sources* 171 (2007) 140.
- [72] K.D. Kreuer, M. Schuster, B. Obliers, O. Diat, U. Traub, A. Fuchs, U. Klock, S.J. Paddison, J. Maier, *Journal of Power Sources* 178 (2008) 499.
- [73] R.A. Zoppi, S.P. Nunes, *Journal of Electroanalytical Chemistry* 445 (1998) 39.
- [74] R.A. Zoppi, I.V.P. Yoshida, S.P. Nunes, *Polymer* 39 (1998) 1309.
- [75] M. Han, S.H. Chan, S.P. Jiang, in *International Journal of Hydrogen Energy*, 2007, p. 385.
- [76] Y.F. Lin, C.Y. Yen, C.C.M. Ma, S.H. Liao, C.H. Lee, Y.H. Hsiao, H.P. Lin, *Journal of Power Sources* 171 (2007) 388.
- [77] Y. Tominaga, I.C. Hong, S. Asai, M. Sumita, *Journal of Power Sources* 171 (2007) 530.
- [78] H.L. Tang, M. Pan, *Journal of Physical Chemistry C* 112 (2008) 11556.
- [79] Z.G. Shao, H.F. Xu, M.Q. Li, I.M. Hsing, *Solid State Ionics* 177 (2006) 779.

- [80] A.S. Arico, V. Baglio, V. Antonucci, I. Nicotera, C. Oliviero, L. Coppola, P.L. Antonucci, *Journal of Membrane Science* 270 (2006) 221.
- [81] V. Baglio, A.S. Arico, V. Antonucci, I. Nicotera, C. Oliviero, L. Coppola, P.L. Antonucci, *Journal of Power Sources* 163 (2006) 52.
- [82] K.A. Mauritz, R.M. Warren, *Macromolecules* 22 (1989) 1730.
- [83] I.D. Stefanithis, K.A. Mauritz, *Macromolecules* 23 (1990) 2397.
- [84] K.A. Mauritz, I.D. Stefanithis, *Macromolecules* 23 (1990) 1380.
- [85] M. Watanabe, H. Uchida, Y. Seki, M. Emori, P. Stonehart, *Journal of the Electrochemical Society* 143 (1996) 3847.
- [86] M. Watanabe, H. Uchida, M. Emori, *Journal of the Electrochemical Society* 145 (1998) 1137.
- [87] H.T. Wang, B.A. Holmberg, L.M. Huang, Z.B. Wang, A. Mitra, J.M. Norbeck, Y.S. Yan, *Journal of Materials Chemistry* 12 (2002) 834.
- [88] V. Di Noto, R. Gliubizzi, E. Negro, G. Pace, *Journal of Physical Chemistry B* 110 (2006) 24972.
- [89] K.A. Mauritz, I.D. Stefanithis, S.V. Davis, R.W. Scheetz, R.K. Pope, G.L. Wilkes, H.H. Huang, *Journal of Applied Polymer Science* 55 (1995) 181.
- [90] V. Di Noto, M. Piga, L. Piga, S. Polizzi, E. Negro, *Journal of Power Sources* 178 (2008) 561.
- [91] Z.G. Shao, P. Joghee, I.M. Hsing, *Journal of Membrane Science* 229 (2004) 43.
- [92] S. Thayumanasundaram, M. Piga, S. Lavina, E. Negro, M. Jeyapandian, L. Ghassemzadeh, K. Müller, V. Di Noto, *Electrochimica Acta* 55 (2010) 1355.
- [93] K.T. Adjemian, S.J. Lee, S. Srinivasan, J. Benziger, A.B. Bocarsly, *Journal Of The Electrochemical Society* 149 (2002) A256.
- [94] K.T. Adjemian, S. Srinivasan, J. Benziger, A.B. Bocarsly, *Journal Of Power Sources* 109 (2002) 356.
- [95] V. Antonucci, A. Di Blasi, V. Baglio, R. Ornelas, F. Matteucci, J. Ledesma-Garcia, L.G. Arriaga, A.S. Arico, *Electrochimica Acta* 53 (2008) 7350.
- [96] N.H. Jalani, R. Datta, *Journal of Membrane Science* 264 (2005) 167.
- [97] P.L. Antonucci, A.S. Arico, P. Creti, E. Ramunni, V. Antonucci, *Solid State Ionics* 125 (1999) 431.
- [98] N. Miyake, J.S. Wainright, R.F. Savinell, *Journal of the Electrochemical Society* 148 (2001) A905.
- [99] F. Damay, L.C. Klein, *Solid State Ionics* 162 (2003) 261.
- [100] J. Fernandez, J. Bandara, A. Lopez, P. Albers, J. Kiwi, *Chemical Communications* (1998) 1493.
- [101] T. Okada, H. Satou, M. Yuasa, *Langmuir* 19 (2003) 2325.
- [102] J. Xie, D.L. Wood, D.M. Wayne, T.A. Zawodzinski, P. Atanassov, R.L. Borup, *Journal of the Electrochemical Society* 152 (2005) A104.
- [103] C.A. Fyfe, *Solid state NMR for chemists*, C.F.C. Press, Guelph, Ontario, 1983.
- [104] M.J. Duer, *Solid-state NMR spectroscopy: principles and applications*, Blackwell Science, Malden, MA, 2002.
- [105] K.J.D. MacKenzie, M.E. Smith, *Multinuclear solid-state NMR of inorganic materials*, Pergamon, Oxford; New York, 2002.
- [106] K. Schmidt-Rohr, H.W. Spiess, *Multidimensional solid-state NMR and polymers*, Academic Press, London; San Diego, 1994.

- [107] E.O. Stejskal, J.D. Memory, High resolution NMR in the solid state: fundamentals of CP/MAS, Oxford University Press, New York, 1994.
- [108] A. Pines, M.G. Gibby, J.S. Waugh, *Journal of Chemical Physics* 59 (1973) 569.
- [109] I.J. Lowe, *Physical Review Letters* 2 (1959) 285.
- [110] E.R. Andrew, A. Bradbury, R.G. Eades, *Nature* 182 (1958) 1659.
- [111] S.J. Sondheimer, N.J. Bunce, M.E. Lemke, C.A. Fyfe, *Macromolecules* 19 (1986) 339.
- [112] N.J. Bunce, S.J. Sondheimer, C.A. Fyfe, *Macromolecules* 19 (1986) 333.
- [113] G. Xu, Y.S. Pak, *Solid State Ionics* 50 (1992) 339.
- [114] M. Rankothge, Haryadi, G. Moran, J. Hook, L. Vangorkom, *Solid State Ionics* 67 (1994) 241.
- [115] Y.S. Pak, G. Xu, *Journal of the Electrochemical Society* 140 (1993) 1237.
- [116] A.Y. Nosaka, S. Watanabe, I. Toyoda, Y. Nosaka, *Macromolecules* 39 (2006) 4425.
- [117] A.Y. Nosaka, Y. Nosaka, *Journal of Power Sources* 180 (2008) 733.
- [118] J.H. Zhang, M.V. Giotto, W.Y. Wen, A.A. Jones, *Journal of Membrane Science* 269 (2006) 118.
- [119] G. Ye, N. Janzen, G.R. Goward, *Macromolecules* 39 (2006) 3283.
- [120] R.S. Chen, J.P. Jayakody, S.G. Greenbaum, Y.S. Pak, G. Xu, M.G. Mclin, J.J. Fontanella, *Journal of the Electrochemical Society* 140 (1993) 889.
- [121] R.C.T. Slade, A. Hardwick, P.G. Dickens, *Solid State Ionics* 9-10 (1983) 1093.
- [122] N. Sivashinsky, G.B. Tanny, *Journal of Applied Polymer Science* 26 (1981) 2625.
- [123] N.G. Boyle, V.J. McBrierty, A. Eisenberg, *Macromolecules* 16 (1983) 80.
- [124] N.G. Boyle, J.M.D. Coey, V.J. McBrierty, *Chemical Physics Letters* 86 (1982) 16.
- [125] N. Bloembergen, E.M. Purcell, R.V. Pound, *Physical Review* 73 (1948) 679.
- [126] J.J. Fontanella, C.A. Edmondson, M.C. Wintersgill, Y. Wu, S.G. Greenbaum, *Macromolecules* 29 (1996) 4944.
- [127] S. Schlick, G. Gebel, M. Pineri, F. Volino, *Macromolecules* 24 (1991) 3517.
- [128] S.F. Dec, R.A. Wind, G.E. Maciel, *Macromolecules* 20 (1987) 2754.
- [129] Q. Chen, K. Schmidt-Rohr, *Macromolecules* 37 (2004) 5995.
- [130] M. Takasaki, K. Kimura, K. Kawaguchi, A. Abe, G. Katagiri, *Macromolecules* 38 (2005) 6031.
- [131] B. MacMillan, A.R. Sharp, R.L. Armstrong, *Polymer* 40 (1999) 2471.
- [132] K.A. Page, W. Jarrett, R.B. Moore, *Journal of Polymer Science Part B-Polymer Physics* 45 (2007) 2177.
- [133] S. Hietala, S.L. Maunu, F. Sundholm, *Journal of Polymer Science Part B-Polymer Physics* 38 (2000) 3277.
- [134] X. Gong, A. Bandis, A. Tao, G. Meresi, Y. Wang, P.T. Inglefield, A.A. Jones, W.Y. Wen, *Polymer* 42 (2001) 6485.
- [135] V.I. Volkov, S.L. Vasilyak, I.W. Park, H.J. Kim, H. Ju, E.V. Volkov, S.H. Choh, *Applied Magnetic Resonance* 25 (2003) 43.
- [136] H.A. Every, M.A. Hickner, J.E. McGrath, T.A. Zawodzinski, *Journal of Membrane Science* 250 (2005) 183.
- [137] J.C. Perrin, S. Lyonnard, A. Guillermo, P. Levitz, *Magnetic Resonance Imaging* 25 (2007) 501.
- [138] J.C. Perrin, S. Lyonnard, A. Guillermo, P. Levitz, *Fuel Cells* 6 (2006) 5.
- [139] J.C. Perrin, S. Lyonnard, A. Guillermo, P. Levitz, *Journal of Physical Chemistry B* 110 (2006) 5439.

- [140] M. Saito, S. Tsuzuki, K. Hayamizu, T. Okada, *Journal of Physical Chemistry B* 110 (2006) 24410.
- [141] R.C.T. Slade, J. Barker, J.H. Strange, *Solid State Ionics* 35 (1989) 11.
- [142] T.A. Zawodzinski, M. Neeman, L.O. Sillerud, S. Gottesfeld, *Journal of Physical Chemistry* 95 (1991) 6040.
- [143] I. Nicotera, T. Zhang, A. Bocarsly, S. Greenbaum, *Journal of the Electrochemical Society* 154 (2007) B466.
- [144] I. Nicotera, A. Khalfan, G. Goenaga, T. Zhang, A. Bocarsly, S. Greenbaum, *Ionics* 14 (2008) 243.
- [145] M. Ise, K.D. Kreuer, J. Maier, *Solid State Ionics* 125 (1999) 213.
- [146] F. Wang, H. Tang, M. Pan, D. Li, *INTERNATIONAL JOURNAL OF HYDROGEN ENERGY* 33 (2008) 2283.
- [147] G. Ye, C.A. Hayden, G.R. Goward, *Macromolecules* 40 (2007) 1529.
- [148] J. Schaefer, E.O. Stejskal, *Journal of the American Chemical Society* 98 (1976) 1031.
- [149] S.R. Hartmann, E.L. Hahn, *Physical Review* 128 (1962) 2042.
- [150] G. Metz, X.L. Wu, S.O. Smith, *Journal of Magnetic Resonance Series A* 110 (1994) 219.
- [151] D.E. Demco, J. Tegenfeldt, J.S. Waugh, *Physical Review B* 11 (1975) 4133.
- [152] A.K. Khitrin, T. Fujiwara, H. Akutsu, *Journal of Magnetic Resonance* 162 (2003) 46.
- [153] M. Ernst, *Journal of Magnetic Resonance* 162 (2003) 1.
- [154] A.E. Bennett, C.M. Rienstra, M. Auger, K.V. Lakshmi, R.G. Griffin, *Journal of Chemical Physics* 103 (1995) 6951.
- [155] M. Carravetta, M. Eden, X. Zhao, A. Brinkmann, M.H. Levitt, *Chemical Physics Letters* 321 (2000) 205.
- [156] Z.H. Gan, R.R. Ernst, *Solid State Nuclear Magnetic Resonance* 8 (1997) 153.
- [157] A. Detken, E.H. Hardy, M. Ernst, B.H. Meier, *Chemical Physics Letters* 356 (2002) 298.
- [158] S. Ando, R.K. Harris, J. Hirschinger, S.A. Reinsberg, U. Scheler, *Macromolecules* 34 (2001) 66.
- [159] A.J. Vega, A.D. English, *Macromolecules* 13 (1980) 1635.
- [160] G. Meresi, Y. Wang, A. Bandis, P.T. Inglefield, A.A. Jones, W.Y. Wen, *Polymer* 42 (2001) 6153.
- [161] P.K. Isbester, T.A. Kestner, E.J. Munson, *Macromolecules* 30 (1997) 2800.
- [162] S.F. Liu, K. Schmidt-Rohr, *Macromolecules* 34 (2001) 8416.
- [163] T. Gullion, D.B. Baker, M.S. Conradi, *Journal of Magnetic Resonance* 89 (1990) 479.
- [164] G.P. Jones, *Physical review* 148 (1966) 332.
- [165] M. Marrony, R. Barrera, S. Quenet, S. Ginocchio, L. Montelatici, A. Aslanides, *Journal of Power Sources* 182 (2008) 469.
- [166] K.D. Kreuer, S.J. Paddison, E. Spohr, M. Schuster, *Chemical Reviews* 104 (2004) 4637.
- [167] L. Shao, J.J. Titman, *Progress In Nuclear Magnetic Resonance Spectroscopy* 51 (2007) 103.
- [168] A. Bosnjakovic, S. Schlick, *Journal of Physical Chemistry B* 108 (2004) 4332.

- 
- [169] S. Mitov, B. Vogel, E. Roduner, H. Zhang, X. Zhu, V. Gogel, L. Jorissen, M. Hein, D. Xing, F. Schonberger, J. Kerres, *Fuel Cells* 6 (2006) 413.
- [170] A. Panchenko, *Journal of Membrane Science* 278 (2006) 269.
- [171] L. Ghassemzadeh, M. Marrony, R. Barrera, K.D. Kreuer, J. Maier, K. Müller, *Journal of Power Sources* 186 (2009) 334.
- [172] D.E. Curtin, R.D. Lousenberg, T.J. Henry, P.C. Tangeman, M.E. Tisack, *Journal of Power Sources* 131 (2004) 41.
- [173] F.D. Coms, *ECS Transactions* 16 (2008) 235.
- [174] M.I. Bro, C.A. Sperati, *Journal of Polymer Science* 38 (1959) 289.
- [175] K.A. Page, K.M. Cable, R.B. Moore, *Macromolecules* 38 (2005) 6472.
- [176] Q. Chen, K. Schmidt-Rohr, *Macromolecular Chemistry and Physics* 208 (2007) 2189.
- [177] N.G. Boyle, V.J. McBrierty, D.C. Douglass, *Macromolecules* 16 (1983) 75.
- [178] H.J.H. Fenton, *Journal of the Chemical Society* 65 (1894) 899.
- [179] S. Sörgel, in PhD Thesis in Chemistry, Stuttgart University, Max Planck Institute for Solid State Research, Stuttgart, Germany, 2009.



## Acknowledgements

There are many people, to whom I would like to express my sincere words of acknowledgments:

I thank **Prof. Dr. Klaus Müller**, for introducing me to the field of solid-state NMR. He supervised this work in all of its stages, from the very first experiments to the final proof-reading of the manuscript. Not only his scientific expertise, but also his optimism and trust were a great help and motivation throughout my work.

I thank **Prof. Dr. Joachim Maier** for giving me the opportunity to be a member of his group at the Max Planck Institute for Solid-State Research and for providing me an excellent research condition. I thank him for his great contribution in bringing up new questions and ideas.

I am grateful to **Priv. Doz. Dr. Klaus Dieter Kreuer** who suggested a fascinating subject for my PhD research. I thank him for giving me the chance of working independently.

I am grateful to **Prof. Dr. Emil Roduner** for his interest in my work and for accepting to be a member of the examination committee.

I also thank **Prof. Dr. Vito Di Noto** from Padova University in Italy, for the collaborations. I thank him not only for the professional support but also for the good time that he offered me during my stay in Padova. I am also grateful to **Dr. Mathieu Marrony** from European Institute for Energy Research (EIFER) in Karlsruhe and **Dr. Sylvie Escribano** from Nuclear Energy Commission (CEA) in Grenoble for providing the in-situ degradation test samples.

Special thanks to **Udo Klock**, for his technical support in preparing the ex-situ setup and to **Helmut Kammerlander** for fabricating all the glass wares needed for the experiments. I am grateful to **Annette Fuchs**, **Edwald Schmitt** and **Wolfgang König** for their constant

technical support. Also **Uwe Traub** for his friendly help with all computer-related problems and **Sofia Weiglein** for her efficient administrative work.

I thank all of my colleagues in the group of Prof. Müller in Stuttgart University and in the group of Prof. Maier in Max Planck Institute for Solid-State Research for a wonderful atmosphere of work and their indirect help, which became essential in the success of my research.

I am grateful to the **Max Planck Research School** for financial support and to **Dr. Hans-Georg Libuda** for his help during my state in Stuttgart.

Special thanks to **Emerson** for his help and support. He was the one I could always turn to. I've learned from him how to enjoy my research and live with it.

I thank my family for their unconditional love and trust that form the solid basis of my life. Words can not express the feeling that I have for all of them: **Behzad, Behnaz, Mahnaz, Mitra, Bahram** and **Ali**: I love you all! With all my being I want to thank **Mahnaz** and **Behzad** who prepared all the conditions at home to give me the confidence and peace here.

This thesis is dedicated to my parents: my dad, **Ebrahim** and my mom, **Heshmat**.

Daddy, you have been always an example for me. Mom, thank you for your endless support, encouragement, trust and love. Thank you for all the years you calmed my fears. With you I always felt secure. I am sorry for my youthful mistakes, and I finally understand your discipline. Thank you for always being there for me. I love you more than you could imagine.

